SEMMELWEIS EGYETEM

DOKTORI ISKOLA

Ph.D. értekezések

3455.

LÁSZLÓ JÁNOS MARCELL

Klinikai idegtudományok
című program

Programvezető: Dr. Molnár Mária Judit, egyetemi tanár

Témavezetők: Dr. Nardai Sándor, egyetemi docens

Dr. Nagy Zoltán, professor emeritus

NEUROPROTECTIVE AND BLOOD–BRAIN BARRIER–STABILIZING EFFECTS OF N,N-DIMETHYLTRYPTAMINE UNDER ISCHEMIA–REPERFUSION CONDITIONS

PhD thesis

János Marcell László, MD

János Szentágothai Neurosciences Division
Clinical Neuroscience Program
Semmelweis University

Supervisor: Sándor Nardai, MD, PhD
Zoltán Nagy, MD, DSc

Official reviewers: Ákos Menyhárt, PhD
András Makkos, MD, PhD

Head of the Complex Examination Committee:

Dániel Bereczki, MD, DSc

Members of the Complex Examination Committee:

Árpád Dobolyi, DSc
Gabriella Pál, MD, PhD

Budapest
2026

Table of content

LIST OF ABBREVIATIONS 5

1. INTRODUCTION WITH THE SCIENTIFIC BACKGROUND AND THE RELEVANT LITERATURE 8

Stroke epidemiology and treatment 8
Mechanisms of stroke from the perspective of the neurovascular unit 8
Microglia function and morphology: activation, proliferation, phagocytosis 12
Peripheral immune response: cytokines and chemokines 13
Mechanisms of stroke-associated brain edema 15
N,N-Dimethyltryptamine (DMT) and the sigma-1 receptor 16

2. OBJECTIVES 19

3. METHODS 20

In vivo 20
Animal model and treatment protocol 20
Lesion volume and edema measurement 22
MRI measurement of lesion volume 23
Quantitative MRI image analysis 23
Functional testing using the “staircase method” 24
Blood-brain barrier permeability *in vivo* 25
Brain section immunohistochemistry 1: S1R, MAP-2, IBA-1 26
Brain section immunohistochemistry 2: CLDN5, GFAP, AQP4, IBA1 26
Confocal microscopy 28
Brain section immunohistochemistry image analysis 28
Analysis of microglia morphology 29
Brain Tissue Sampling for mRNA Expression Analysis 29
RNA isolation, cDNA synthesis and qPCR from brain samples 30
RNA isolation, cDNA synthesis and qPCR from PBMC pellets 30
Serum CLDN5, matrix metalloproteinase-9 (MMP9) and GFAP ELISA 31
Preliminary assessment of circulating biomarkers 31
Comprehensive assessment of circulating biomarkers 31

In vitro ... 32
Cell Cultures ... 32
Oxygen-glucose deprivation and reoxygenation model ... 32
Impedance-based measurement of endothelial cells, pericytes and glial cells ... 33
Barrier integrity tests ... 33

4. RESULTS ... 38

DMT reduces lesion volume and BBB disruption in a rat stroke model ... 38
DMT attenuates oxygen-glucose deprivation–induced barrier disruption in a rat co-culture model ... 43
DMT preserves BBB integrity via claudin-5 stabilization and mitigates cytotoxic edema by downregulating AQP4 activation ... 49
DMT modulates gene expression and attenuates cytokine release in brain endothelial cells following OGDR ... 54
DMT modulates cerebral expression of inflammation-related cytokine genes following focal ischemia ... 57
Initial assessment of circulating biomarkers ... 59
Comprehensive assessment of DMT-induced increases in circulating biomarkers including BD1063 treated and sham operated groups ... 60
DMT attenuates microglial activation following stroke ... 63
S1R is expressed in neurons and microglia in the peri-infarct cortex ... 67
Decreased apoptosis following DMT treatment ... 68
Preliminary analysis of neurotrophic factor levels in the cortex and serum, without sigma-1 receptor antagonist treatment or sham-operated controls ... 69
Assessment of serum neurotrophic factor levels, including sigma-1 receptor antagonist–treated and sham-operated control groups ... 70
Improved motor function following DMT treatment ... 71

5. DISCUSSION ... 72

BBB integrity ... 74
Inflammation ... 75
Apoptosis ... 76
Neuroplasticity ... 77

Key limitations 78
Translational feasibility 78
6. CONCLUSION 80
7. SUMMARY 81
Összefoglalás 82
8. REFERENCES 83
9. BIBLIOGRAPHY OF THE CANDIDATE'S PUBLICATIONS 101
10. ACKNOWLEDGMENTS 102

List of Abbreviations

3D – Three-dimensional

5-HT2A – 5-hydroxytryptamine 2a receptor

AJ – Adherent junctions

ANOVA – Analysis of variance

APAF1 – Apoptotic protease activating factor 1

AQP4 – Aquaporin-4

ARRIVE Guidelines – Animal research: reporting of in vivo experiments

ATP – Adenosine triphosphate

BBB – Blood-brain barrier

BD1063 – 1-[2-(3,4-dichlorophenyl)ethyl]-4-methylpiperazine

BDNF – Brain-derived neurotrophic factor

bp – Base pair

BSA – Bovine serum albumin

cDNA – Complementary deoxyribonucleic acid

CINC-1 – Cytokine-induced neutrophil chemoattractant 1

CLDN5 – Claudin-5

CNS – Central nervous system

CSF – Cerebrospinal fluid

CXCL1 – Chemokine (c-x-c motif) ligand 1

CXCL-8 – C-x-c motif chemokine ligand 8

CXCL-10 – C-x-c motif chemokine ligand 10

DAMPs – Danger-associated molecular patterns

DAPI – 4′,6-diamidino-2-phenylindole

DMT – N,n-dimethyltryptamine

DMEM – Dulbecco's modified eagle medium

DMSO – Dimethyl sulfoxide

DW – Distilled water

EBA – Evans blue-labelled albumin

EDTA – Ethylenediaminetetraacetic acid

ELISA – Enzyme-linked immunosorbent assay

FBS – Fetal bovine serum

FDR – False discovery rate

FITC – Fluorescein isothiocyanate

FSE – Fast spin echo

GFAP – Glial fibrillary acidic protein

GO – Gene ontology

IBA1 – Ionized calcium-binding adapter molecule 1

ICAM-1 – Intercellular adhesion molecule-1

IL-1β – Interleukin-1 beta

IL-6 – Interleukin-6

IL-10 – Interleukin-10

IMPROVE Guidelines – Ischaemia models: procedural refinements of in vivo experiments

i.p. – Intraperitoneally

log2FC – Log2 fold change

MAP – Microtubule-associated protein 2

MAO-A – Monoamine oxidase a

MACE-seq – Massive analysis of cdna ends sequencing

MCAO – Middle cerebral artery occlusion

MMP – Matrix metalloproteinase

MMP9 – Matrix metallopeptidase 9

MRI – Magnetic resonance imaging

MTT – 3-(4,5-dimethylthiazol-2-yl)-2,5-diphenyltetrazolium bromide

MW – Molecular weight

mRNA – Messenger ribonucleic acid

NA – Numerical aperture

NHS – Normal horse serum

NK cells – Natural killer cells

NVU – Neurovascular unit

OGD – Oxygen-glucose deprivation

OGDR – Oxygen-glucose deprivation followed by reoxygenation

ON – Overnight

PBS – Phosphate buffered saline

PBMC – Peripheral blood mononuclear cell

PFA – Paraformaldehyde

Pe – Permeability coefficient

PPIA – Peptidylprolyl isomerase a

PCR – Polymerase chain reaction

qPCR – Quantitative polymerase chain reaction

RAGE – Receptor for advanced glycation end products

RIN – Rna integrity number

RNA – Ribonucleic acid

RNA-seq – Rna sequencing

ROS – Reactive oxygen species

RPM – Rotations per minute

RT – Room temperature

S1R – Sigma-1 receptor

SD – Standard deviation

SEM – Standard error of the mean

SF – Sodium fluorescein

SII – Systemic immune-inflammation index

TEER – Transendothelial electrical resistance

TJ – Tight junction

TLRs – Toll-like receptors

TNF-α – Tumor necrosis factor alpha

tMCAO – Transient middle cerebral artery occlusion

Treg cells – Regulatory t cells

TTC – 2,3,5-triphenyltetrazolium chloride

TX-PBS – Triton-x phosphate buffered saline

UV – Ultraviolet

VCAM-1 – Vascular cell adhesion molecule-1

ZO-1 – Zonula occludens-1

ZO-2 – Zonula occludens-2

ZO-3 – Zonula occludens-3

1. Introduction with the scientific background and the relevant literature

Stroke epidemiology and treatment

Stroke remains one of the most serious neurological conditions, often resulting in long-term disability and placing a considerable burden on patients, their families, and the healthcare system (1). The associated direct and indirect costs are substantial. Although numerous neuroprotective strategies have been explored over the past decades, none have yet become part of standard clinical care (2). The underlying pathophysiological processes involve a complex interplay of multiple cell types, signaling cascades, and regulatory loops. The resulting damage frequently leads to lasting structural and functional deficits. Therapeutic approaches targeting only a single component or cell population have generally not been sufficient to significantly improve outcomes (3). Currently available stroke treatments, such as intravenous thrombolysis and endovascular thrombectomy, are limited by narrow therapeutic time windows and are not applicable to all patients. Moreover, these interventions carry the risk of serious complications. Given these limitations, therapeutic options for preventing neuronal death and for managing post-stroke brain edema remain inadequate (1-3).

Mechanisms of stroke from the perspective of the neurovascular unit

Following ischemia, a wide range of spatially and temporally well-characterized events unfolds, resulting in blood-brain barrier (BBB) disruption. The prompt activation of microglia, astrocyte, pericyte and endothelial cells lead to the production of various proinflammatory cytokines and chemokines initiating neuroinflammation (4, 5). This leads to swift BBB opening with consequential extravasation of blood-borne molecules into the brain parenchyma, inducing further reactions that aggravate BBB disruption (6, 7). The wave of infiltrating peripheral leukocytes such as neutrophils, monocytes and lymphocytes disrupt the BBB further, creating the inflammatory milieu of cytokines and chemokines which drive neuroinflammation, ultimately causing secondary neuron damage and lesion expansion (4, 8, 9).

The neurovascular unit (NVU) is a structural and functional unit of the BBB comprising **neurons** and **endothelial cells** that interact with surrounding **astrocytes**, **pericytes**, and the **basement membrane** to maintain BBB stability (10, 11).

Astrocyte end-feet cover more than 99% of the BBB endothelium (12) underscoring the essential role astrocytes play in maintaining BBB integrity (13). Cytotoxic swelling of astrocytic end-feet begins within minutes of energy depletion following cerebral infarction, leading to their detachment from the endothelium and subsequent disruption of the BBB (14). Aquaporin-4 (AQP4) is largely expressed in astrocytic end-feet, adjacent to cerebral capillaries (15). Extensive evidence from studies on transgenic mice deficient in AQP4 has highlighted the role of this water channel in both cytotoxic and vasogenic edema. During the formation of ischemic cerebral edema, AQP4 expression increases in astrocyte end-feet, facilitating passive water movement through the astrocytic plasma membrane driven by osmotic gradients, which leads to astrocyte cytotoxic swelling (16, 17). Several earlier studies showed that the absence of AQP-4 correlates with smaller infarct size, reduced astrocyte swelling, decreased brain edema, and even improved long term outcome (16, 18, 19). As a background mechanism modified astrocyte activation, reduced microglia activation and reduced neuroinflammation was verified (16). Astrocyte swelling causes intracellular calcium signaling events, promoting signaling cascades that release neuroactive substances such as glutamate and adenosine triphosphate (ATP), which initiate and exacerbate excitotoxicity and neuroinflammtion (20). In acute stroke patients, there is a strong positive correlation between serum glial fibrillary acidic protein (GFAP) levels derived from astrocytes and various clinical parameters, such as infarct size (21-23), severity of neurology deficits in the acute phase (23) as well as long-term outcomes at 3 months (22) and 1 year (24). Serum GFAP measurement in the early phase of the stroke appears to be a reliable biomarker for detecting intracerebral hemorrhage (25-27).

Pericytes are unevenly distributed along the walls of brain microvessels, covering at least 80% of the microvascular surface. They provide structural support to the endothelium within the NVU and play a crucial role in the formation and maintenance of the blood-brain barrier (28). Pericytes possess contractile abilities that allow them to regulate capillary blood flow and influence autoregulation of cerebral blood flow (29, 30). During ischemic stroke, pericytes respond rapidly by migrating from the microvessel wall, undergoing constriction, and detaching from the basement membrane (31). This process disrupts interactions between pericytes and tight junctions, leading to increased permeability of the BBB (32, 33).

Endothelial cells are characterized by a the absence of fenestrae and the high expression of proteins that form unique physical barrier between adjacent cells (34). The components of this firm connections are: tight junctions (TJ) composed of occludin, claudin, zonula occludens: ZO-1, ZO-2, ZO-3 and cingulin; adherent junctions (AJ) composed of cadherins, catenins, vinculin and actinin; and junctional adhesion molecules (35). All three structural components are anchored to the actin cytoskeleton. The tightness of the tight junction connections determines the paracellular permeability of water-soluble molecules (13). From the onset of cerebral ischemia, endothelial cells respond with cytoskeletal reorganization and the translocation of tight junctions, which widens the paracellular space between the cells, leading to hyperpermeability (36). Central nervous system (CNS) endothelial cells have lower rates of transcytosis compared to peripheral endothelial cells, which prevents blood components from crossing the blood-brain barrier through non-specific vesicular transport (28).

Claudin-5 (CLDN5) is the most abundant tight junction protein in endothelial cells and is especially highly expressed in the endothelial cells of the central nervous system (37). In cultured brain-derived endothelial cells, exposure to hypoxia led to facilitated disappearance of claudin-5 from the plasma membrane and reduced its total cellular protein levels, while mRNA levels remained unchanged. This coincided with a decrease in trans-endothelial electrical resistance. These findings suggest that hypoxia-induced alterations in claudin-5 expression may be due to posttranscriptional mechanisms, possibly involving increased degradation or decreased translation efficiency (38). The leakage of the blood-brain barrier in response to ischemia appears to begin with an upregulation of endothelial transcytosis, characterized by an increased number of visible vesicles within endothelial cells as early as 4–6 hours post-injury. Subsequently, there is significant remodeling of tight junction complexes during the later phase, typically starting after 24 hours (39, 40). One possible mechanism of the dissociation of claudin-5 from the cytoskeleton is caveolin-1 mediated endocytosis (39, 41). The experimentally induced mosaic loss of CLDN5 in adult mice brain endothelial cells resulted in increased blood-brain barrier leakage and the rapid onset of neuroinflammation. This was marked by widespread activation of endothelial cells, microglia, and astrocytes, which further contributed to BBB opening. These findings underscore the critical role of CLDN5 in maintaining the integrity of the adult BBB and

highlight the pathological consequences associated with its dysregulation (42). Patients who developed clinical deterioration as a result of hemorrhagic transformation following stroke had higher serum claudin-5 levels within 3 hours of stroke onset compared to those who did not experience such complications. This indicates that measuring serum CLDN5 levels shortly after stroke onset could serve as an effective screening method for identifying patients at high risk of hemorrhagic transformation in acute ischemic stroke (43).

Endothelial cells upon activation start to express adhesion molecules (ICAM-1, VCAM-1, selectin, integrin), enabling **peripheral leukocytes** to infiltrate the infarcted area (44, 45). This recruitment of peripheral leukocyte gives a further push to the BBB disruption peaking between 1-3 days (46). Many reports have shown that following stroke, neutrophils are the first blood-derived leukocytes to infiltrate the ischemic brain within a few hours. Their numbers peak between days 1–3 and then decline over time (47-50). Somewhat later, between 2-6 hours after the insult, peripheral monocytes begin to infiltrate. Their numbers peak at day 7 and decrease thereafter (51-53). T cells also accumulate in the ischemic brain within the initial 24 hours following cerebral ischemia (54, 55). Upon extravasation, activated leukocytes release proteases, MMPs, and ROS, directly damaging blood vessels. Additionally, they produce biologically active substances such as eicosanoids, leukotrienes, prostaglandins, and platelet-activating factor, which induce vasoconstriction and promote platelet aggregation. Leukocytes adhere to the endothelium, causing microvascular blood flow obstruction, thereby contributing to the cerebral no-reflow phenomenon (56). Finally, infiltrated leukocytes exacerbate neuronal injury by activating proinflammatory factors within the penumbra and infarct core areas (57).

Activated microglia and infiltrating neutrophils are the primary sources of MMP-9, which has the capability to degrade the **basal lamina** (58). The basal lamina is divided into two layers: the vascular basement membrane produced by pericytes and endothelial cells and the glial basement membrane secreted by astrocytes (59). It separates and anchors cells through adhesion receptors (60). MMPs exhibit substrate specificity for type IV collagen, laminin, and fibronectin, which are structural components of the basement membrane. **MMP-9**, in particular, plays a critical role in disrupting the blood-brain barrier during ischemic stroke, thereby affecting the integrity of connections within the

neurovascular unit (61, 62). Serum levels of MMP-9 in the acute phase of stroke patients were significantly correlated with infarct volume (63), early lesion progression (64), hemorrhagic transformation (65, 66), early neurological deficits, long-term major disability, and increased risk of death at 3 months (67, 68).

Microglia function and morphology: activation, proliferation, phagocytosis

The interruption of the physiological ligand-receptor-mediated crosstalk between microglia, neurons, and astrocytes (6) together with neuron-released glutamate due to ischemia alerts microglia (69). Moreover, the leakage of blood components across the altered BBB after stroke also serves as an activating signal to microglia, thereby inducing an inflammatory response (70, 71). Activated microglia, similar to macrophages, have the ability to phagocytose, produce cytokines and MMPs that exacerbates BBB disruption (72). It is estimated that microglia start to produce pro-inflammatory cytokines like TNF-α and IL- 1β within hours after stroke onset (73). Activated microglia are prone to phagocytosing viable neurons when these neurons temporarily express an 'eat me' signal (74) or when the damaged BBB leads to complement deposition on neurons, prompting direct phagocytosis (75). Activated capillary-associated microglia can markedly contribute to the expansion of infarct lesions in the peri-infarct region following brain ischemia, based on the observation that this particular subset of microglia is capable of phagocytosing viable endothelial cells, leading to local endothelial activation and promoting vessel disintegration (71). The proliferation of microglia following ischemia reperfusion has been well-established for many years. The dominant immune cells in the first 24h of stroke are overwhelming microglia that present intensive proliferating activity (76). Increasing numbers of macrophages infiltrating from the periphery accumulate in the infarcted necrotic core from day 3 post-stroke taking the task of clearing the necrotic core tissue instead of microglia. Infiltrating macrophages possibly weaken microglial phagocytosis while in reverse microglia boost macrophage phagocytosis (77). At this stage, microglia gather at the outskirts of the infarcted core in the peri-infarct regions (78).

It is important to note that inhibiting microglial activation has been associated with reduced infarct volume and alleviation of neuroinflammation (79). However, complete depletion of microglia has been shown to increase the size of the ischemic lesion

(80). One possible mechanism underlying this observation is that microglial phagocytic function mitigates the damaging effects of infiltrating neutrophils during brain ischemia (81). Microglia are not essential for recruiting peripheral leukocytes but play a crucial role in mitigating the harmful effects of these infiltrating leukocytes during neuroinflammation, thereby preventing the expansion of secondary lesions. Additionally, the presence of microglia has been demonstrated to attenuate the astrocytic response induced by ischemia, thereby inhibiting the secretion of inflammatory factors by astrocytes (82). Furthermore, the fact that completely blocking the entry of monocytes into the infarcted area worsens the outcome of cerebral ischemia underscores the complexity of the interplay between peripheral and CNS-resident immune cells. (83, 84).

Ramified microglia are the most common microglial phenotype in the mature CNS. Previously they were labeled as "resting", but in reality, these cells are incredibly dynamic, constantly monitoring their immediate environment with thin, branched and highly motile processes making transient contacts with neurons, basal lamina and astrocytes (85). Furthermore, even in their steady state, ramified microglia appear to be protective against excitotoxic neuronal cell death. (86). They seem undoubtedly "resting" compared to the impressive and rapid morphological shift they can undergo in response to stimuli. Microglia take an amoeboid morphology in response to acute ischemia. Amoeboid microglia are much more macrophage-like, identified by round and larger cell bodies and lack of processes, indicating overall increased mobility (87). Experimental models have demonstrated that morphology shift from ramified to amoeboid form occurs within 30-60 minutes after injury, as microglia migrate towards the source of ATP at the site of the injury (88). Alongside these morphological changes, amoeboid microglia also undergo a notable shift in gene expression patterns. These cells are more likely to express genes related to cell cycle progression, migration, and phagocytosis (89).

Peripheral immune response: cytokines and chemokines

After ischemic brain damage, brain-generated DAMPs (danger-associated molecular patterns) and cytokines leak into the circulation through disrupted BBB or cerebrospinal fluid (CSF) drainage lymphatic pathways (90). These molecules activate systemic immunity, peripheral immune cells, neurohumoral pathways (91) and immune response in lymphoid organs as well, triggering inflammation (92). Peripheral innate

immune cells, including neutrophils, monocytes, macrophages, and dendritic cells, as well as specific groups of lymphocytes such as NK cells and γδ T cells are rapidly activated by DAMPs, through leukocyte pattern recognition receptors, such as TLRs and RAGE (91). The response aims to eliminate the potential threat through a massive and indiscriminate humoral and cellular inflammatory reaction (93). In experimental stroke, this immune response is characterized by elevated serum cytokine levels and increased production of inflammatory mediators in circulating immune cells within hours after ischemia (94, 95). It is important to note that both central and peripheral cytokines contribute to brain injury after cerebral ischemia. (96).

Retrospective analyses have shown that a higher white blood cell count upon admission of acute ischemic stroke patients is linked to larger stroke volume, increased likelihood of hemorrhagic transformation, and unfavorable outcomes, including an elevated risk of 30-day mortality (97, 98). A recent meta-analysis from 2022 demonstrated that a high systemic immune-inflammation index (SII), calculated as neutrophils × platelets/lymphocytes (a marker indicating the inflammatory and immune status of patients and derived from routine blood tests), is significantly associated with poor patient outcomes, increased mortality, and a higher incidence of hemorrhagic transformation (99). A prospective clinical trial involving 697 consecutive patients, concluding in 2024, reported that the systemic immune-inflammation index independently predicts early stroke progression in patients with acute ischemic stroke (100).

It has long been observed that IL-6 levels on admission of stroke patients, as a marker of the systemic inflammatory status, are associated with early clinical deterioration (101). Peak plasma IL-6 levels and other peripheral markers of inflammation within the first week of ischemic stroke are correlated with brain infarct volume, stroke severity, and long-term outcomes. These data suggest that the extent of the peripheral inflammatory response correlates with the severity of acute ischemic stroke and influences clinical outcomes (102).

IL-10 is a well-known anti-inflammatory cytokine that has been demonstrated to be protective in experimental stroke models (103, 104). As source of IL-10 in stroke, T-cells, especially Treg cells, macrophages, microglia (103), B cells (105) and astrocytes (106) have been identified. Based on human data, we know that reduced serum levels of

the anti-inflammatory IL-10 have been independently associated with clinical severity at admission, neurological worsening (107), and poor functional prognosis in ischemic stroke patients (108).

In humans, the gene expression profile of circulating innate immune cells changes rapidly within the first few hours of stroke, as part of the systemic immune response (109). Acute ischemic stroke triggers a profound gene expression response in peripheral blood mononuclear cells (PBMCs), with a significant number of upregulated genes involved in the activation and differentiation of white blood cells. Within this group, some genes facilitate cell adhesion, while others encode enzymes responsible for cell membrane remodeling, preparing leukocytes for a more differentiated state (110). Interestingly, although PBMCs themselves were not hypoxic, elevated levels of hypoxia-related genes were, potentially due to local or systemic signaling from the brain (110, 111).

Mechanisms of stroke-associated brain edema

In case of **cytotoxic cerebral edema** also known as cellular edema extracellular water passes into cells, causing them to swell (112). This process is typically triggered by ischemia or excitotoxicity (113), cells lose the ability to maintain ATP-dependent sodium/potassium (Na+/K+) membrane pumps. These pumps normally maintain a low intracellular and high extracellular concentration of sodium ions (114). When cellular energy supply is compromised, these pumps cease to operate leading to an accumulation of sodium ions inside the cell, drawing water along the osmotic gradient. This, in turn, leads to intracellular fluid accumulation, cellular swelling and reduction of the extracellular volume (115, 116). Once cytotoxic edema has developed and provided there is some reperfusion of blood in the capillaries, a sodium concentration gradient forms. This gradient extends from the capillary lumen, crossing the endothelium into the extracellular space. Sodium ions stream into the extracellular space from the capillaries, drawing water along with them. This passage of water and sodium from capillaries into the brain parenchymal extracellular space is called **ionic edema** (117). It is therefore the ionic edema which is practically responsible for the tissue swelling seen in ischemic infarcts, not cytotoxic edema which is merely a redistribution of water and sodium from the extracellular to the intracellular compartment. It is important to mention that tissue swelling requires an influx of fluid, hence necessitating some blood flow. Observations

have long indicated that reperfusion promotes swelling, and notably, the swelling is less pronounced in the center of infarct cores compared to the periphery (114). Cytotoxic and ionic edema is distinguished from vasogenic edema by the intactness of the blood-brain barrier as well. In the former, there is no involvement of altered capillary permeability or endothelial dysfunction (117). **Vasogenic cerebral edema** occurs when the blood brain barrier is disrupted. This type of edema arises from the breakdown of tight endothelial junctions that constitute the blood-brain barrier, either due to physical disruption or release of vasoactive compounds. As a result, intravascular proteins and fluid exude from the capillaries into the extracellular space. Mass effect from edema can reduce cerebral perfusion pressure, leading to further ischemia and cytotoxic edema (117). It is important to recognize that cytotoxic, ionic and vasogenic edema occur simultaneously in stroke (118).

N,N-Dimethyltryptamine (DMT) and the sigma-1 receptor

N,N-Dimethyltryptamine (DMT) is a well-known, long-studied, and abundant molecule in nature, found endogenously in plants, animals, and humans, and is best known for its hallucinogenic properties. DMT, was originally known as the active compound of the ayahusaca brew, a traditional spiritual medicine used by indigenous people in the Amazonian basin (119). Since then, it has been documented that rat brain is endogenously capable of synthesize DMT in concentration comparable to canonical neurotransmitters like serotonin and that experimental cardiac arrest significantly increased the DMT level in the brain, however its physiological function is not fully understood (120, 121). The pharmacokinetic profile and psychedelic properties of intravenous DMT are well established in humans as well. In case of intravenous administration, DMT rapidly cross the blood-brain-barrier (122) and shows a rapid clearance via MAO-A metabolism (123) with a documented early plasma elimination half-life of 5.0–5.8 minutes, followed by longer late elimination half-life of 14–16 min after 15–20 min (124, 125). When administered, it exerts a complex and profound effect on the psyche, interacting with multiple receptor systems, including serotonin receptors (primarily the 5-HT1A, 5-HT2A, and 5-HT2C subtypes), as well as glutamatergic, histaminergic, dopaminergic, trace amine–associated, and sigma receptors, with varying affinities (126, 127).

Sigma-1 receptor (S1R) is an intracellular chaperone between the endoplasmic reticulum and mitochondria, interfering with calcium homeostasis (128) but can translocate to the plasma membrane interacting with ion channels as well (129). In this regard, it is involved in the transmission of endoplasmic reticulum stress to the nucleus and regulates cellular excitability (126). Given the central role of sigma-1 receptor in the stress reaction of cells, its pharmacological modulation was abundantly investigated in experimental stroke models, with diverse treatment effects ranging from decreased lesion size to improved neurological function (130). A specific sigma-1 receptor agonist was even studied in a phase II human trial during the subacute phase of stroke, but no significant effects on functional endpoints were observed (131).

DMT was showed to have beneficial properties in cell protection and structural and functional neuroplasticity as well. Via sigma-1 receptor, DMT robustly increased the survival of in vitro cultured human cortical neurons and dendritic cells in severe hypoxia (132). DMT treatment activates neural stem cell proliferation, neuroblast migration and generation of new neurons in adult rat brain on a sigma-1 receptor mediated way, (and not in 5-HT2A mediated way) (133) and promotes neuroplasticity in vitro and in vivo by enhanced neuritogenesis, spinogenesis, dendritogenesis and synaptogenesis in an intracellular 5-HT2A mediated pathway (134, 135).

Considering that in 2014 a phase II randomized, placebo-controlled trial of the selective sigma-1 receptor agonist cutamesine in post-stroke patients did not demonstrate improvement in functional outcomes within the first 56 days (131), and that fluoxetine—a sigma-1 receptor ligand of moderate affinity—administered for six months after stroke also failed to produce clinically relevant benefits on long-term (12-month) functional recovery in three parallel-running, large-scale randomized controlled trials (FOCUS (136), AFFINITY (137), and EFFECTS (138)), the therapeutic potential of selective sigma-1 receptor modulation in human stroke—despite the highly promising preclinical findings—remains questionable.

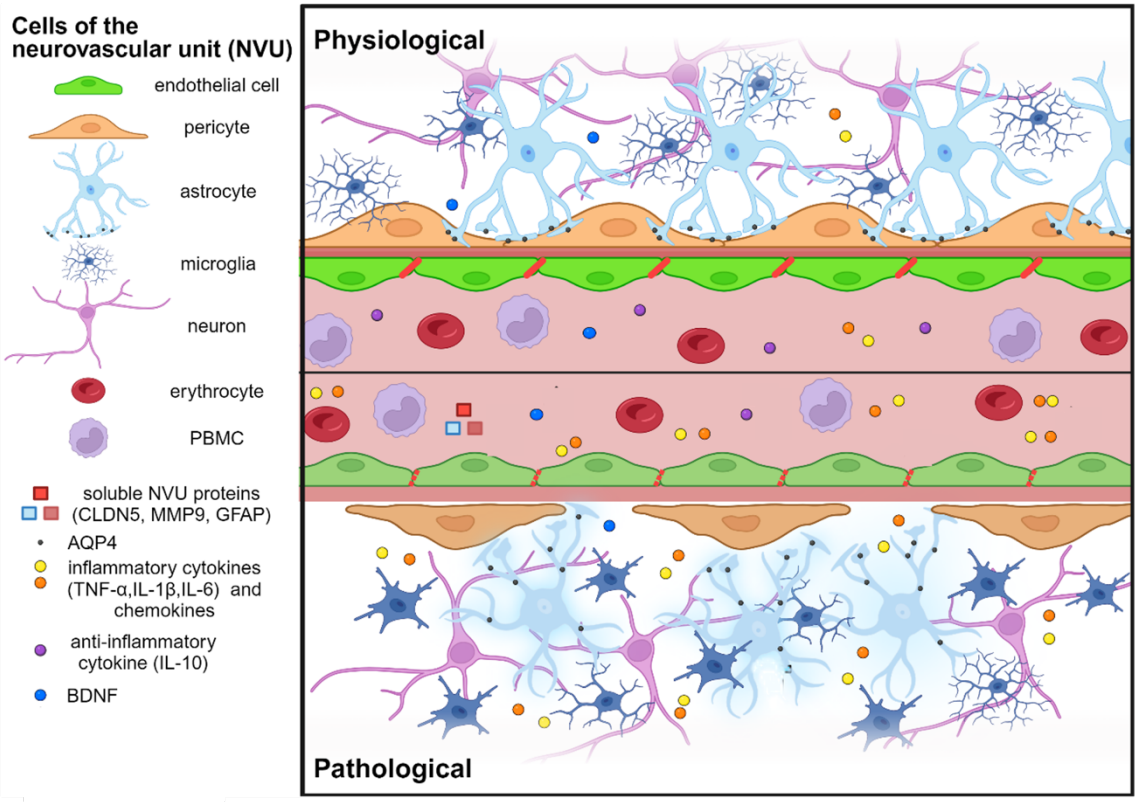

Fig. 1. Schematic of the blood–brain barrier under physiological and pathological condition

2. Objectives

Upon examining the extensive network of cells, pathways, mechanisms, interactions, and feedback loops involved in stroke pathogenesis, it appears challenging to improve stroke outcomes by manipulating just one component, as evidenced by the failure of such approaches in clinical translation. Based on the previously described scientific background, our research group aimed to investigate the cytoprotective effects of N,N-dimethyltryptamine, an endogenous compound capable of exerting pleiotropic effects through various receptor types, under ischemia-reperfusion conditions using an in vivo rat model of transient cerebral ischemia. Our goal was to assess whether DMT treatment starting at the timepoint of reperfusion exerts a **neuroprotective** effect in the post-ischemic brain, and if yes, to determine how this protection relates to the integrity of the **blood-brain barrier**, the extent of stroke-associated cerebral **edema**, and the modulation of **neuroinflammation**, including microglial activation and peripheral immune responses. Furthermore, our objective was to investigate the potential of DMT to promote **neurorestoration** following stroke, which from a clinical perspective represents the key determinant of long-term recovery and therapeutic relevance.

In addition to the in vivo experiments, we employed an in vitro triple co-culture model of the blood-brain barrier, consisting of endothelial cells, astrocytes, and pericytes to further dissect the mechanisms underlying BBB protection and cell survival, including the effects of DMT on the endothelial transcriptome under ischemic conditions.

Given DMT's interaction with multiple receptor systems, an important objective was to determine which effects are attributable to sigma-1 receptor activation and which are sigma-1–independent.

3. Methods

In vivo

Animal model and treatment protocol

All experimental procedures complied with the ARRIVE recommendations as well as with the directives of the European Communities Council (86/609 EEC and 2010/63/EU). The study protocol received approval from the Animal Care and Use Committee of Semmelweis University (XIV-I-001/29–7/2012) and from the Department of Animal Health, Government Office of Pest County, Hungary (PE/EA/01445-6/2022). Data acquisition and analysis were performed under blinded conditions. Humane endpoints were predefined according to the IMPROVE Guidelines (139). Data analysis was carried out by investigators blinded to the group allocation. Transient middle cerebral artery occlusion (MCAO) was induced in male Wistar rats (Toxi-Coop Ltd., Budapest, Hungary; body weight: 280 ± 20 g) under continuous isoflurane anesthesia (Harvard Apparatus, Holliston, MA, USA). After surgical exposure of the right internal carotid artery, a filament was advanced while monitoring regional cerebral blood flow within the right MCA territory using Laser-Doppler Flowmetry (Perimed Inc., Stockholm, Sweden). Only animals exhibiting at least a 40% reduction in perfusion were randomized into the treatment groups (Fig. 5). The ischemic period was maintained for 60 minutes (140). Administration of N,N-dimethyltryptamine (DMT, Sigma-Aldrich, St. Louis, MO) was initiated immediately prior to filament withdrawal by intraperitoneal injection of DMT (1 mg/kg bw), prepared in 0.1 ml of 70% ethanol and subsequently diluted to a final volume of 1 ml with physiological saline. This was followed by continuous delivery of DMT at a rate of 2 mg/kg bw/h for 24 hours using intraperitoneally implanted osmotic pumps (Alzet, ALZA, Palo Alto, CA). This approach was chosen because DMT is metabolized very rapidly; by combining a bolus with an infusion we aimed to maintain a stable serum level throughout the critical hours after reperfusion. The dose was selected based on prior literature. A technical consideration was to dissolve crystalline DMT in alcohol to prepare the most concentrated solution possible for the 200 μL reservoir of the osmotic pump. This resulted in a maintenance dose of 2 mg/kg/h, which reliably falls within the psychedelic range. In humans, a rapid i.v. bolus of approximately 0.2 mg/kg already produces a psychedelic, fast-onset experience lasting about 20–30 minutes. At 0.1 mg/kg

it typically yields a pleasant somatosensory experience, and below this dose the regimen can be considered sub-psychedelic.

Control animals received an equivalent vehicle bolus without DMT. In the sigma receptor antagonist arm, rats were co-administered 1-(3,4-Dichlorophenethyl)-4-methyl-piperazine dihydrochloride (BD1063, 2 mg/kg bw/24 h; Axon Medchem BV, Groningen, The Netherlands) through separate osmotic pumps, in addition to intraperitoneal boluses of both DMT and BD1063 (1 mg/kg bw each). The dosing regimen was established based on prior in vivo studies (141). For cytokine analyses and PBMC assays, sham-operated groups were included, in which animals underwent an incision over the right carotid artery and abdominal opening identical to the surgical preparation in treated cohorts. For tissue and blood collection, anesthesia was induced intraperitoneally using a ketamine (50 mg/kg bw) and xylazine (4 mg/kg bw) mixture. Blood samples were obtained following aortic cannulation. Peripheral blood mononuclear cells (PBMCs) were isolated using mononuclear cell preparation tubes (BD Vacutainer CPT, product no. 362782). Brains were fixed by transaortic perfusion with 4% paraformaldehyde in 0.1 M PBS. Subsequently, the specimens were immersed in 30% glucose solution for two days before free-floating coronal sections of 40 μm thickness were prepared with a microtome (Leica SM2000R, Nussloch, Germany) (142).

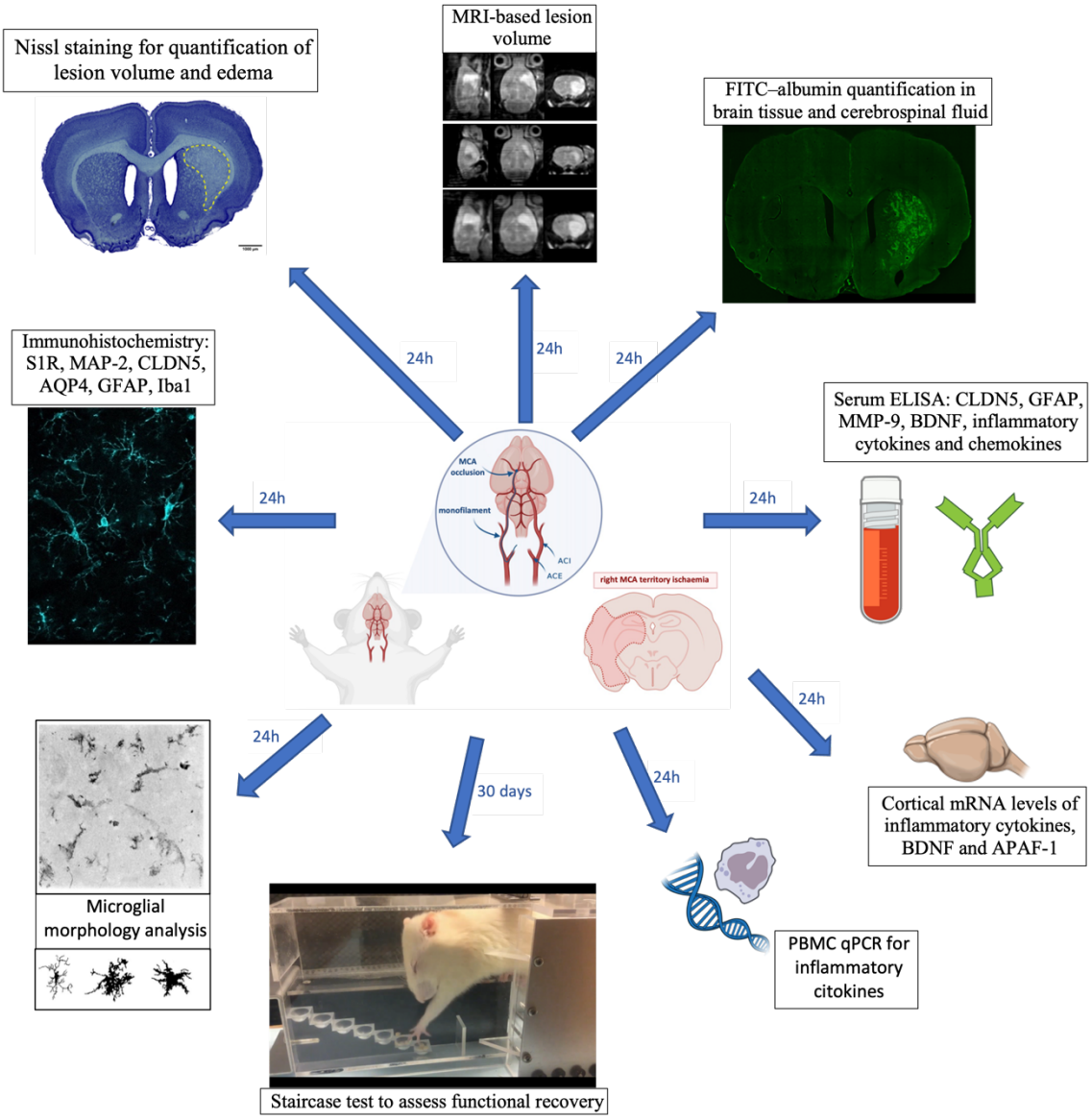

Fig. 2. Overview of the in vivo experimental workflow after 1 h tMCAO, followed by either 24 h reperfusion with specimen processing or 30-day functional recovery assessment. All experimental animals underwent tMCAO-induced stroke. Experimental groups included a control group (no DMT treatment), a DMT-treated group, and a combined BD1063 + DMT-treated group.

Lesion volume and edema measurement

Cresyl violet (Nissl) staining was applied using a routinely employed histological procedure (143). In brief, tissue sections were immersed for 90 minutes in a solution consisting of cresyl violet (0.1 g), glacial acetic acid (0.2 ml), and distilled water (100 ml) adjusted to pH 3.2. Subsequently, the samples were rinsed in 96% ethanol, dehydrated,

and cleared sequentially with isopropanol and xylene. Mounting and coverslipping were then performed. Histological volumes were determined using the following formula: sum of the cross-sectional areas of the regions of interest × number of slices × section interval. Cerebral edema was quantified as: (volume of the ipsilateral hemisphere – volume of the contralateral hemisphere) / volume of the contralateral hemisphere. Edema-corrected lesion volume was calculated by the equation: infarct volume × (1 – volume of edema) (144, 145). Slides were captured on a Zeiss Axioscan 7 Microscope Slide Scanner (Karl Zeiss AG, Oberkochen, Germany), and processed with the QuPath software package (version 0.5.1) (142).

MRI measurement of lesion volume

MRI examinations were carried out in rats anesthetized with 2% isoflurane using a NanoScan® 1 T MRI system (Mediso Ltd., Budapest, Hungary), equipped with an actively shielded 450 mT/m gradient and volume coils for both transmission and reception. For anatomical imaging, a T2-weighted fast spin echo (FSE) sequence was applied in a three-dimensional acquisition mode covering a 38.4 × 48 × 48 mm field of view. Sequence parameters included a repetition time/echo time of 2000/59.2 ms (2000/78.9 ms in the treated + antagonist group), a dwell time of 25 μs, and two excitations, yielding a total acquisition time of 25 min 44 s. Brain segmentation into three-dimensional volumes of interest (left and right hemispheres) was performed using VivoQuant software (inviCRO, Boston, MA) (141).

Quantitative MRI image analysis

The volume of T2 hyperintense regions detected 24 h after ischemic stroke provides a reliable approximation of the eventual infarct core (146). To quantify the T2-positive lesion volume within the MRI dataset, voxel intensity histograms of both hemispheres were generated using the histogram function of the VivoQuant software (inviCRO, Boston, MA). The discrepancy between the histograms of the right (stroke-affected) and left hemispheres reflected the presence of ischemic injury. The number of voxels corresponding to the lesion was then multiplied by the voxel size to obtain the final cerebral lesion volume (141).

Functional testing using the “staircase method”

Animals were kept in groups of four under standard housing conditions with a 12 h light/dark cycle and a controlled ambient temperature of 22 ± 2 °C. Water was available ad libitum, while food was restricted to a daily portion of 10–15 g of standard laboratory chow. The behavioral test apparatus (Campten Instruments Ltd., Loughborough, UK) consisted of a chamber with a central platform accessible by the animal, with seven steps positioned on each side. Two standard food pellets were placed on each step, resulting in 14 pellets per side. Training was performed once daily for six days per week over a 14-day period prior to the experiment. During each trial, rats remained in the staircase boxes for 10 minutes, after which the numbers of pellets consumed, dropped, or left on the steps were recorded. Only those animals that successfully learned to collect at least eight pellets with their left forepaw on the final two consecutive training days were included in the post-stroke phase. Following induction of stroke, testing continued according to the same protocol on every post-stroke day for the first two weeks, and subsequently every fourth day until day 30 (141, 147) (Fig. 3 and Fig. 4).

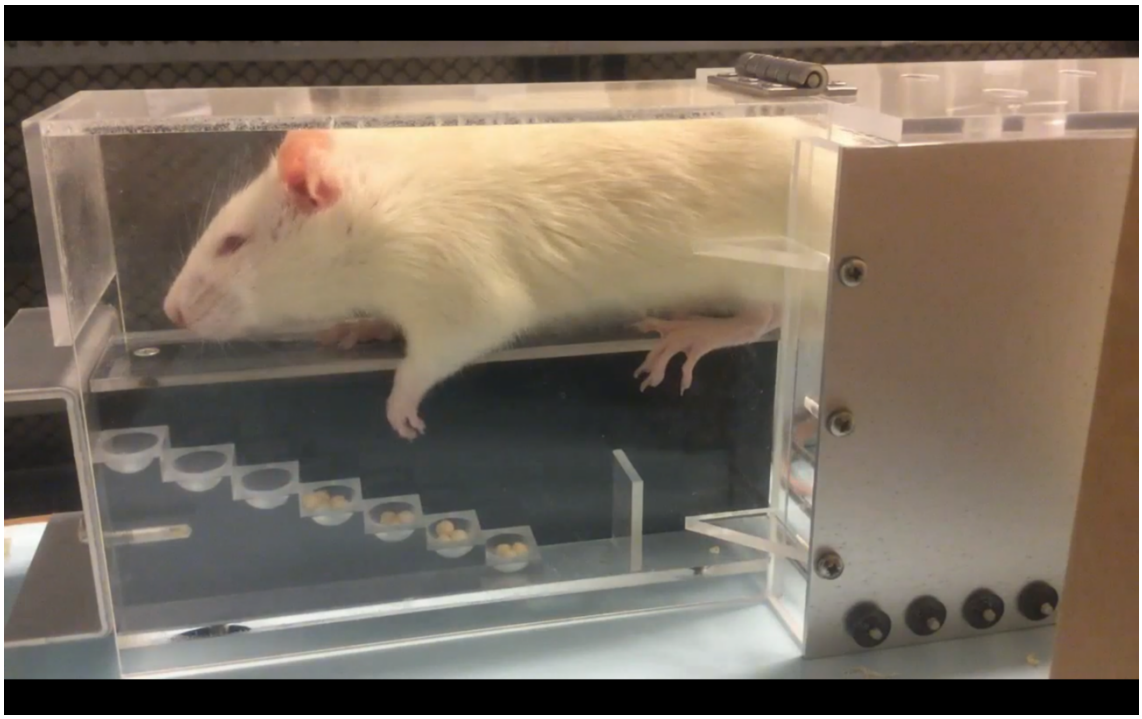

Fig. 3. Representative example of a control rat 30 days after stroke
The animal exhibits persistent motor impairment of the left forelimb, being unable to grasp and consume food pellets, and instead merely displacing them.

Fig. 4. Representative example of a DMT-treated rat 30 days after stroke
The animal exhibited markedly improved motor performance with the affected left forelimb compared to the control group, being capable not only of gross motor movement but also of fine motor control, as demonstrated by its ability to grasp and consume the food pellets.

Blood-brain barrier permeability *in vivo*

FITC-albumin visualization and quantification in CSF: To assess blood–brain barrier integrity, 21 animals (n = 7 per group) received an intravenous injection of 1 ml FITC-albumin solution (20 mg in 1 ml 0.9% NaCl; Sigma, Saint Louis, MO, USA, product no. A9771) through the lateral tail vein one hour prior to sacrifice. Following one hour of circulation, cerebrospinal fluid (CSF) was collected from the cisterna magna using a stereotaxic frame (Harvard Apparatus, Holliston, MA, USA) in combination with a 100 µl Hamilton HPLC syringe (Hamilton Company, Reno, NV, USA). Brains were subsequently fixed via transcardiac perfusion with 4% paraformaldehyde prepared in 0.1 M phosphate buffer (148). Free-floating sections (40 µm thick) were prepared from the fixed brains. FITC-albumin was visualized in the brain tissue using a 780 LSM confocal laser-scanning microscope (Karl Zeiss AG, Oberkochen, Germany), and fluorescence

intensity was expressed in arbitrary units. For the control hemisphere, two images per animal were acquired (n = 14 images per group), whereas for the ischemic hemisphere ten images per animal were collected (n = 210). Quantification of FITC-albumin levels in CSF samples (n = 5 per group) was performed by fluorescence spectroscopy with excitation at 495 nm and emission at 520 nm, using a Multiskan Sky microplate reader (ThermoFisher Scientific, Waltham, MA). Fluorescence intensity measurements were normalized to the injected FITC-albumin stock solution, which was set to 100% (142).

Brain section immunohistochemistry 1: S1R, MAP-2, IBA-1

Immunohistochemical procedures, including chromogenic and multiple immunofluorescence labeling, were performed according to previously published methods (149). Free-floating sections were pre-treated to facilitate antibody penetration, and non-specific binding was blocked. For single-labeling experiments, sections were incubated for 72 h at 4 °C with anti-S1R primary antibodies (1:500, ABCAM, Cambridge, MA; catalog no. AB53852), followed by the application of appropriate secondary antibodies and avidin–biotin complexes containing horseradish peroxidase. Immunoreactivity was visualized with 3,3′-diaminobenzidine as chromogen, intensified using Ni-ammonium sulfate in the presence of H_2O_2 as substrate. For multiple immunofluorescence labeling, anti-S1R antibodies were combined with two cell-specific markers: anti-MAP-2 (1:200, Sigma-Aldrich, St. Louis, MO; catalog no. M4403) for neurons and IBA-1 (1:100, Novus Biologicals, Centennial, CO; catalog no. NB100–1028) for microglia. Signals were detected with carbocyanine-tagged secondary antibodies (2, 3, or 5). Chromogenic staining results were captured on a BX-51 microscope (Olympus, Tokyo, Japan) at 5× magnification. Sections subjected to multiple immunofluorescence labeling were examined on a 780 LSM confocal laser-scanning microscope (Karl Zeiss AG, Oberkochen, Germany); high-resolution images were acquired with a 3× optical zoom at 63× magnification (Plan-Apochromat 63×/1.40), using pinhole settings restricting detection to 0.5–0.7 μm optical thickness. Multipanel images were assembled using CorelDraw X5 (Corel Corp., Ottawa, Canada) (141).

Brain section immunohistochemistry 2: CLDN5, GFAP, AQP4, IBA1

CLDN5 immunostaining

For immunostaining, three brain sections per animal from five animals per group were analyzed (free-floating sections, 40 μm; total of 15 sections per group). Sections were washed three times for 10 minutes each in PBS on a horizontal shaker. Cell membrane permeabilization was achieved by incubating the samples in PBS within a 98 °C water bath for 1 hour, followed by cooling to room temperature (RT). Blocking was performed for 2 hours at RT using a solution containing 2% normal horse serum (NHS), 0.3% BSA, and 0.5% TX-PBS. Sections were then incubated overnight (ON) at 4 °C with anti-CLDN5 primary antibody diluted in the blocking buffer. After three PBS washes on the following day, sections were incubated for 2 hours at RT with A594 anti-rabbit secondary antibody diluted in PBS. Samples were subsequently washed three more times in PBS, and nuclei were counterstained with Hoechst 33342 for 15 minutes at RT. A final wash in double-distilled water was performed before mounting the sections on glass slides with Confocal Matrix (Micro Tech Lab, Graz, Austria). Imaging was carried out using a confocal microscope (142).

GFAP-AQP4 immunostaining

Between each step, brain sections were washed identically to the CLDN5 immunostaining protocol. Permeabilization was carried out in 1% Triton-X-PBS for 10 minutes, followed by incubation in a blocking solution containing 2% NHS, 0.3% BSA, and 0.5% TX-PBS. Sections were then exposed overnight (ON) at 4 °C to goat anti-GFAP primary antibody. For double-labeling experiments, the primary antibodies were applied sequentially. On the second day, after washing, anti-goat A488 secondary antibody was applied for 2 hours at room temperature (RT). This was followed by overnight incubation at 4 °C with rabbit anti-AQP4 primary antibody. On the third day, sections were washed and then incubated with anti-rabbit A594 secondary antibody for 2 hours at RT. Nuclei were counterstained for 15 minutes at RT, followed by final washes, after which the sections were mounted in the same way as described for CLDN5 staining (142).

IBA1 immunostaining

Between each step, brain sections were washed in the same manner as described for the previous immunostainings. Permeabilization was carried out in two phases: first, sections were incubated in 0.01 M citrate buffer in a 70 °C water bath for 20 minutes,

followed by PBS washes and an additional permeabilization step in 0.5% Triton-X-PBS for 30 minutes. After washing, blocking was performed with 2% NHS, 0.3% BSA, and 0.5% TX-PBS, after which goat anti-IBA1 primary antibody was applied overnight (ON) at 4 °C. On the second day, samples were incubated with anti-goat A488 secondary antibody for 2 hours at room temperature (RT). Following the washes, nuclear counterstaining was performed for 15 minutes at RT. After a final wash, sections were mounted in the same manner as for CLDN5-stained samples (142).

Confocal microscopy

Immunolabeling for CLDN5 was captured as single-plane images using a confocal laser-scanning microscope (Olympus Fluoview FV1000, Olympus Life Science Europa GmbH, Germany). In contrast, GFAP, AQP4, and IBA1 immunoreactivities were analyzed on a spinning disk confocal microscope (Zeiss, Germany), generating image stacks of 15–20 optical sections. The confocal laser-scanning microscope was configured with the following parameters: objective lens UPLSAPO 60×, numerical aperture (NA) 1.35; sampling speed 4 μs/pixel; sequential unidirectional scanning mode; excitation wavelengths 405 nm (DAPI) and 543 nm (Alexa 594). The spinning disk confocal microscope was set up as follows: PlanApoN 60× objective lens, NA 1.42; camera binning 1; Z-step size 0.3 μm; excitation wavelengths 405 nm (Hoechst 33342), 488 nm (Alexa 488), and 543 nm (Alexa 594) (142).

Brain section immunohistochemistry image analysis

Original images were segmented to isolate single microvessels, microglia, or astrocytes. These segmented images were subsequently processed using Matlab (MathWorks, Natick, MA, USA). Image contrast was first optimized by histogram equalization. Grayscale images were then converted to binary format, and objects smaller than four pixels were excluded. In the binary images, pixel counts represented the area of the labeled structures, whereas total fluorescence intensities were obtained by masking the grayscale images with their respective binary masks. Each total intensity value was normalized to the corresponding area (142).

Analysis of microglia morphology

Microglial morphology at the single-cell level was assessed according to the protocol of Fernández-Arjona and colleagues (2017) (150). IBA1-immunostained sections were examined using a Spinning Disk Confocal Microscope to identify the brain region affected by experimental stroke, with the corresponding contralateral area serving as control. For each animal, ten images were captured from both the control and stroke-affected hemispheres by an investigator blinded to group allocation. In total, 300 images were obtained across three experimental groups (5 animals per group). Altogether, 553 individual microglial cells were identified from both hemispheres across the experimental groups. Single-cell images were extracted in Photoshop CS4 (Adobe, San Jose, CA, USA), where contrast and brightness were adjusted to optimize visualization of cell structures. The images were then converted into binary format using ImageJ, and further corrected in Photoshop CS4 to ensure that all microglial processes were represented as continuous lines. Morphological parameters—including fractal dimension, lacunarity, density, span ratio, maximum span across the convex hull, area, perimeter, circularity, maximum and minimum radii, and mean radius—were quantified from the processed cell profiles. These analyses were performed using the Box Counting Fractal Analysis method implemented in the FracLac plugin of ImageJ (151). Data were first normalized and subsequently analyzed using the Weka Explorer data mining software package (152). In the final step, expectation–maximization clustering was applied to partition the dataset into three distinct clusters (153), and the distribution of these clusters was then evaluated across the experimental groups (142).

Brain Tissue Sampling for mRNA Expression Analysis

At 25 h after MCAO, animals were sacrificed by decapitation and brains were rapidly removed. Coronal sections of 2 mm thickness were prepared from fresh brain tissue using a rat brain matrix (Harvard Apparatus, Boston, MA), beginning 6 mm caudal to the frontal pole. The first coronal slices were subjected to TTC staining, after which tissue from the lesion border zone was isolated with a punch biopsy needle. Samples were preserved in RNAlater solution and stored at −80 °C. Blood serum was collected by direct puncture of the aorta, centrifuged at 1200 RPM for 5 minutes, and stored at −80 °C until further assays were performed (141).

RNA isolation, cDNA synthesis and qPCR from brain samples

RNA was extracted from rat brain tissue using TRIzol reagent (Invitrogen, Carlsbad, CA) following the manufacturer's instructions, applying a 10:1 TRIzol-to-tissue volume ratio to account for the high lipid content. RNA yield was determined by UV spectrophotometry with a NanoDrop1000 instrument (ThermoFisher Scientific, Waltham, MA). Integrity was assessed on an Agilent BioAnalyzer (Agilent Technologies, Santa Clara, CA), and only samples with an RNA integrity number (RIN) above 7.5 were included for further processing. For cDNA synthesis, 1 μg of RNA per sample was reverse transcribed using the High Capacity cDNA Reverse Transcription Kit (Applied Biosystems, Foster City, CA). Gene expression levels were quantified with gene-specific TaqMan assays (Applied Biosystems, Foster City, CA). Normalization was performed using the ΔCt method, with PPIA (Cyclophilin A) serving as the reference gene (154). Quantitative PCR was carried out on the ABI StepOne Real-Time PCR System, and threshold cycle (Ct) values were calculated with StepOne v2.1 software (Applied Biosystems, Foster City, CA) (141).

RNA isolation, cDNA synthesis and qPCR from PBMC pellets

Total RNA was extracted from PBMC pellets using TRIzol reagent (Invitrogen, Waltham, MA) according to the manufacturer's instructions. RNA yield was quantified by UV spectrophotometry on a NanoDrop One instrument (ThermoFisher Scientific, Waltham, MA), and integrity was assessed with an Agilent BioAnalyzer (Agilent Technologies, Santa Clara, CA). Only samples with RIN values greater than 8 were included in subsequent analyses. For cDNA synthesis, 1 μg RNA from each sample was reverse transcribed using the High Capacity cDNA Reverse Transcription Kit (ThermoFisher). Target gene expression levels were determined using TaqMan Real-Time PCR Assays (ThermoFisher). Data were normalized by the ΔCt method with PPIA (cyclophilin A) as the reference gene. Statistical analyses were performed in GraphPad Prism software, applying the non-parametric Wilcoxon paired test to compare conditions and identify significantly altered expression patterns. A p-value of < 0.05 was considered statistically significant (142).

Serum CLDN5, matrix metalloproteinase-9 (MMP9) and GFAP ELISA

Serum concentrations of CLDN5, MMP9, and GFAP were measured using rat-specific ELISA kits: CLDN5 (Elabscience, cat# E-EL-R2502), MMP9 (Elabscience, cat# E-EL-R3021), and GFAP (Elabscience, cat# E-EL-R1428). Blood was collected with EDTA-Na_2 as anticoagulant, and samples were centrifuged at 1000 × g for 15 minutes at 2–8 °C within 30 minutes of collection. Serum from nine animals per group was analyzed in duplicate, applying 100 µl per well for each assay. Following sample loading, assays were performed strictly according to the manufacturers' instructions. Absorbance was read at 450 nm on a Multiskan EX microplate reader (Thermo Scientific, cat# 51118170) (142).

Preliminary assessment of circulating biomarkers (without S1R antagonist and sham groups)

Plasma samples from all rats were analyzed for IL-1β, IL-6, TNF-α, IL-10, and BDNF using high-sensitivity rat ELISA kits (ThermoFisher, Waltham, MA; catalog numbers: BMS630, BMS625, BMS622, BMS629, ERBDNF), and for APAF1 with a rat ELISA kit (LSBio, Seattle, WA; catalog number: LS-F8140–1), according to the manufacturers' protocols. The assay volume was 25 µl. Standard ranges were as follows: 31.3–2000 pg/ml (IL-1β and IL-6), 39.1–2500 pg/ml (TNF-α), 15.6–1000 pg/ml (IL-10), 12.29–3000 pg/ml (BDNF), and 0.156–10 ng/ml (APAF1). Analytical sensitivities were 4.0 pg/ml (IL-1β), 12.0 pg/ml (IL-6), 11.0 pg/ml (TNF-α), 1.5 pg/ml (IL-10), 12 pg/ml (BDNF), and 0.156 ng/ml (APAF1). Before measurement, samples were thawed and diluted 1:2 (IL-1β, IL-6, TNF-α, BDNF, APAF1) or 1:4 (IL-10). Each sample was assayed in triplicate, and mean values were used for statistical evaluation. Intra- and inter-assay coefficients of variation were <10% and <12%, respectively. Absorbance was read at 450 nm on a Synergy HT microplate reader (Bio-Tek Instruments, Winooski, VT) (141).

Comprehensive assessment of circulating biomarkers

Cytokine, chemokine, and neurotrophin concentrations in rat serum and culture supernatants were determined using OptEIA kits (BD Biosciences, Franklin Lakes, NJ) and high-sensitivity ELISA assays for IP-10 and CINC-1/CXCL1 (ThermoFisher),

following the manufacturers' protocols. The precision of the assays was specified as follows: intra-assay coefficient of variation (CV) < 10% and inter-assay CV < 12% (CV% = SD/mean × 100) (142).

In vitro

Cell Cultures

According to previously established methods, primary rat brain endothelial cells (RBECs), pericytes (RPCs), and glial cells were isolated and cultured (155, 156). Briefly, RBECs were isolated from 4-week-old outbred Wistar rats of both sexes and plated onto culture dishes (Corning Costar, New York, NY, USA) pre-coated with 100 µg/ml collagen type IV (Sigma-Aldrich, cat# C5533) and 25 µg/ml fibronectin (Sigma-Aldrich, cat# F1141). Cells were maintained in DMEM/HAM's F-12 medium (Gibco, Waltham, MA, USA) supplemented with plasma-derived bovine serum (PDS, First Link, Wolverhampton, UK; 15% for the first 3 days, then reduced to 10%), 10 mM HEPES, 100 µg/ml heparin, 5 µg/ml insulin, 5 µg/ml transferrin, 5 ng/ml sodium selenite (ITS, Pan-Biotech, Aidenbach, Germany), 1 ng/ml basic fibroblast growth factor (bFGF), and 50 µg/ml gentamicin. Cultures were kept at 37 °C in a humidified atmosphere containing 5% CO_2. To remove contaminating cell populations lacking P-glycoprotein expression, the medium was supplemented with 3 µg/ml puromycin during the initial 3 days of culture (156). Following isolation, pericytes were seeded onto culture dishes (VWR International, Radnor, PA, USA) coated with 100 µg/ml collagen type IV. Glial cells were obtained from newborn rats and plated in uncoated 75 cm^2 flasks (TPP, Trasadingen, Switzerland). As previously reported, the resulting glial cultures consisted of approximately 80% astrocytes and 20% microglial cells (157). Both pericytes and glial cells were cultured in low-glucose DMEM medium (Gibco, ThermoFisher) supplemented with 10% fetal bovine serum (FBS, Pan-Biotech, Aidenbach, Germany) and 50 µg/ml gentamicin (142).

Oxygen-glucose deprivation and reoxygenation model

To mimic hypoxic conditions, cells were subjected to 6 hours of oxygen–glucose deprivation (OGD) followed by 24 hours of reoxygenation (OGDR) (Fig. 12A). The timing of this experimental paradigm was adapted from the study of Sato et al., 2022

(158). A dedicated O_2/CO_2 incubator (PHCBI MCO-50M) was used to establish an atmosphere of 1% O_2 and 5% CO_2. Prior to the 6-hour OGD period, oxygen was removed from the serum- and glucose-free DMEM/F12 medium (Biowest, cat# L0091) supplemented with Glutamax (Gibco) by bubbling with N_2 gas. Control cells were maintained under normoxic conditions in a humidified incubator with 5% CO_2 using the standard culture medium described above, throughout the same 6+24-hour protocol. This group is referred to as "normoxia" (Fig. 12A). At the onset of the 24-hour reoxygenation phase, 200 µM DMT, with or without 2 µM BD1063, was added to the culture medium (142).

Impedance-based measurement of endothelial cells, pericytes and glial cells

Real-time impedance-based cell analysis was carried out in specialized 96-well plates with integrated gold electrodes (E-plate 96; Agilent, Santa Clara, CA, USA; cat# 300600910) using the xCELLigence RTCA SP system (Agilent). For RBECs, plates were coated with collagen type IV (100 µg/ml) and fibronectin (25 µg/ml), while for RPCs and glial cells only collagen type IV (100 µg/ml) was applied. Cell-free background impedance was recorded in culture medium for each well prior to seeding. Subsequently, 5×10^3 RBECs/well, 6×10^3 RPCs/well, and 6×10^3 glial cells/well were plated and cultured until confluency. Impedance of the cell layers was monitored at 10 kHz every 10 minutes. To promote barrier formation, confluent RBEC monolayers were pre-treated with 550 nM hydrocortisone for 24 h before OGDR exposure. The impedance readout, expressed as the cell index, reflects cell–cell contact integrity and adhesion strength, and is defined as $Zn - Z0$, where Zn is the impedance at a given time point and Z0 represents the cell-free background impedance. Cell index values were normalized to the final measurement obtained before OGDR treatment (142, 159).

Barrier integrity tests

Triple co-culture model

To assess barrier integrity, 8.5×10^4 RBECs and 1.5×10^4 RPCs were co-cultured on cell culture inserts (Corning, cat# 3460), while 2.5×10^4 glial cells were seeded on the bottom of the companion plate. Cultures were maintained under control conditions for 5

days before being subjected to OGDR (6-hour OGD followed by 24-hour reoxygenation). At the onset of reoxygenation, 200 µM DMT, with or without 2 µM BD1063, was added to the standard culture medium. Following OGDR, supernatants were collected and centrifuged at 700 × g for 5 minutes to remove cellular debris, then stored at −20 °C until analysis. RBECs were fixed with ice-cold acetone:methanol (1:1) for 2 minutes and immediately rehydrated in PBS containing 1% FBS. Glial cells were fixed separately with 4% paraformaldehyde (PFA) for 15 minutes at room temperature for subsequent immunocytochemistry (142).

Transendothelial electrical resistance measurement

To assess sodium ion permeability, transendothelial electrical resistance (TEER) was determined using an EVOM Volt-Ohm meter (World Precision Instruments Inc., Sarasota, FL, USA) equipped with STX-2 chopstick electrodes. Background resistance was recorded from inserts without cells and subtracted from the measured values. TEER values were then normalized to the surface area of the endothelial monolayer and expressed as $\Omega \times cm^2$, in line with our previous publications (142, 159).

Permeability measurement

Following the 24-hour reoxygenation period, barrier integrity was evaluated by assessing permeability to two fluorescent tracers: sodium fluorescein (SF, 10 µg/ml, MW = 376 Da) and Evans blue–conjugated albumin (EBA, 170 µg/ml, MW = 67 kDa). The assay was carried out in Ringer-Hepes buffer (118 mM NaCl, 4.8 mM KCl, 2.5 mM $CaCl_2$, 1.2 mM $MgSO_4$, 5.5 mM D-glucose, 20 mM HEPES, pH 7.4), following previously established protocols (159). The concentrations of SF and EBA in samples collected from the lower chamber were quantified using a Fluorolog 3 spectrofluorometer (Horiba Jobin Yvon). Permeability across cell-free inserts was also assessed. Endothelial permeability coefficients (Pe) were derived from tracer clearance values, following the methodology described in earlier works (142, 155).

Cell culture immunocytochemistry: CLDN5

Fixed RBECs were rinsed three times with phosphate-buffered saline (PBS) and subsequently blocked in 3% bovine serum albumin (BSA) prepared in PBS for 1 h at

room temperature (RT). The anti-CLDN5 primary antibody (see Table S1 for details) was diluted in the blocking solution and applied overnight (ON) at 4 °C. Following three PBS washes, cells were incubated for 1 h at RT with Alexa Fluor 488-conjugated anti-rabbit secondary antibody together with Hoechst 33342 nuclear stain, both diluted in PBS. After three additional PBS washes and a final rinse in distilled water (DW), membranes were excised, mounted on glass slides using Fluoromount-G (Southern Biotech, AL, USA; cat# 0100-01), and analyzed by confocal microscopy (142).

GFAP-IBA1 immunocytochemistry

GFAP–IBA1 immunocytochemistry was carried out in the same manner as CLDN5 immunostaining. Since glial cells were fixed with paraformaldehyde (PFA), membranes were permeabilized with 0.2% Triton X-100 (TX) for 10 min at 4 °C. After blocking, cells were incubated overnight (ON) at 4 °C with anti-GFAP and anti-IBA1 primary antibodies. This was followed by 1 h incubation at room temperature (RT) with anti-mouse Alexa Fluor 555 and anti-goat Alexa Fluor 488 secondary antibodies. Following the final washing step, cells were mounted using Fluoromount-G (142).

Cell culture immunocytochemistry image analysis

CLDN5 and GFAP–IBA1 fluorescence images were acquired using a Leica TCS SP5 confocal laser scanning microscope (Leica Microsystems, Wetzlar, Germany). To ensure comparability of staining intensity, all images were captured under identical settings (n = 13–20 images per group). Image analysis was performed with ImageJ software (NIH, Bethesda, MD, USA) (142).

MTT cytotoxicity assay

RBECs and RPCs were cultured in 96-well plates (Corning) at a density of 5×10^3 cells per well. Once confluent, the cells were subjected to OGDR treatment. Following OGDR, the medium was completely removed and cells were incubated for 3 h at 37 °C in CO_2 atmosphere with 0.5 mg/ml 3-(4,5-dimethylthiazol-2-yl)-2,5-diphenyltetrazolium bromide (MTT, Sigma M5655) dissolved in serum- and phenol red-free DMEM/F-12 medium (Gibco). After crystal formation, the medium was discarded and blue formazan crystals were solubilized in 100 µl/well dimethyl sulfoxide (DMSO, Sigma-

Aldrich/Merck). Absorbance was measured at 595 nm, with MTT reduction in normoxic wells set as 100% viability (142).

Total RNA isolation

In the triple co-culture system, RBECs were cultured on Transwell inserts (Corning, cat# 3460) for 5 days. Following OGDR treatment (6-hour OGD + 24-hour R), RPCs were removed, and RBECs were directly lysed on the inserts with Buffer RLT Plus (Qiagen, cat# 1053393), as described in previous works (159). Total RNA was extracted using the RNeasy Plus Micro Kit (Qiagen, cat# 74034), which includes an integrated gDNA eliminator spin column, following the manufacturer's instructions. RNA integrity was assessed by automated capillary electrophoresis (RNA Pico Sensitivity Assay, LabChip GX II Touch HT instrument, Perkin Elmer). Isolated RNA samples were stored at −80 °C until further analysis (142).

Library preparation and 3' RNA-sequencing (RNA-seq)

Genome-wide transcriptomic profiling was conducted by RNA-seq at GenXPro GmbH, Frankfurt, Germany. For library preparation, 1 µg of purified RNA per sample was used, resulting in the generation of 20 libraries in total. RNA was fragmented and reverse transcribed into cDNA with barcoded oligo(dT) primers carrying TrueQuant unique molecular identifiers, followed by template switching. The libraries were subsequently amplified by polymerase chain reaction (PCR) and purified using solid phase reversible immobilization beads (Agencourt AMPure XP, Beckman Coulter, cat# A63882). Sequencing was performed on the Illumina NextSeq 500 platform (142).

Bioinformatic analysis of RNA-seq data

Approximately 20 million single-end 75 bp reads were generated per library. Raw sequencing reads were adapter- and quality-trimmed using Cutadapt (version 3.4), and their quality was subsequently assessed with FastQC. The cleaned reads were aligned to the reference genome with STAR (version 2.7.10a), allowing for spliced alignments. Gene-level read quantification was carried out with STAR and RSEM (version 1.3.3), while transcript abundance was additionally estimated using RSEM. MultiQC (version 1.12) was applied to compile outputs from all tools into a unified report, thereby

facilitating the identification of global patterns and potential biases. Differential expression analysis was conducted with the DESeq2 package in R/Bioconductor, yielding log2 fold change (log2FC) values and P-values for each gene. To adjust for multiple testing, false discovery rates (FDR) were calculated using the Benjamini–Hochberg procedure. Genes with FDR < 0.05 and log2FC > 0.415 or log2FC < −0.415 were defined as differentially expressed. Functional enrichment analysis was performed with the g:GOSt tool of g:Profiler to identify overrepresented Gene Ontology (GO) terms (142).

Statistical analysis

All data are expressed as mean ± SD. For statistical comparisons between two groups, a t-test was used followed by Bonferroni correction (141). Otherwise, statistical comparisons were performed using one-way or two-way ANOVA followed by Bonferroni's post hoc test. Analyses were performed with GraphPad Prism 8.1 software (GraphPad Software Inc., La Jolla, CA). A p value < 0.05 was considered indicative of statistical significance (142).

4. Results

DMT reduces lesion volume and BBB disruption in a rat stroke model

To investigate the effects of DMT in experimental stroke, we employed a transient middle cerebral artery occlusion (tMCAO) model in rats, which has been reliably used in prior studies (140, 141). The protocol consisted of a 60-minute occlusion period, followed by 24 hours of reperfusion. Only animals exhibiting a reduction of at least 40% in cerebral blood flow were included and randomly assigned to treatment groups (Fig. 5). Reviewing the surgical logs from approximately 150 operated animals, the mean reduction in cerebral blood flow was 70%. This typically occurred in an "all-or-none" manner—an instantaneous, steep drop once the filament reached the ideal position.

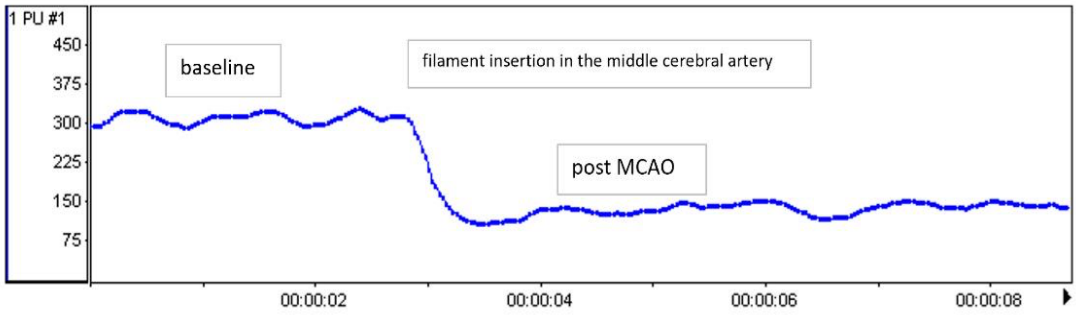

Fig. 5. Cerebral blood flow alterations during the induction of transient MCA occlusion

Transcranial laser Doppler flowmetry over the middle cerebral artery territory reveals a marked drop in cerebral blood flow immediately upon filament insertion, confirming successful arterial occlusion. Figure reproduced and legend adapted from: (142)

This model generates infarcts of sufficient size for reliable analysis while minimizing mortality associated with prolonged ischemia. It closely mirrors the pathophysiology of human ischemic stroke. However, natural variation in collateral circulation among individual animals leads to considerable variability in lesion volume, necessitating larger sample sizes to achieve statistical power compared to other models (160).

To evaluate the impact of DMT, infarct volume and brain edema were assessed on Nissl-stained histological sections (Fig. 6A). Treatment with DMT significantly reduced both infarct size and the associated swelling relative to the untreated stroke group (Fig. 6B–C).

Following these histological findings, magnetic resonance imaging (MRI) was conducted for further validation. To explore potential mechanisms underlying the observed effect, a subset of animals was co-treated with BD1063, a selective sigma-1 receptor (S1R) antagonist, alongside DMT (Fig. 6D). MRI scans acquired 24 hours after MCAO confirmed that DMT monotherapy significantly decreased lesion volume compared to controls (135.1 ± 19.0 mm^3 vs. 204.8 ± 24.5 mm^3, $p = 0.0373$; n = 10 per group). In contrast, animals receiving the combined DMT and BD1063 treatment exhibited significantly larger infarct volumes compared to the DMT-only group (208.1 ± 22.6 mm^3 vs. 135.1 ± 19.0 mm^3, $p = 0.0238$; Fig. 6E). Notably, no significant difference was observed between the DMT+BD1063 group and the control animals (208.1 ± 22.6 mm^3 vs. 204.8 ± 24.5 mm^3, $p = 0.9222$; Fig. 6E).

Using this protocol, we generated a large striatal–cortical lesion with an MRI-measured volume of 150–200 mm^3, corresponding to ~15–20% of the rat hemisphere. Proportionally, this is comparable to a relatively large 70–100 mL human infarct, or even a larger, “malignant” lesion of approximately 150 mL. Regarding the time window, a direct translation of this model to a human equivalent is more difficult due to the strong dependence on collateral circulation. However, in humans with poor collaterals, our model roughly corresponds to an M1-level occlusion lasting about 60–120 minutes.

We found no difference in mortality between the DMT-treated and untreated groups during either the 24-hour or the 30-day follow-up, and we did not observe any non-technical deaths.

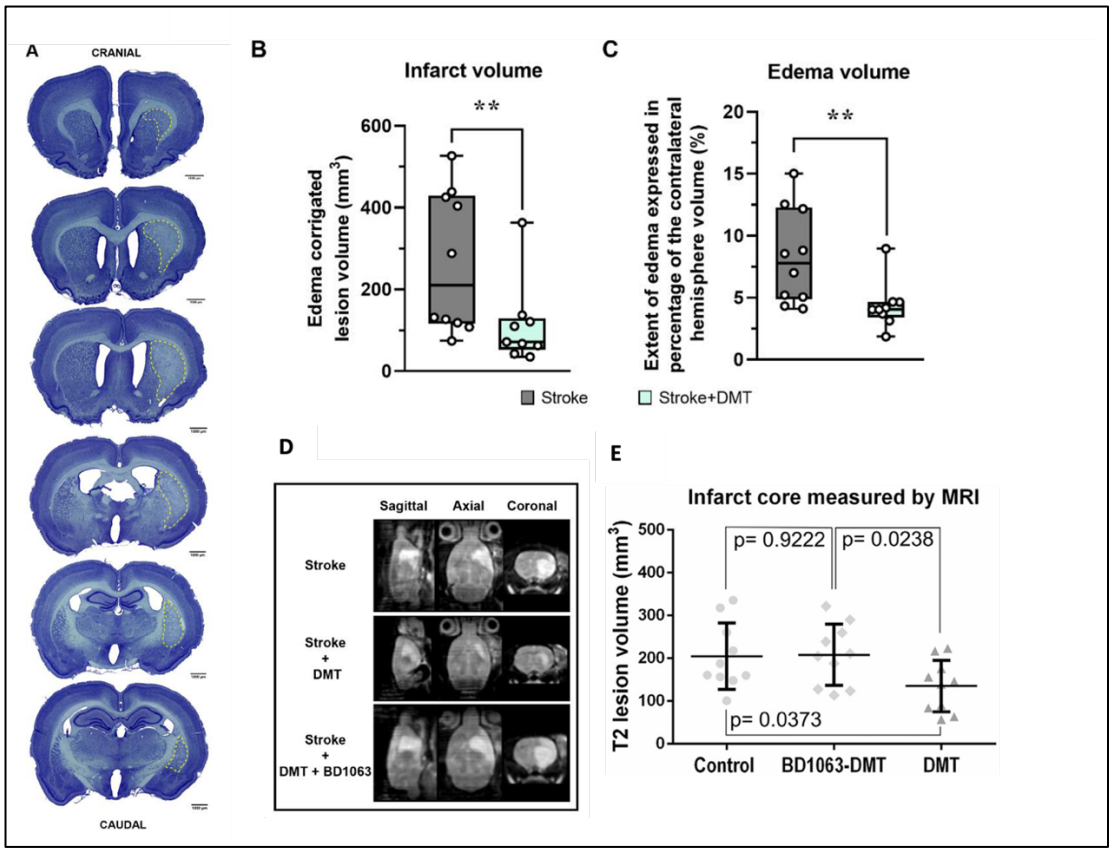

Fig. 6. Effect of DMT on infarct size and the associated edema

A: Representative cresyl violet–stained coronal brain sections from a DMT-treated rat, shown in cranial-to-caudal sequence. The infarcted regions are marked with yellow dotted lines. **B, C**: Quantitative comparison of infarct volume and brain edema between the stroke group (n = 10) and the DMT-treated stroke group (n = 9) demonstrates that DMT significantly reduced infarct size (**P = 0.0327) and the extent of associated edema (**P = 0.0135); data are presented as mean ± SD, analyzed with unpaired t-test. **D**: Representative MRI scans in sagittal, axial, and coronal planes from rats in the stroke, DMT-treated, and DMT+BD1063-treated groups (n = 10 rats/group). **E:** Quantitative analysis of individual T2-weighted lesion volumes at 24 hours post-MCAO revealed that DMT administration significantly reduced infarct core size. Animals receiving DMT monotherapy (grey triangles) exhibited markedly smaller lesion volumes compared to vehicle-treated controls (grey dots). In contrast, rats treated with the combined DMT and BD1063 regimen (grey diamonds) displayed lesion sizes comparable to those observed in the control group. Data are presented as mean ± standard deviation. Figure reproduced and legend adapted from: (142)

In line with the lesion volume data presented above, DMT appears to confer neuroprotection in the context of ischemic stroke. To examine whether this effect is associated with preserved blood-brain barrier (BBB) integrity, we assessed vascular permeability using FITC-albumin. The dye was administered to selected groups 23 hours after reperfusion, followed by one hour of circulation before sample collection (Fig. 7A). FITC-albumin fluorescence in the brain parenchyma was quantified on histological sections (Fig. 7B, Fig. 7E). A significant reduction in FITC-albumin extravasation was observed in DMT-treated animals compared to stroke controls ($P = 0.0093$). This effect persisted in animals receiving combined treatment with DMT and the sigma-1 receptor antagonist BD1063 (Fig. 7C).

To further validate these findings, FITC-albumin levels in the cerebrospinal fluid (CSF) were measured using fluorescence spectroscopy. DMT-treated animals exhibited significantly lower FITC-albumin concentrations in the CSF compared to the stroke group ($P = 0.0454$). Although a slight trend toward increased leakage was observed in the DMT+BD1063 group, the difference did not reach statistical significance ($P = 0.3821$; Fig. 7D).

Together, these results suggest that DMT supports BBB integrity following ischemic injury. Although BD1063 may partly influence this effect, its failure to completely block DMT's effect suggests that sigma-1 receptor signaling is involved, but not solely responsible, for the protective mechanism.

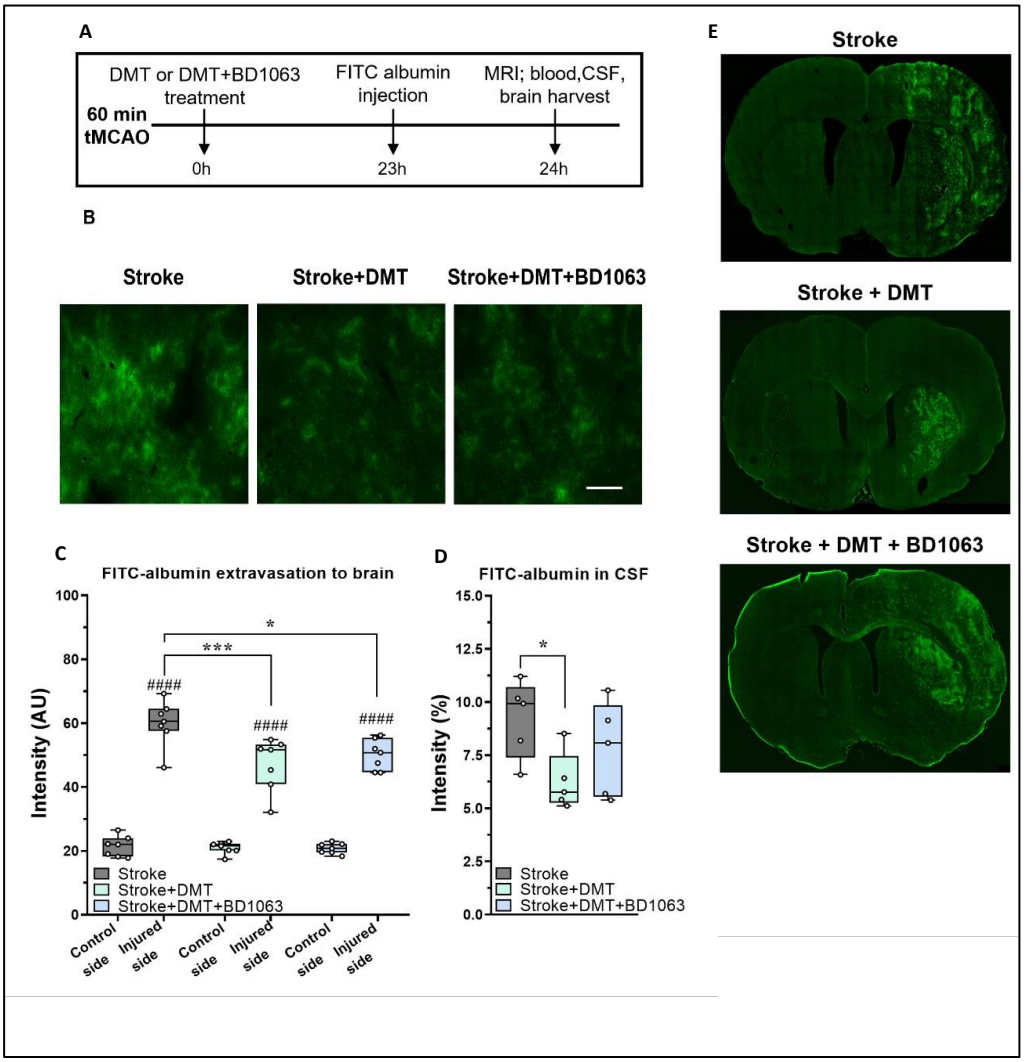
A
DMT or DMT+BD1063 treatment
FITC albumin injection
MRI; blood,CSF, brain harvest
60 min tMCAO
0h
23h
24h
B
Stroke
Stroke+DMT
Stroke+DMT+BD1063
C
FITC-albumin extravasation to brain
Intensity (AU)
Stroke
Stroke+DMT
Stroke+DMT+BD1063
Control side
Injured side
D
FITC-albumin in CSF
Intensity (%)
E
Stroke
Stroke + DMT
Stroke + DMT + BD1063

Fig. 7. Albumin extravasation to brain and cerebrospinal fluid in the rat transient focal brain ischemia model

A: Schematic representation of treatment protocol and experimental timeline. **B:** Representative low-magnification images (scale bar: 200 μm) from the stroke, DMT-treated stroke, and DMT+BD1063 co-treated groups demonstrate green FITC-albumin fluorescence as an indicator of blood-brain barrier (BBB) permeability. The observed extravasation reflects the extent of BBB disruption. **C:** Quantitative assessment of FITC-albumin extravasation in both hemispheres across stroke, DMT, and DMT+BD1063 treatment groups (n = 7 rats/group). A significant reduction in FITC signal intensity was observed in the DMT group compared to stroke (***P = 0.0093). The DMT+BD1063 co-treatment group also showed reduced intensity versus stroke (*P = 0.011), while no significant difference was found compared to DMT alone (P = 0.4254); values shown as mean ± SD, analyzed with two-way ANOVA followed by Bonferroni's post hoc test. The contralateral, non-injured hemisphere showed no treatment-related changes. **D**: Quantitative analysis of FITC-albumin penetration into the cerebrospinal fluid (CSF) using fluorescence spectroscopy. CSF samples were collected from stroke (n = 5), DMT-treated stroke (n = 5), and DMT+BD1063-treated stroke (n = 5) groups. A significant reduction in FITC intensity was observed in the DMT-treated stroke group compared to vehicle-treated stroke animals (p = 0.0454), while the DMT+BD1063 co-treated group showed no significant difference from the stroke group (p = 0.3821). (H) FITC-albumin levels in cerebrospinal fluid were quantified using fluorescence spectroscopy (n = 5 rats/group). DMT treatment significantly reduced FITC intensity compared to stroke (*P = 0.0454), whereas co-treatment with BD1063 did not yield a significant difference from stroke alone (P = 0.3821). **E:** Fluorescent images illustrating FITC-albumin leakage into the brain parenchyma as a marker of blood-brain barrier disruption. Figure reproduced and legend adapted from: (142)

DMT attenuates oxygen-glucose deprivation–induced barrier disruption in a rat co-culture model

To examine the cell type–specific responses to DMT, primary rat brain endothelial cells, pericytes, and astroglia were studied both in monocultures and in co-culture

systems, forming a specific model of the blood–brain barrier. The effects of DMT under normoxic conditions were initially tested on brain endothelial monolayers across a concentration range of 1–300 µM (Fig. 8A–B). No concentration-dependent effect on endothelial impedance was observed, except for a modest 5% decrease at the highest concentration (300 µM) relative to untreated controls.

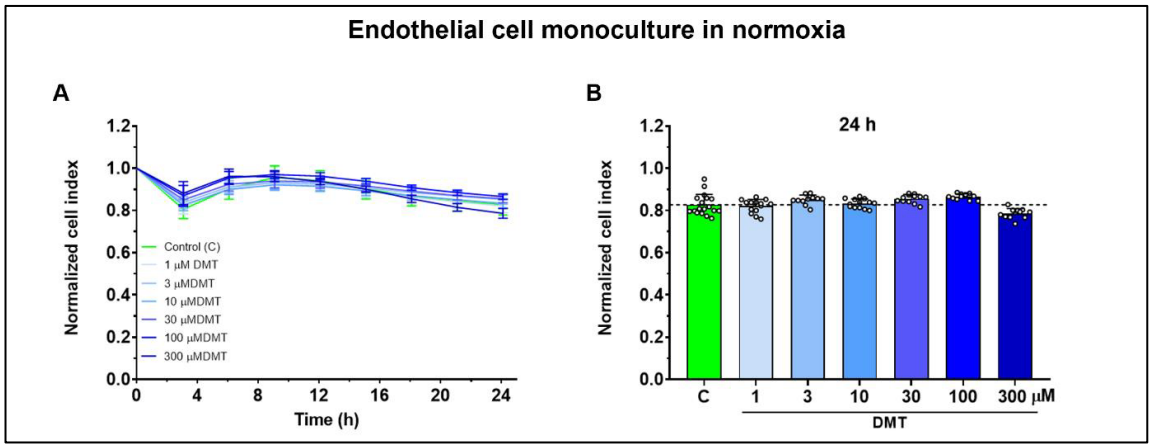

Fig. 8. Effect of DMT on BBB cell types under normoxic conditions

A–B: Impedance kinetics of rat primary brain endothelial cells exposed to 1–300 µM DMT under normoxic conditions. Data are presented as mean ± SD, n = 11–18. Figure reproduced and legend adapted from: (142)

The oxygen-glucose deprivation–reoxygenation (OGDR) model was established using monocultures of each blood-brain barrier cell type, and real-time impedance measurements were employed to monitor the kinetics of cellular responses (Fig. 9A). Following a 6-hour OGD insult, cultures were allowed to recover for 24 hours under reoxygenated conditions in the presence of either DMT alone or in combination with the S1R antagonist BD1063. The cellular response to OGDR varied distinctly among the three cell types (Fig. 9B). Endothelial cells exhibited a sharp drop in impedance to 40% during OGD, but recovered to nearly 90% of baseline after reoxygenation. Glial cells also showed sensitivity, with impedance decreasing to 63%. Although an initial recovery peak was observed, glial impedance plateaued at 71% by the end of the 30-hour observation period. Pericytes were the most vulnerable, showing a marked decline in impedance to 14% during OGD and a partial recovery to 70% post-reoxygenation. Quantitative analysis of the impedance curves (area under the curve, expressed as cell index) further confirmed

that pericytes were most affected by OGDR, followed by endothelial cells and astrocytes, the latter exhibiting the best recovery profile.

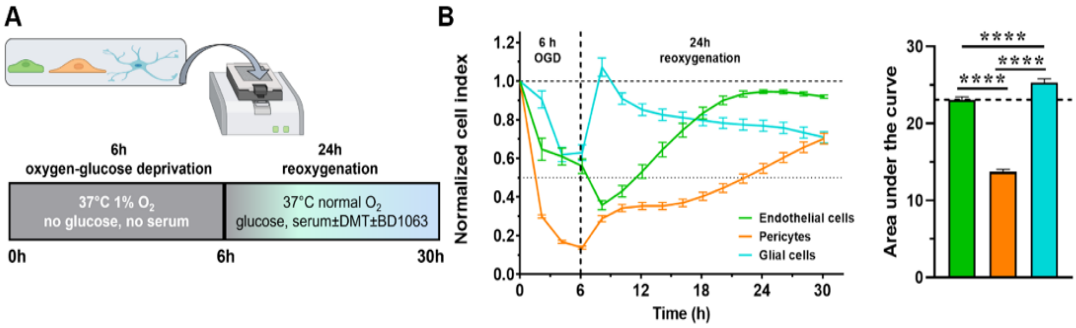

Fig. 9. Effect of OGDR on a primary rat blood-brain barrier (BBB) co-culture model

A: Schematic representation of the impedance-based experimental setup. Rat primary brain endothelial cells (green), pericytes (orange), and glial cells (blue) were subjected to 6 hours of oxygen-glucose deprivation (OGD), followed by 24 hours of reoxygenation in the presence of either DMT or DMT+BD1063. **B:** Real-time impedance recordings for each cell type under OGDR conditions, shown as kinetic curves and quantified by area under the curve (AUC) of cell index from 0 to 30 hours. Data are presented as mean ± SD; one-way ANOVA with Bonferroni's post hoc test; ****P < 0.0001; n = 5–13. Figure reproduced and legend adapted from: (142)

The impact of DMT during the reoxygenation phase was also assessed; however, no significant changes were detected in the impedance of any of the cell monolayers after 24 hours of recovery (Fig. 10A–F).

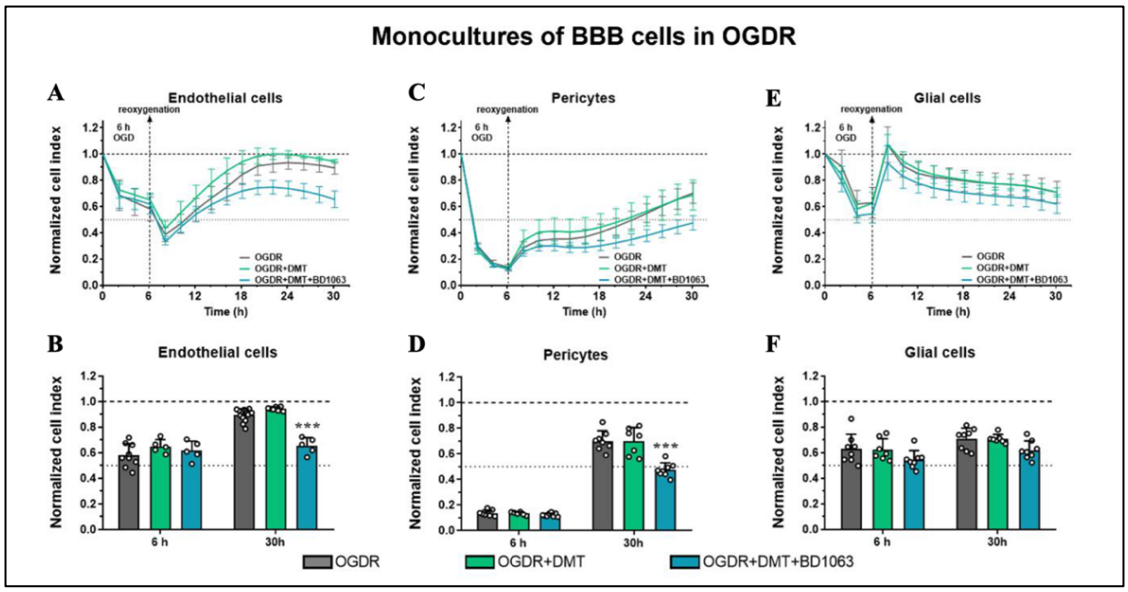

Fig. 10. Effect of DMT on BBB cell types under OGDR

A-F: Impedance profiles of rat primary brain endothelial cells, pericytes, and glial cells during a 6-hour period of oxygen-glucose deprivation (OGD) followed by reoxygenation (OGDR). Cultures were treated with 200 µM DMT or 200 µM DMT combined with 2 µM BD1063. Data are expressed as mean ± SD. Statistical analysis was performed using ANOVA with Bonferroni's post hoc test. ****P < 0.0001 compared to the OGDR group, n = 5–13. Figure reproduced and legend adapted from: (142)

OGDR exposure led to a reduction in cellular metabolic activity in both brain endothelial cells and pericytes, as determined by MTT assay (Fig. 11). This impairment was reversed by DMT treatment at concentrations of 100 and 200 µM (Fig. 11A). Based on these results, the 200 µM dose was selected for subsequent experiments. In brain endothelial cells, DMT effectively prevented the OGDR-induced decline in metabolic activity (Fig. 11B), whereas no such protective effect was observed in pericytes (Fig. 11C).

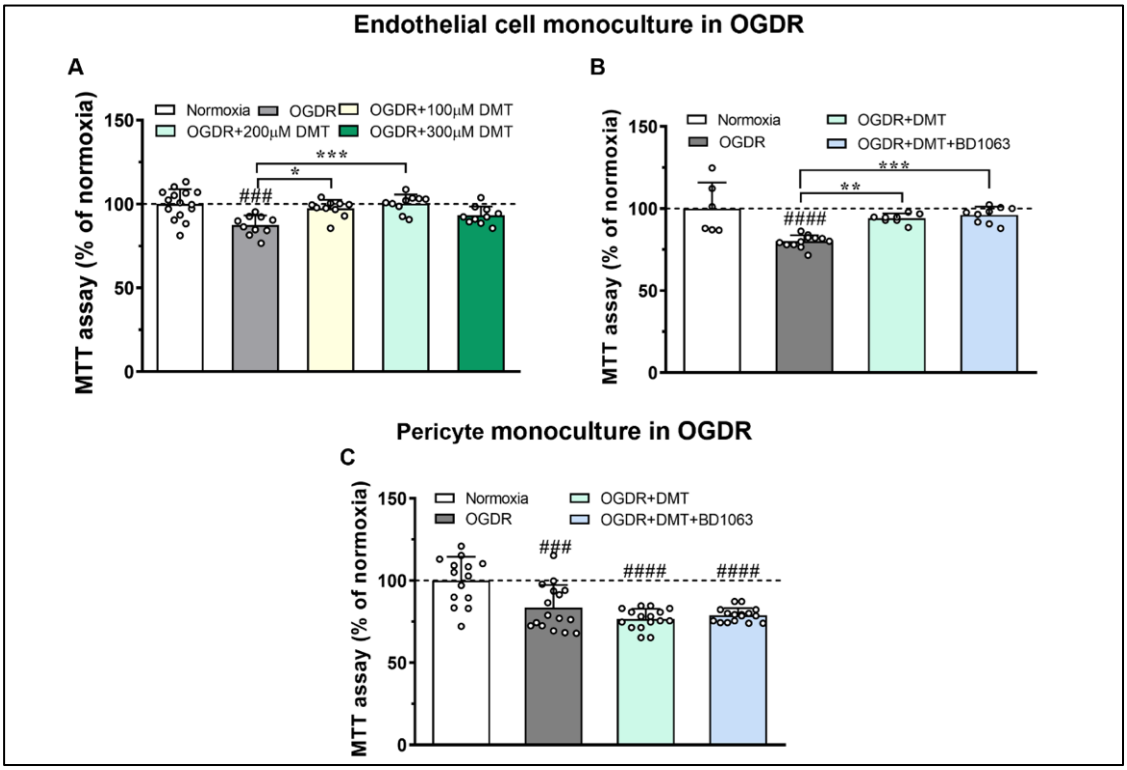

Fig. 11. Effect of DMT on metabolic activity assessed by MTT assay in primary rat brain endothelial cells and pericytes during OGDR

A: Evaluation of cell viability in rat brain endothelial cells exposed to oxygen-glucose deprivation and reoxygenation (OGDR) and treated with increasing concentrations of DMT (100, 200, and 300 μM). Results are expressed as percentages relative to normoxic controls. Data represent mean ± SD; statistical comparisons were performed using one-way ANOVA followed by Bonferroni's multiple comparisons test; ###p = 0.0002 versus normoxia; *p = 0.0121, ***p = 0.0005 versus OGDR; n = 10–15. **B:** Effect of 200 μM DMT, with or without 2 μM BD1063, on endothelial cell viability following OGDR. Values are expressed relative to normoxia (mean ± SD); ###p < 0.0001 versus normoxia; **p = 0.0012, ***p = 0.0001 versus OGDR; n = 6–12. **C:** Viability of brain pericytes following OGDR and treatment with 200 μM DMT alone or combined with 2 μM BD1063. Results are shown as a percentage of normoxic controls (mean ± SD); ###p = 0.0004, ####p < 0.0001 versus normoxia; n = 14–16. Figure reproduced and legend adapted from: (142)

To assess barrier integrity in the in vitro BBB model, a triple co-culture system was utilized (Fig. 12A). Exposure to OGDR resulted in a significant reduction in

transendothelial electrical resistance (TEER) (Fig. 12B), accompanied by a 2.4-fold increase in paracellular permeability to fluorescein (Fig. 12C) and a 2.5-fold increase in transcellular permeability to albumin (Fig. 12D), indicating substantial barrier disruption. DMT administration significantly attenuated the increase in albumin permeability, suggesting a protective effect on the transcellular route. However, DMT had no detectable influence on the OGDR-induced changes in paracellular integrity, as reflected by unchanged TEER and fluorescein permeability values (Fig. 12B–D). Notably, co-treatment with the sigma-1 receptor antagonist BD1063 did not reverse the stabilizing effect of DMT (Fig. 12D).

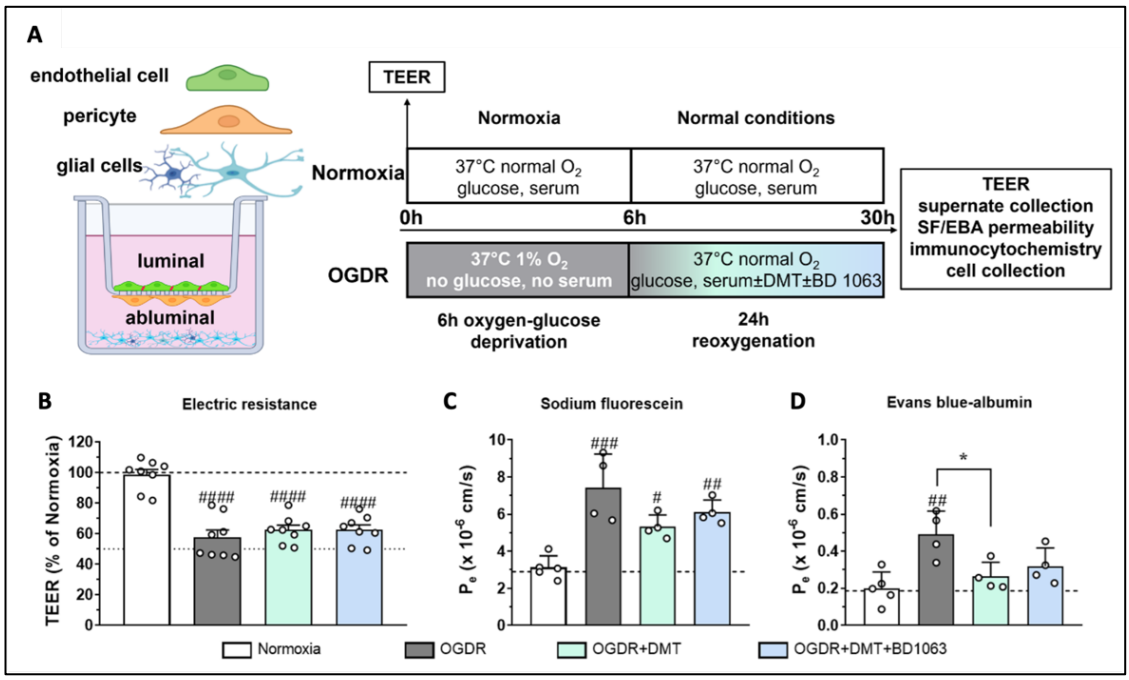

Fig. 12. Effect of OGDR and DMT on a primary rat blood-brain barrier (BBB) co-culture model

A: Overview of the experimental design for assessing barrier integrity using the BBB co-culture model under normoxic and OGDR conditions. **B:** Transendothelial electrical resistance (TEER) measurements taken after 24 hours of reoxygenation. Values are expressed as mean ± SEM; n = 8. **C:** Permeability to sodium fluorescein and **D** Evans blue–albumin (Pe: endothelial permeability coefficient) following 24-hour reoxygenation. Results are given as mean ± SD; n = 4. One-way ANOVA with Bonferroni's post hoc test; #P < 0.05, ##P < 0.01, ###P < 0.0003 versus normoxia. Figure reproduced and legend adapted from: (142)

DMT preserves BBB integrity via claudin-5 stabilization and mitigates cytotoxic edema by downregulating AQP4 activation

Immunofluorescence analysis revealed a marked reduction in the tight junction protein claudin-5 (CLDN5) on the ischemic hemisphere compared to the contralateral side following focal cerebral ischemia ($P < 0.0001$; Fig. 13A), indicating blood-brain barrier disruption. This loss of CLDN5 signal was prevented by DMT administration, as no significant difference in fluorescence intensity was observed between hemispheres in the DMT-treated group. However, the protective effect of DMT was abolished by co-treatment with the sigma-1 receptor antagonist BD1063, which resulted in a significant reduction in CLDN5 intensity on the injured side ($P < 0.0001$), resembling that of vehicle-treated animals (Fig. 13B).

Similar patterns were observed in vitro using cultured brain endothelial cells exposed to OGDR. CLDN5 staining was decreased after OGDR, while DMT treatment preserved its intensity. In contrast, the combined DMT+BD1063 condition showed a reduction in CLDN5 staining comparable to OGDR alone (Fig. 13C–D).

Circulating CLDN5 protein levels were also quantified to assess systemic evidence of BBB breakdown. Serum CLDN5 concentrations were significantly elevated following stroke (Fig. 13H), consistent with junctional degradation. This increase was effectively inhibited by DMT treatment ($P < 0.0001$), and BD1063 co-administration did not interfere with the protective effect. Serum matrix metalloproteinase-9 (MMP9), known

to degrade junctional proteins, was significantly elevated in the stroke group. DMT significantly reduced serum MMP9 levels ($P = 0.0076$), reaching values similar to those in vehicle-treated controls. Notably, this effect was not altered by the addition of BD1063 (Fig. 13I).

Given the role of AQP4 in astrocyte-mediated water transport and cytotoxic edema, we next examined its expression by immunohistochemistry (Fig. 13E). A significant increase in AQP4 fluorescence intensity was detected in the peri-infarct region compared to the contralateral hemisphere ($P = 0.0033$). DMT treatment prevented this elevation, as no significant difference was found between hemispheres. However, in the DMT+BD1063 group, AQP4 expression increased on the injured side ($P = 0.0011$), mirroring the vehicle group (Fig. 13F). These findings suggest that the effect of DMT on AQP4 expression is mediated through sigma-1 receptor signaling.

In our analysis of astrocytes in the perivascular region (Fig. 13E), the immunoreactivity of glial fibrillary acidic protein (GFAP), a cytoskeletal marker of astrocytes, did not show significant differences between hemispheres in any treatment group (Fig. 13G), in contrast to the pattern observed for AQP4. In glial cell cultures, OGDR increased GFAP staining, and this effect was significantly decreased by DMT (Fig. 14A–B).

Finally, serum GFAP levels were measured to evaluate astrocytic activation and BBB dysfunction, as serum GFAP is known from human data to correlate with infarct size, neurological severity, and long-term outcome in acute stroke patients (91, 92, 161, 162) (Fig. 13J). Stroke induced a fourfold elevation in circulating GFAP, which was significantly suppressed by DMT treatment ($P < 0.0001$). However, co-administration of BD1063 reversed this effect ($P = 0.0179$), and GFAP levels in the DMT+BD1063 group were not significantly different from those in the vehicle-treated stroke group ($P = 0.0586$). These results support the notion that DMT mitigates ischemia-induced astrocytic and BBB responses, at least in part, through sigma-1 receptor–dependent mechanisms.

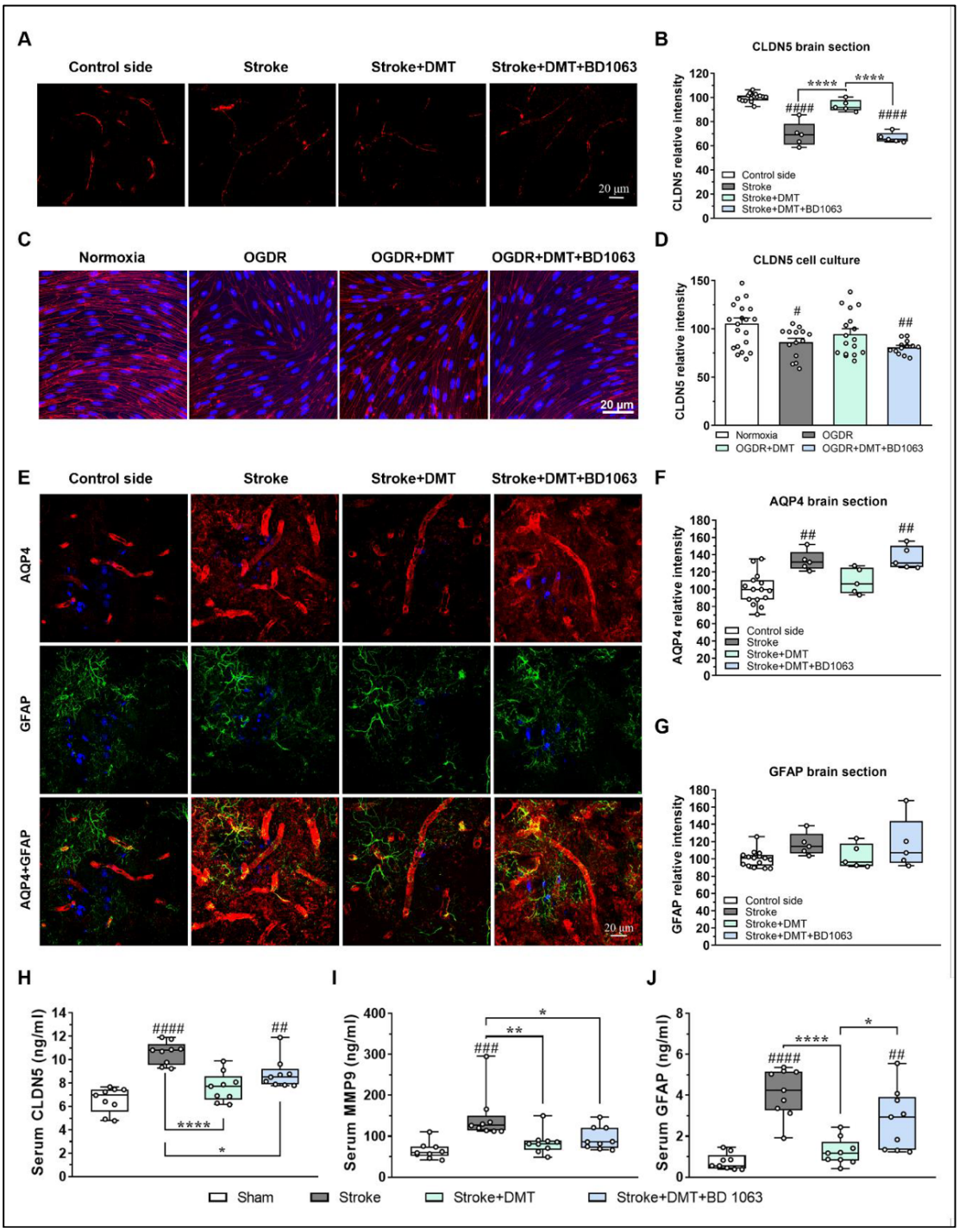
A
Control side
Stroke
Stroke+DMT
Stroke+DMT+BD1063
20 μm
B
CLDN5 brain section
CLDN5 relative intensity
Control side
Stroke
Stroke+DMT
Stroke+DMT+BD1063
C
Normoxia
OGDR
OGDR+DMT
OGDR+DMT+BD1063
20 μm
D
CLDN5 cell culture
CLDN5 relative intensity
Normoxia
OGDR
OGDR+DMT
OGDR+DMT+BD1063
E
Control side
Stroke
Stroke+DMT
Stroke+DMT+BD1063
AQP4
GFAP
AQP4+GFAP
20 μm
F
AQP4 brain section
AQP4 relative intensity
G
GFAP brain section
GFAP relative intensity
H
Serum CLDN5 (ng/ml)
I
Serum MMP9 (ng/ml)
J
Serum GFAP (ng/ml)
Sham
Stroke
Stroke+DMT
Stroke+DMT+BD 1063

Fig. 13. DMT preserves blood-brain barrier integrity

A: Representative images show CLDN5 immunofluorescent staining in brain sections. **B:** Quantification of CLDN5 signal intensity reveals a significant reduction on the injured hemisphere after stroke, which is prevented by DMT treatment. Data are presented as mean ± SD. One-way ANOVA with Bonferroni's post hoc test: #### $P < 0.0001$ compared to the contralateral (control) hemisphere, **** $P < 0.0001$ compared to the stroke group; n = 5–15. **C:** CLDN5 immunofluorescent staining in cultured brain endothelial cells. **D:** Quantitative analysis of CLDN5 fluorescence intensity confirms reduced expression after OGDR, which is mitigated by DMT. Mean ± SD, one-way ANOVA with Bonferroni's post hoc test: # $P = 0.0399$; ## $P = 0.0058$ compared to the normoxia group; n = 13–17. **E:** Double immunostaining for AQP4 and GFAP in brain sections. **F:** Quantification of AQP4 signal intensity reveals significantly elevated levels on the injured side following stroke, which is prevented by DMT treatment. Mean ± SD, one-way ANOVA with Bonferroni's post hoc test: ## $P < 0.005$ compared to the contralateral hemisphere; n = 5–15. **G:** Quantification of GFAP fluorescence intensity shows no significant inter-group differences. **H–J:** Serum ELISA measurements of CLDN5, MMP9, and GFAP concentrations. Data are expressed as mean ± SD; n = 9 rats/group. One-way ANOVA with Bonferroni's post hoc test: ## $P < 0.01$; ### $P < 0.001$; #### $P < 0.0001$ vs. sham group; * $P < 0.05$; ** $P = 0.0076$; **** $P < 0.0001$ vs. stroke group. Figure reproduced and legend adapted from: (142)

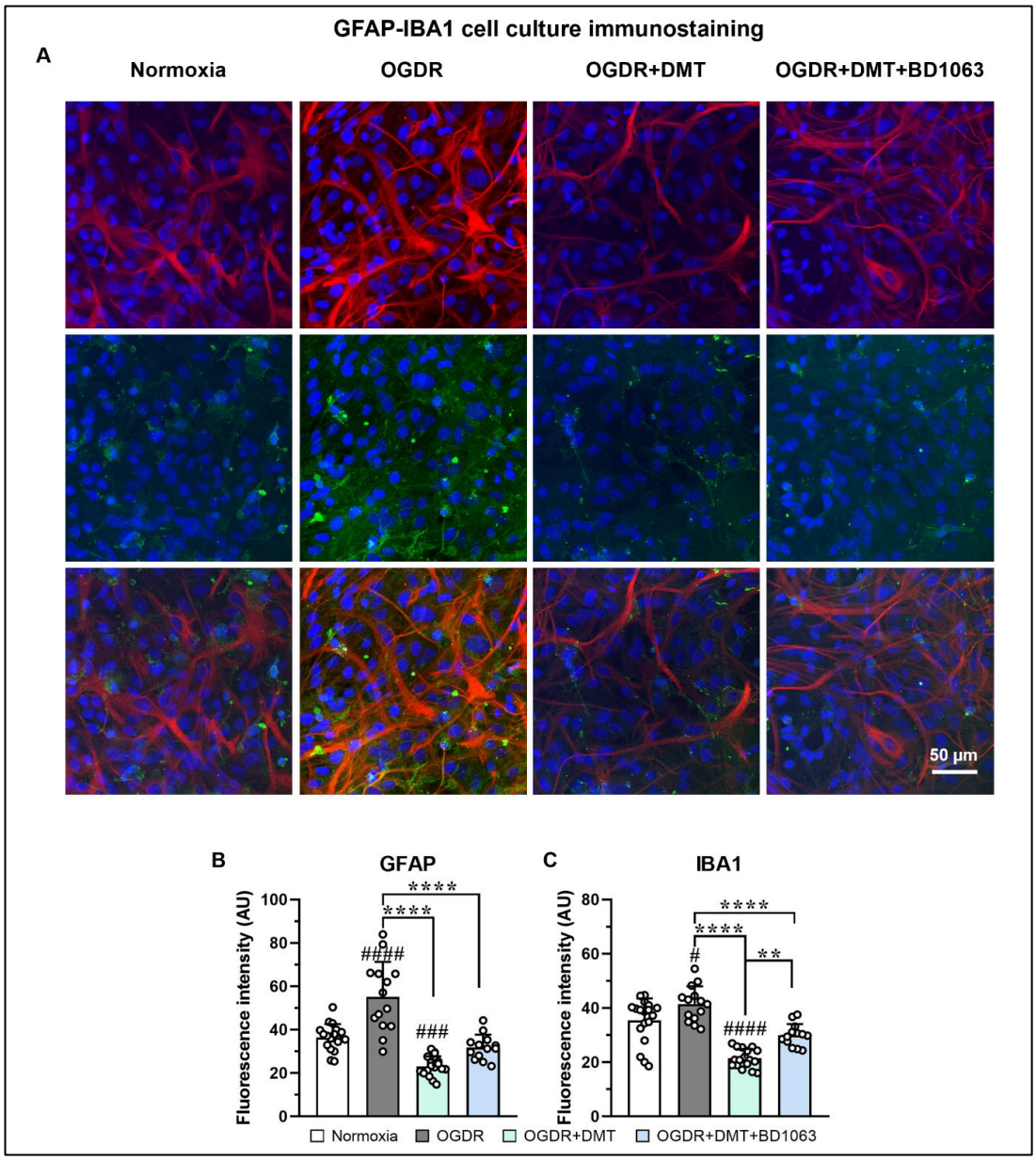

Fig. 14. Immunostaining of cultured glial cells following OGDR

A: Representative immunofluorescent images of GFAP-positive astrocytes and IBA1-labeled microglia in glial cell cultures after oxygen-glucose deprivation and reoxygenation (OGDR). Scale bar: 50 µm. **B:** Quantification of GFAP fluorescence intensity. **C:** Quantification of IBA1 fluorescence intensity. Data are presented as mean ± SD; one-way ANOVA with Bonferroni's post hoc test: ### $P < 0.001$, #### $P < 0.0001$ compared to the normoxia group; ** $P < 0.01$ and **** $P < 0.0001$ compared to the stroke + DMT group; n = 14–18. Figure reproduced and legend adapted from: (142)

DMT modulates gene expression and attenuates cytokine release in brain endothelial cells following OGDR

To explore transcriptomic alterations induced by DMT in brain endothelial cells under ischemic conditions, we performed Massive Analysis of cDNA Ends (MACE-seq) on primary brain endothelial cells derived from triple co-cultures. Principal component analysis revealed clear clustering between OGDR-exposed samples and the normoxic controls along principal component 2, underscoring substantial transcriptional reprogramming following OGDR exposure (Fig. 15A). Differential expression analysis identified 942 downregulated and 1071 upregulated genes in the OGDR group relative to normoxia (Fig. 15B). These transcriptional changes were enriched for pathways related to cellular stress responses, extracellular matrix reorganization, and proliferative signaling (Fig. 15C–D).

Surprisingly, DMT exerted only a modest impact on the overall transcriptomic profile: comparison of OGDR vs. OGDR+DMT conditions revealed significant alterations in just 19 transcripts. Among these, notable findings included the downregulation of inflammation-associated genes (Gbp2, Cuedc2) and the upregulation of transcripts involved in anti-inflammatory signaling (Lrrc14, Gdf15) and glucose metabolism (Flcn, Uap1l1, Insig1) (Fig. 15E). Importantly, the addition of the sigma-1 receptor antagonist BD1063 did not reverse these gene expression changes (OGDR+DMT+BD1063 vs. OGDR+DMT; Fig. 15F), suggesting sigma-1 receptor–independent transcriptional modulation.

To further investigate the inflammatory milieu, cytokine concentrations were measured in both the luminal and abluminal compartments of the co-culture model, simulating the blood and brain sides of the BBB, respectively (Fig. 15G–N). In normoxic conditions, the four analyzed cytokines were undetectable, except for IL-6, which was present at very low levels in the luminal chamber (Fig. 15K). OGDR significantly increased the secretion of pro-inflammatory cytokines—TNFα, IL-1β, and IL-6 (Fig. 15G–L)—as well as the anti-inflammatory cytokine IL-10 (Fig. 15M–N) in both compartments. Higher cytokine concentrations were found on the abluminal side, reflecting contributions from astrocytes and microglia in addition to endothelial cells.

DMT administration effectively suppressed the release of TNFα, IL-1β, and IL-6 across both compartments, without significantly altering IL-10 levels (Fig. 15G–N). Co-treatment with BD1063 antagonized DMT's effect on TNFα, IL-1β, and IL-6 (Fig. 15G–L), implicating the sigma-1 receptor in mediating this anti-inflammatory action.

Taken together, these results indicate that DMT reduces inflammation in the in vitro BBB model. However, given the limited transcriptional response observed in endothelial cells by MACE-seq, it is likely that this cell type is not the primary target of DMT. To further elucidate the systemic mechanisms underlying DMT's neurovascular protection, we next examined inflammatory gene expression in the brain and in peripheral blood mononuclear cells (PBMCs), assessed plasma cytokine and chemokine profiles, and analyzed morphological changes in brain microglia.

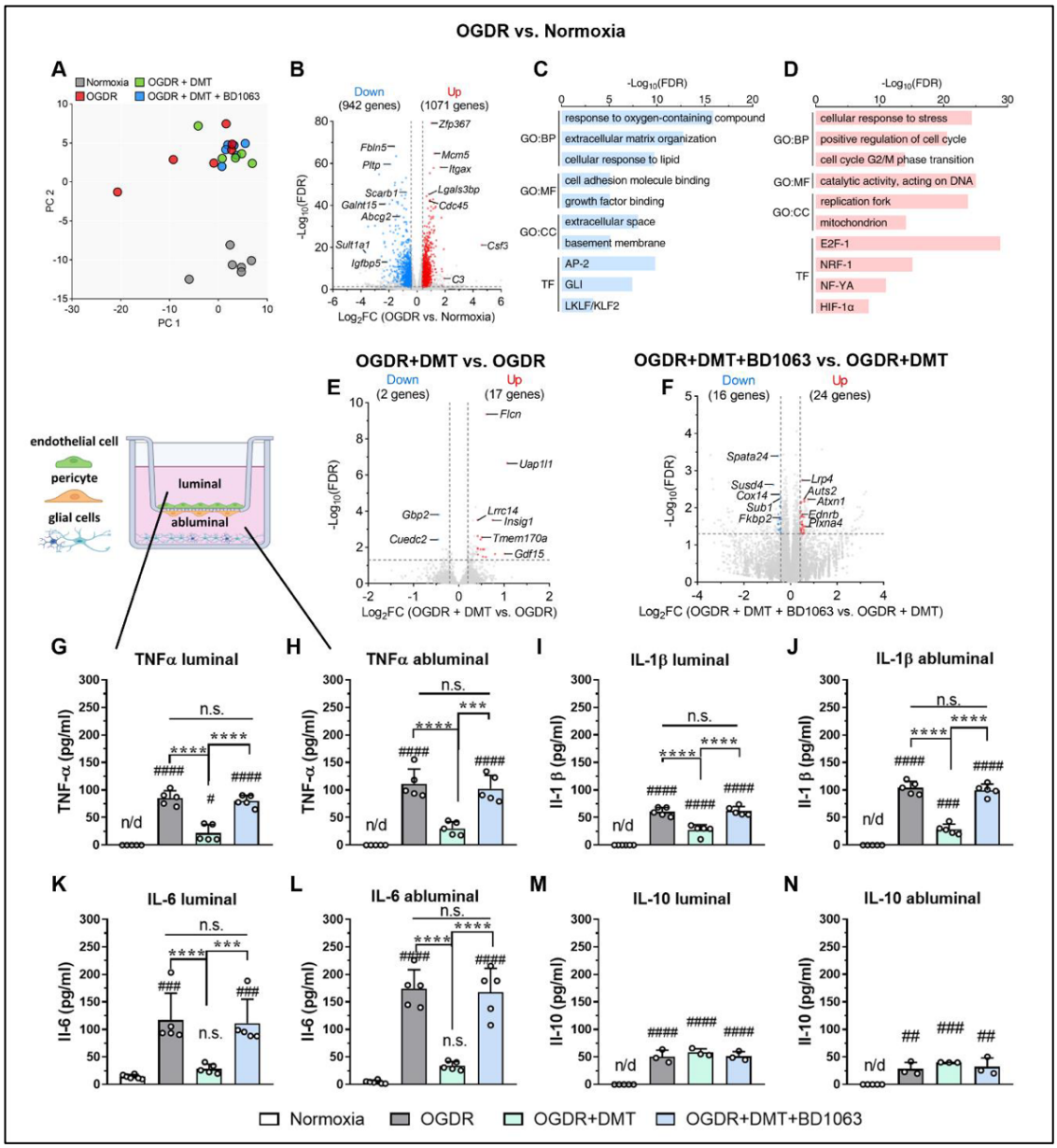
OGDR vs. Normoxia
A
Normoxia
OGDR
OGDR + DMT
OGDR + DMT + BD1063
PC 2
PC 1
B
Down
(942 genes)
Up
(1071 genes)
Zfp367
Fbln5
Pltp
Mcm5
Itgax
Scarb1
Galnt15
Lgals3bp
Cdc45
Abcg2
Sult1a1
Igfbp5
Csf3
C3
-Log10(FDR)
Log2FC (OGDR vs. Normoxia)
C
-Log10(FDR)
GO:BP
response to oxygen-containing compound
extracellular matrix organization
cellular response to lipid
GO:MF
cell adhesion molecule binding
growth factor binding
GO:CC
extracellular space
basement membrane
TF
AP-2
GLI
LKLF/KLF2
D
-Log10(FDR)
GO:BP
cellular response to stress
positive regulation of cell cycle
GO:MF
cell cycle G2/M phase transition
catalytic activity, acting on DNA
GO:CC
replication fork
mitochondrion
TF
E2F-1
NRF-1
NF-YA
HIF-1α
endothelial cell
pericyte
glial cells
luminal
abluminal
OGDR+DMT vs. OGDR
E
Down
(2 genes)
Up
(17 genes)
Flcn
Uap1l1
Gbp2
Lrrc14
Insig1
Cuedc2
Tmem170a
Gdf15
-Log10(FDR)
Log2FC (OGDR + DMT vs. OGDR)
OGDR+DMT+BD1063 vs. OGDR+DMT
F
Down
(16 genes)
Up
(24 genes)
Spata24
Susd4
Cox14
Sub1
Fkbp2
Lrp4
Auts2
Atxn1
Ednrb
Plxna4
-Log10(FDR)
Log2FC (OGDR + DMT + BD1063 vs. OGDR + DMT)
G
TNFα luminal
TNF-α (pg/ml)
H
TNFα abluminal
TNF-α (pg/ml)
I
IL-1β luminal
Il-1 β (pg/ml)
J
IL-1β abluminal
Il-1 β (pg/ml)
K
IL-6 luminal
Il-6 (pg/ml)
L
IL-6 abluminal
Il-6 (pg/ml)
M
IL-10 luminal
Il-10 (pg/ml)
N
IL-10 abluminal
Il-10 (pg/ml)
n/d
n.s.
Normoxia
OGDR
OGDR+DMT
OGDR+DMT+BD1063

Fig. 15. The anti-inflammatory effects of DMT in cultured brain endothelial cells following OGDR

A: Principal component analysis (PCA) reveals distinct transcriptomic profiles between normoxia and OGDR-treated groups. **B:** Volcano plot representing differential gene expression in OGDR versus normoxia. Log2FC: log2(fold change), FDR: false discovery rate. **C, D:** Gene ontology (GO) and transcription factor binding site (TF) enrichment analysis of downregulated **(C)** and upregulated **(D)** pathways in the OGDR group compared to normoxia. **E:** Volcano plot illustrating transcriptomic changes induced by DMT in OGDR-treated brain endothelial cells. **F:** Volcano plot showing the effect of BD1063 co-treatment on DMT-modulated gene expression. **G:** Schematic diagram of the BBB co-culture model highlighting the luminal and abluminal compartments. **G–N:** Quantification of TNFα, IL-1β, IL-6, and IL-10 cytokine levels in supernatants from the luminal and abluminal compartments of the rat triple co-culture BBB model. n/d: not detected. n = 3–6 per group; data are presented as mean ± SD; one-way ANOVA with Bonferroni's post hoc test: # $P < 0.05$, ## $P < 0.01$, ### $P < 0.001$, #### $P < 0.0001$ compared to the normoxia group; *** $P < 0.001$, **** $P < 0.0001$ for comparisons among OGDR groups. Figure reproduced and legend adapted from: (142)

DMT modulates cerebral expression of inflammation-related cytokine genes following focal ischemia

To evaluate the potential anti-inflammatory effects of DMT in the post-ischemic brain, we assessed cortical mRNA expression levels of key inflammatory mediators 25 hours after MCAO in two experimental groups (n = 8 per group). The selected targets included three pro-inflammatory cytokines—interleukin-1β (IL-1β), interleukin-6 (IL-6), and tumor necrosis factor-α (TNF-α)—as well as the anti-inflammatory cytokine interleukin-10 (IL-10), measured bilaterally in both the peri-infarct and contralateral cortices.

IL-1β mRNA expression was markedly downregulated in DMT-treated animals in both the peri-infarct region (0.05 ± 0.04 vs. 0.29 ± 0.02, $p = 0.0061$) and the contralateral hemisphere (0.06 ± 0.05 vs. 0.38 ± 0.22, $p = 0.0015$) (Fig. 16A). A similar bilateral

suppression was observed for IL-6, with significantly reduced transcript levels in both hemispheres (peri-infarct: 0.30 ± 0.29 vs. 0.85 ± 0.38, p = 0.0054; contralateral: 0.36 ± 0.64 vs. 1.85 ± 0.51, p = 0.0001) (Fig. 16B).

TNF-α expression was significantly decreased in the contralateral cortex of DMT-treated animals (0.490 ± 0.08 vs. 1.45 ± 0.21, p = .0007), whereas in the peri-infarct cortex only a nonsignificant trend toward reduction was observed (0.58 ± 0.15 vs. 0.80 ± 0.14, p = .2970) (Fig. 16C).

In contrast, IL-10 exhibited an opposing pattern: DMT treatment resulted in a significant upregulation of IL-10 mRNA in the peri-infarct cortex (1.59 ± 0.86 vs. 0.77 ± 0.63, p = .0487), while in the contralateral cortex there was a nonsignificant trend toward elevated expression (1.24 ± 0.71 vs. 0.63 ± 0.61, p = .0854) (Fig. 16D).

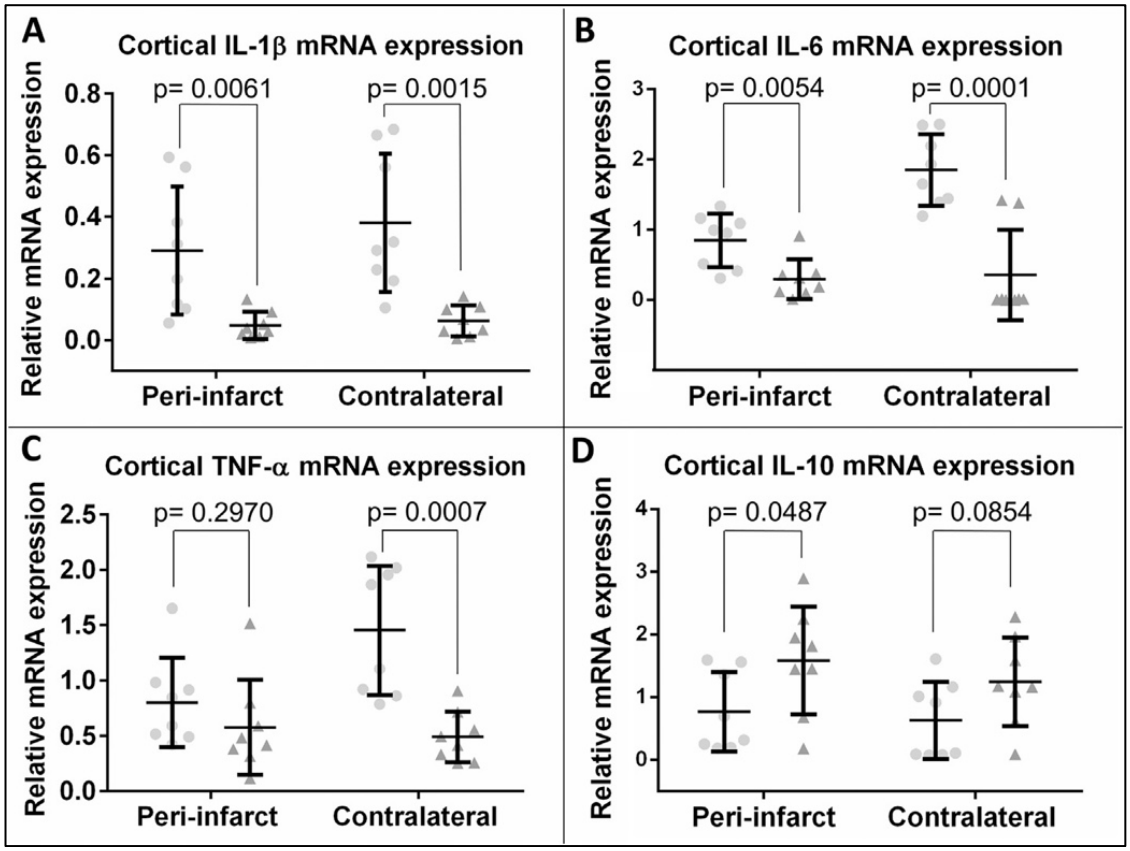

Fig. 16. Bilateral changes in inflammatory-regulator gene expression in the rat frontal cortex following DMT treatment after MCAO

Individual mRNA expression levels for each animal are displayed, with grey triangles representing the DMT-treated group (n = 8) and grey dots indicating controls (n = 8). **A:** DMT administration resulted in significantly reduced IL-1β mRNA expression in both the peri-infarct and contralateral cortices. **B:** A similar bilateral downregulation was observed for IL-6 mRNA expression in the DMT-treated group. **C:** TNF-α mRNA expression showed a decreasing trend in both hemispheres, but the reduction reached statistical significance only in the contralateral cortex. **D:** A significant upregulation of the anti-inflammatory cytokine IL-10 mRNA was detected in the peri-infarct cortex of the DMT-treated animals; however, no significant difference was found in the contralateral hemisphere. Bars represent mean ± standard deviation. Figure reproduced and legend adapted from: (141)

Initial assessment of circulating biomarkers—conducted without sigma-1 receptor antagonist treatment and without sham-operated controls—suggests that DMT exerts systemic anti-inflammatory effects.

To evaluate whether the transcriptional changes observed in the brain were reflected systemically, we quantified serum protein concentrations of the same key cytokines 25 hours post-MCAO in the same cohorts of animals (n = 8 per group). In alignment with the cortical mRNA data, serum levels of the pro-inflammatory cytokines IL-1β (53.88 ± 20.12 pg/ml vs. 151.40 ± 58.47 pg/ml, $p = 0.0006$), IL-6 (60.34 ± 19.63 pg/ml vs. 255.4 ± 113.00 pg/ml, $p = 0.0003$), and TNF-α (57.88 ± 25.22 pg/ml vs. 183.0 ± 69.65 pg/ml, $p = 0.0003$) were all significantly reduced in the DMT-treated animals compared to controls. In contrast, the concentration of the anti-inflammatory cytokine IL-10 was markedly elevated following DMT administration (146.80 ± 122.10 pg/ml vs. 21.31 ± 3.01 pg/ml, $p < 0.0115$) (Fig. 17A–D).

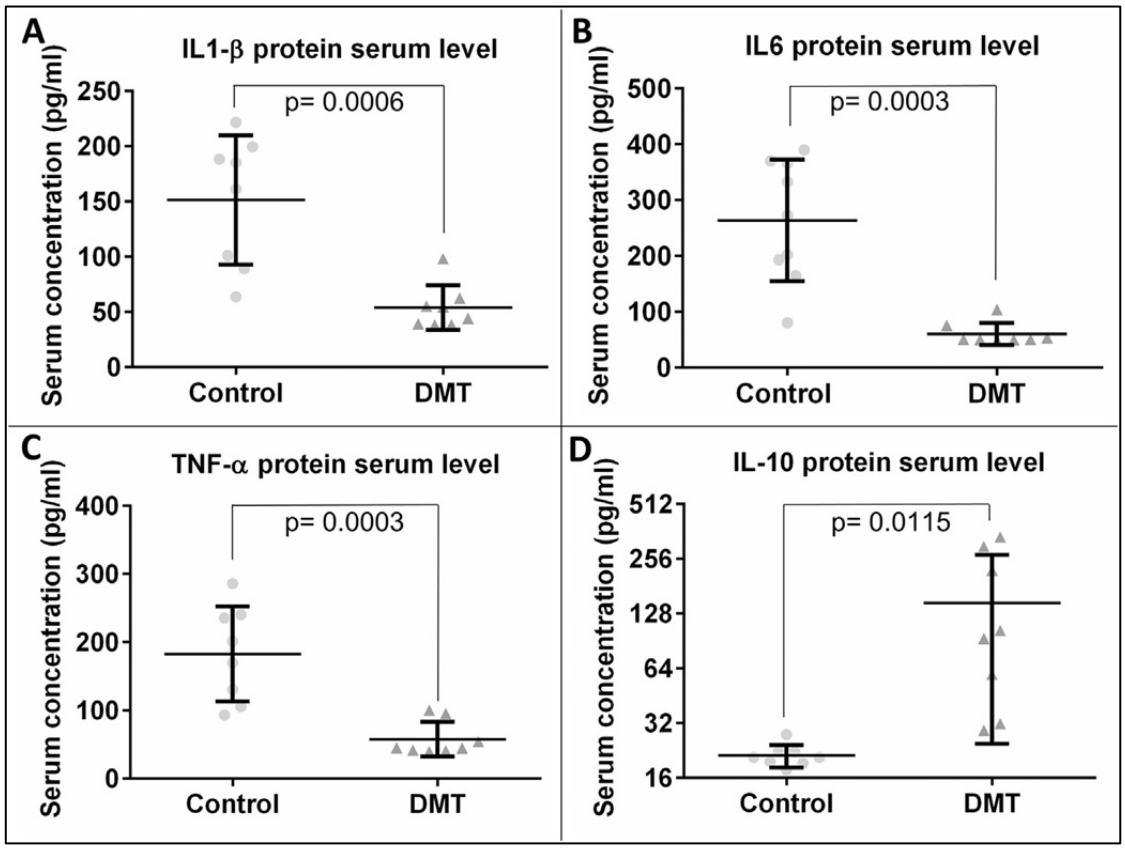

Fig. 17. Systemic anti-inflammatory response induced by DMT treatment following MCAO

Individual data points indicate serum protein concentrations in DMT-treated animals (grey triangles, n = 8) and vehicle-treated controls (grey dots, n = 8). Panels **A–C** show that serum levels of the pro-inflammatory cytokines IL-1β, IL-6, and TNF-α were significantly reduced in the DMT-treated group. Panel **D** demonstrates that the serum concentration of the anti-inflammatory cytokine IL-10 exhibited considerable variability but was significantly elevated in DMT-treated animals compared to controls. Bars represent mean ± standard deviation. Figure reproduced and legend adapted from: (141)

Comprehensive assessment of DMT-induced increases in circulating biomarkers including BD1063 treated and sham operated groups

Following cerebral ischemia, danger-associated molecular patterns (DAMPs) and inflammatory cytokines released from the injured brain can traverse the compromised blood–brain barrier (BBB), triggering peripheral innate immune responses (90). This

peripheral activation drives a broad-spectrum inflammatory reaction aimed at neutralizing potential threats through both humoral and cellular mechanisms (94).

To evaluate the systemic immune response associated with BBB breakdown and the modulatory effect of DMT, we measured serum cytokine concentrations and included a sham-operated control group for reference. Animals subjected to stroke exhibited significantly increased serum levels of pro-inflammatory cytokines TNFα, IL-6, CXCL-1, and CXCL-10 (Fig. 18A, C, E, F), along with a notable reduction in the anti-inflammatory cytokine IL-10 (Fig. 18D), compared to sham controls. Treatment with DMT significantly lowered circulating concentrations of TNFα, IL-1β, IL-6, CXCL-1, and CXCL-10, while simultaneously elevating IL-10 levels (Fig. 18A–F), indicating a systemic anti-inflammatory effect. Co-administration of the sigma-1 receptor antagonist BD1063 counteracted the anti inflammatory effect of DMT on TNFα, IL-1β, IL-6, and IL-10 (Fig. 18A–D), but failed to reverse the DMT-induced changes in the chemokines CXCL-1 and CXCL-10 (Fig. 18E–F).

To identify the cellular origin of inflammatory mediators in the circulation, gene expression analyses were conducted on peripheral blood mononuclear cells (PBMCs). Stroke induced a marked upregulation of TNFα, IL-6, CXCL-8, and CXCL-10 mRNA expression compared to the sham group (Fig. 18G, I, K, L). DMT treatment normalized these transcript levels, suggesting a suppressive effect on PBMC inflammatory activity. In contrast, IL-10 gene expression in PBMCs was significantly lower in DMT-treated animals than in both the sham and stroke groups (Fig. 18J), indicating that circulating IL-10 may originate from sources other than PBMCs. Notably, IL-1β mRNA levels remained unchanged across all experimental groups (Fig. 18H), further supporting the hypothesis that PBMCs are not the principal contributors to serum IL-1β following stroke. The addition of BD1063 did not reverse the transcriptional changes induced by DMT in PBMCs (Fig. 18G–L), suggesting that these effects occur via sigma-1 receptor–independent mechanisms.

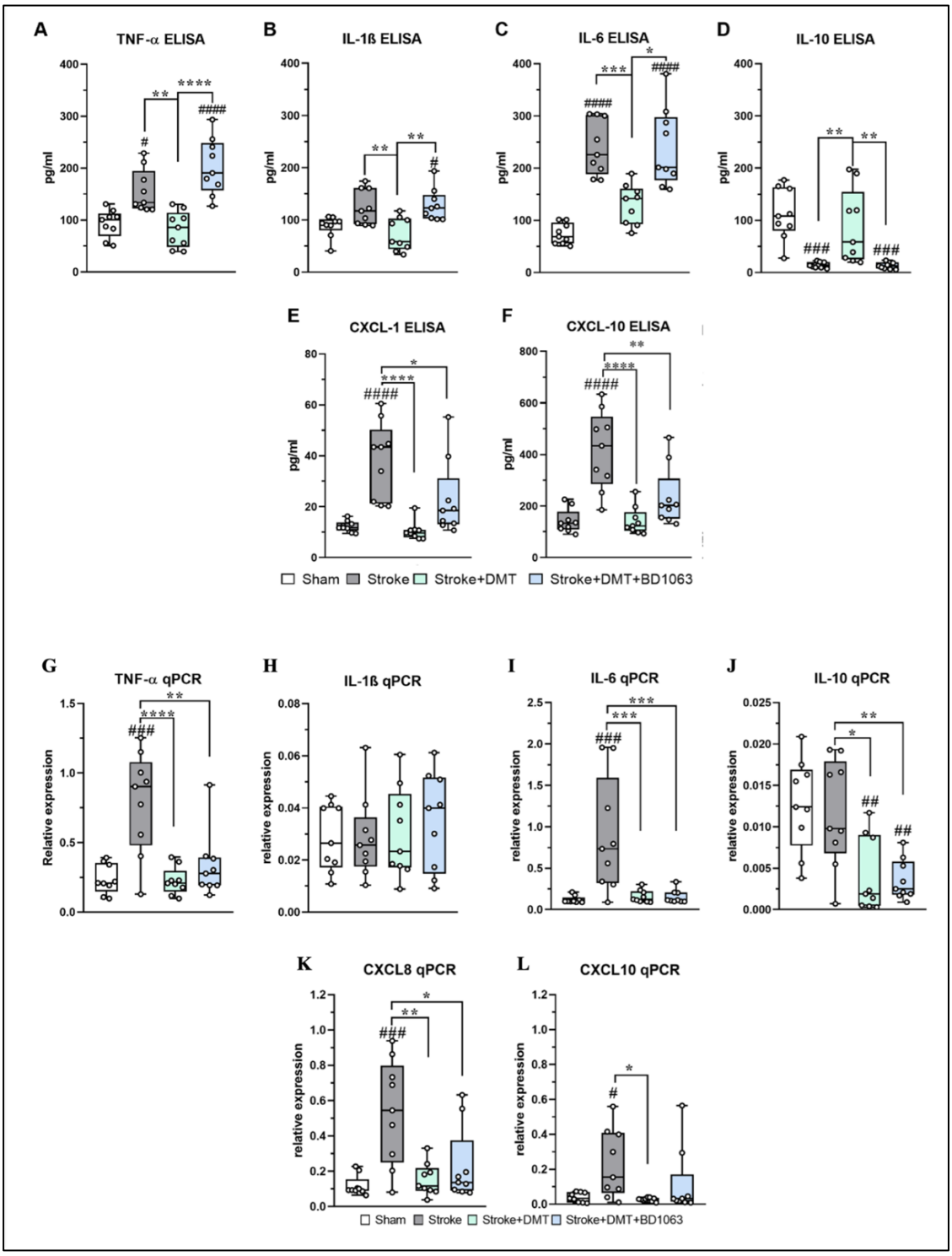
A
TNF-α ELISA
pg/ml
B
IL-1ß ELISA
pg/ml
C
IL-6 ELISA
pg/ml
D
IL-10 ELISA
pg/ml
E
CXCL-1 ELISA
pg/ml
F
CXCL-10 ELISA
pg/ml
Sham
Stroke
Stroke+DMT
Stroke+DMT+BD1063
G
TNF-α qPCR
Relative expression
H
IL-1ß qPCR
relative expression
I
IL-6 qPCR
relative expression
J
IL-10 qPCR
relative expression
K
CXCL8 qPCR
relative expression
L
CXCL10 qPCR
relative expression
Sham
Stroke
Stroke+DMT
Stroke+DMT+BD1063

Fig. 18. The anti-inflammatory effects of DMT in a rat unilateral stroke model
A–F: Serum concentrations of cytokines TNFα, IL-1β, IL-6, IL-10, CXCL-1, CXCL-10 were quantified using ELISA. **G–L:** Expression levels of TNFα, IL-1β, IL-6, IL-10, CXCL-8, and CXCL-10 mRNA in peripheral blood mononuclear cells (PBMCs) were assessed via qPCR. All groups included n = 9 animals. Data are shown as mean ± SD. Statistical analysis was performed using one-way ANOVA followed by Bonferroni's post hoc test. # $P < 0.05$, ## $P < 0.01$, ### $P < 0.001$, #### $P < 0.0001$: comparison with the sham group; * $P < 0.05$, ** $P < 0.01$, *** $P < 0.001$, **** $P < 0.0001$: comparisons among stroke groups. Figure reproduced and legend adapted from: (142)

DMT attenuates microglial activation following stroke

Microglial activation after cerebral ischemia is marked by distinct morphological alterations, including reduced branching, retracted processes, and enlarged cell bodies. Functionally, microglia display a predominantly pro-inflammatory phenotype during the first post-stroke week, which gradually shifts toward pro-repair roles. Nonetheless, microglia exhibit substantial heterogeneity, with cells of differing morphology and function coexisting throughout the timeline of injury (151, 160).

To examine the effect of DMT on post-stroke microglial activation, we performed IBA1 immunohistochemistry, evaluating both signal intensity (Fig. 19A) and morphological changes (Fig. 19C). A significant increase in IBA1 fluorescence intensity was observed in the ipsilateral hemisphere compared to the contralateral side in all experimental groups. DMT treatment did not influence IBA1 signal intensity, which reached the highest values in the DMT+BD1063 co-treated animals (Fig. 19B). In cultured glial cells, OGDR similarly elevated IBA1 staining in microglia, which was significantly reduced by DMT and reversed by BD1063 (Fig. 14C).

To further characterize microglial activation, we conducted quantitative morphometric analysis on individual microglia from peri-infarct regions, assessing parameters such as fractal dimension, lacunarity, density, span ratio, maximum span across hull, area, perimeter, circularity, maximum-to-minimum radius, and mean radius. Based on this multidimensional dataset, three distinct microglial clusters were defined:

Cluster 0 encompassed highly ramified, homeostatic microglia involved in environmental surveillance; Cluster 1 represented intermediately ramified, reactive microglia; and Cluster 2 included the least ramified, highly activated microglia characteristic of injury response (Fig. 19C).

In the contralateral hemisphere, Cluster 0 microglia predominated in all groups, with a smaller proportion of Cluster 1 cells also present (Fig. 20). Focal ischemia led to a prominent shift in microglial phenotype on the injured side, with a predominance of Cluster 2 cells and fewer Cluster 1 cells, while Cluster 0 microglia were nearly absent. DMT treatment mitigated this shift, resulting in a greater representation of Cluster 0 and 1 microglia and a reduced proportion of Cluster 2 cells. In contrast, animals co-treated with BD1063 exhibited a cluster distribution similar to the stroke-only group, indicating that the protective effect of DMT on microglial morphology was mediated through sigma-1 receptor signaling (Fig. 19D).

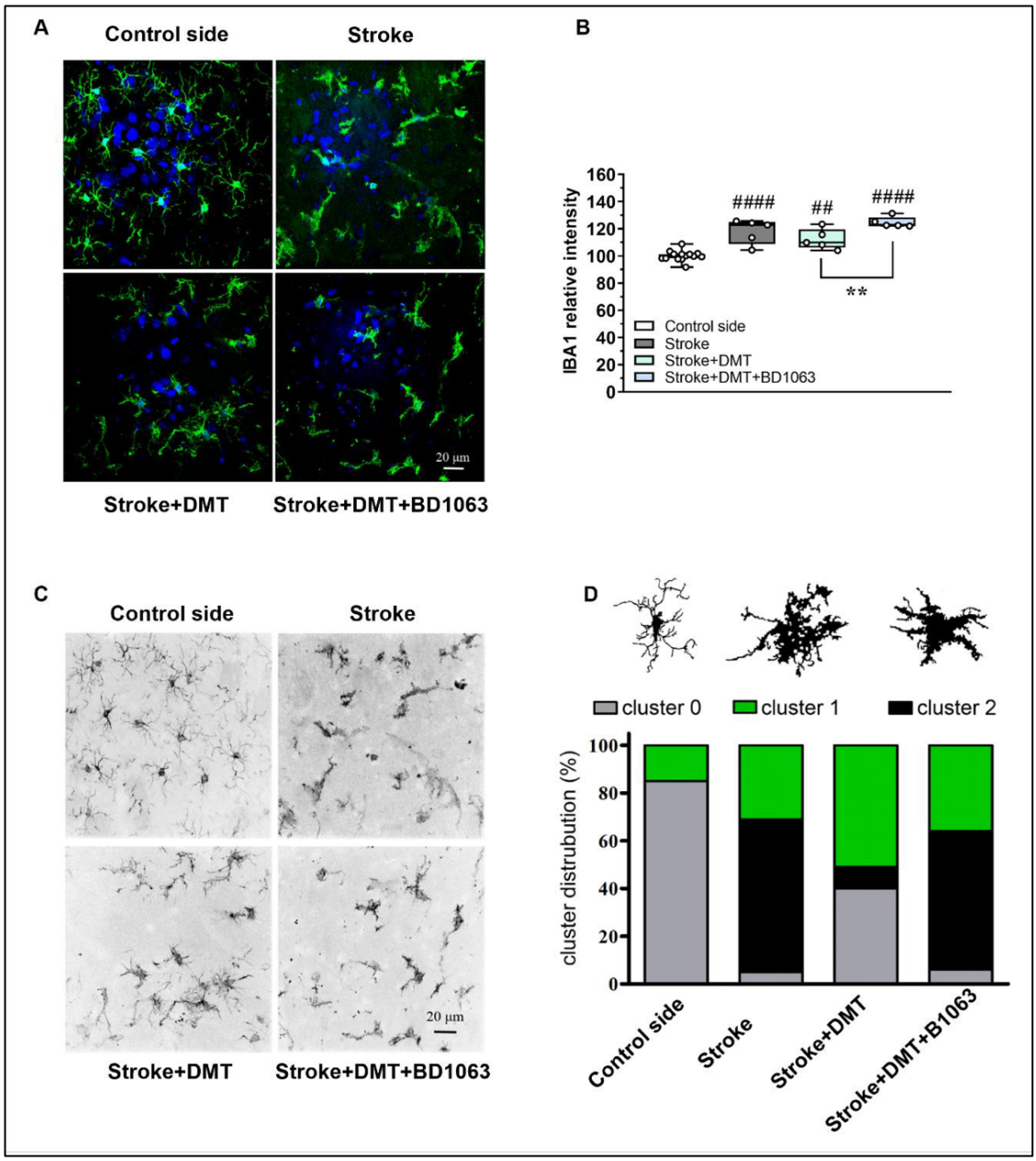
A
Control side
Stroke
20 μm
Stroke+DMT
Stroke+DMT+BD1063
B
IBA1 relative intensity
160
140
120
100
80
60
40
20
0
####
##
####
**
Control side
Stroke
Stroke+DMT
Stroke+DMT+BD1063
C
Control side
Stroke
20 μm
Stroke+DMT
Stroke+DMT+BD1063
D
cluster 0
cluster 1
cluster 2
cluster distrubution (%)
100
80
60
40
20
0
Control side
Stroke
Stroke+DMT
Stroke+DMT+B1063

Fig. 19. DMT preserves microglial morphology in a rat model of unilateral stroke

A: Representative IBA1 immunofluorescent images of microglial cells in brain sections across all experimental groups. **B:** Quantitative analysis of IBA1 immunofluorescence intensity. n = 5–15 images per group; values are shown as mean ± SD. Statistical analysis: one-way ANOVA followed by Bonferroni's post hoc test. ## $P < 0.01$, #### $P < 0.0001$ versus the control hemisphere; ** $P < 0.01$ versus the stroke + DMT group. **C:** Representative images illustrating IBA1-positive microglial cell morphology in each experimental condition. **D:** Proportional distribution of microglial morphological phenotypes: highly ramified, homeostatic (cluster 0, gray); moderately ramified, intermediate (cluster 1, green); and minimally ramified, reactive (cluster 2, black). Data represent analyses from n = 5 animals per group; 10 images per hemisphere per animal; a total of 553 cells per group were evaluated. Figure reproduced and legend adapted from: (142)

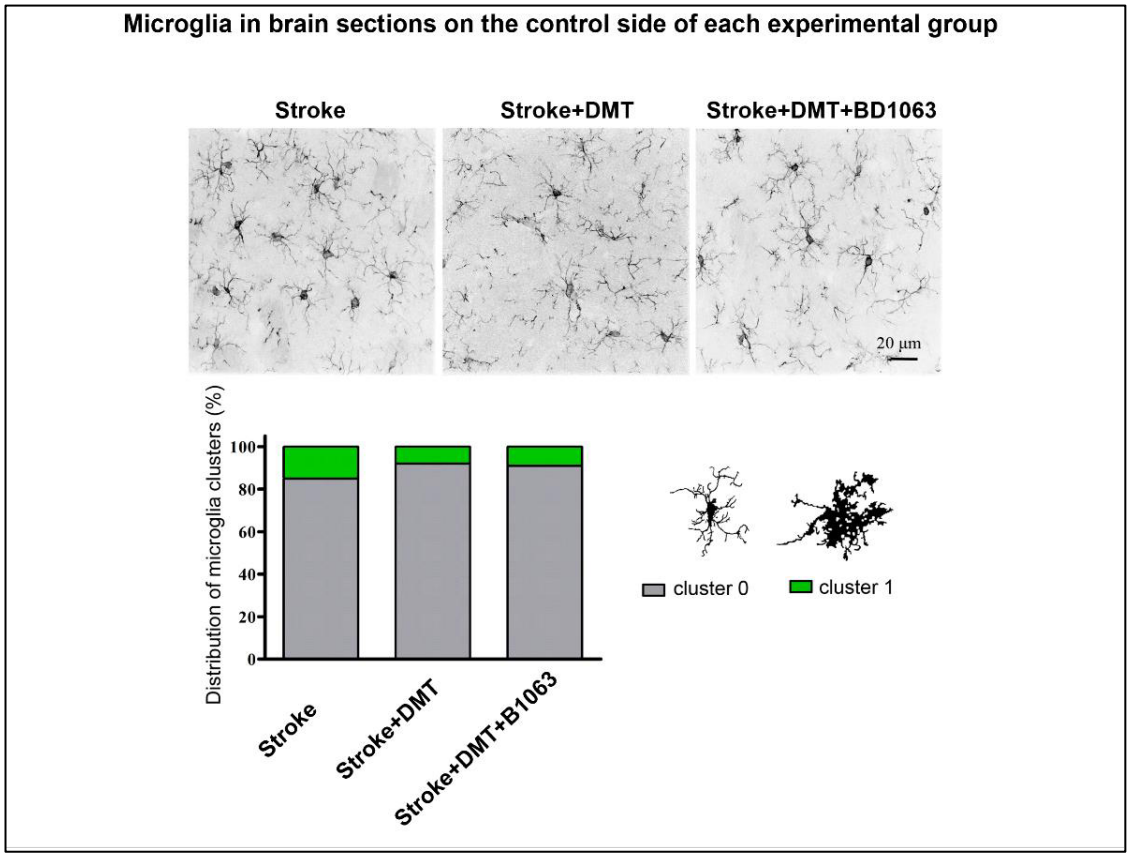

Fig. 20. Microglial morphology on the contralateral side in each experimental group revealed by IBA1 immunostaining

Representative IBA1-immunolabeled images show microglial cells in cortical brain sections on the uninjured hemisphere of rats subjected to experimental stroke. The examined groups include stroke, stroke + DMT, and stroke + DMT + BD1063. Based on morphological analysis, microglia were categorized into two clusters: cluster 0 (gray), consisting of highly ramified, homeostatic microglia; and cluster 1 (green), representing moderately ramified microglia responsive to subtle environmental changes. Across all experimental groups, cluster 0 microglia accounted for more than 80% of cells observed in the contralateral cortex. Figure reproduced and legend adapted from: (142)

S1R is expressed in neurons and microglia in the peri-infarct cortex

Consistent with previous findings (163), robust immunoreactivity for the sigma-1 receptor (S1R) was observed in the peri-infarct cortex following MCAO. Double immunofluorescence labeling revealed that S1R was co-localized with both the neuron-specific marker MAP-2 and the microglia-specific marker IBA-1 across all examined animals, confirming its expression in these cell types within the injured cortical region (Fig. 21).

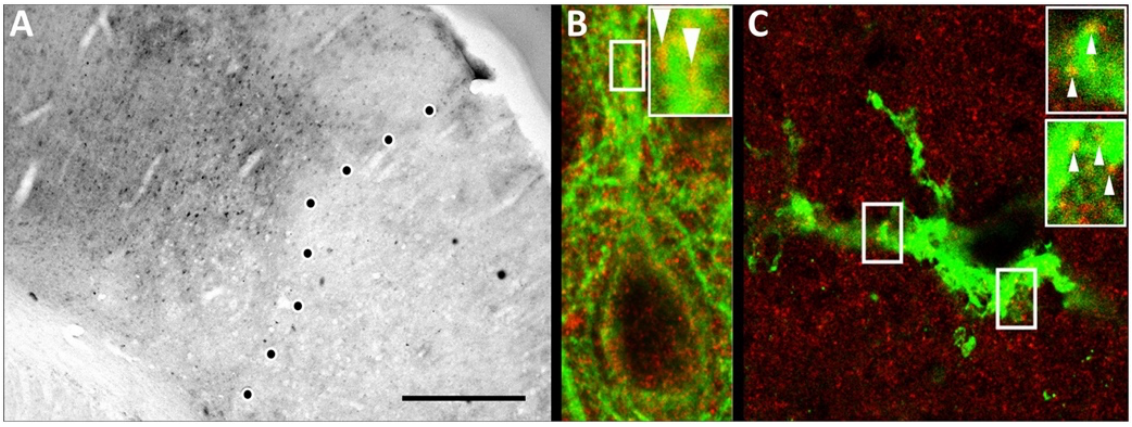

Fig. 21. Demonstration of S1R expression in the peri-infarct cortex following DMT treatment, and its co-localization with neuronal and microglial markers

A: Increased anti-S1R immunoreactivity (1:200) was detected in the peri-infarct cortex, while no labeling was observed within the infarct core. The localization of the immunostaining corresponded to the lesion border, as delineated by the dotted line. Scale bar = 500 μm. **B and C:** Dual immunofluorescence revealed S1R (1:500) as red puncta, whereas neurons were identified using MAP-2 (1:200) **(B)** and microglia using IBA-1 (1:100) **(C)**, both shown in green fluorescence. Insets from high-magnification images demonstrate clear co-localization of S1R with both neuronal and microglial markers. Figure reproduced and legend adapted from: (141)

Decreased apoptosis following DMT treatment

Twenty-five hours after MCAO, a significant downregulation in APAF1 mRNA expression—an essential regulator of the intrinsic apoptotic pathway—was observed in DMT-treated animals (n = 8) compared to controls (n = 8), both in the peri-infarct cortex (0.12 ± 0.02 vs. 0.22 ± 0.19, $p = 0.0357$) and in the corresponding contralateral region (0.02 ± 0.04 vs. 0.37 ± 0.02, $p = 0.0011$) (Fig. 22A). These transcriptional findings were paralleled by serum protein measurements: circulating APAF1 levels were markedly reduced in the DMT group compared to vehicle-treated controls (0.79 ± 0.98 ng/ml vs. 6.72 ± 2.03 ng/ml, $p < 0.0001$) (Fig. 22B).

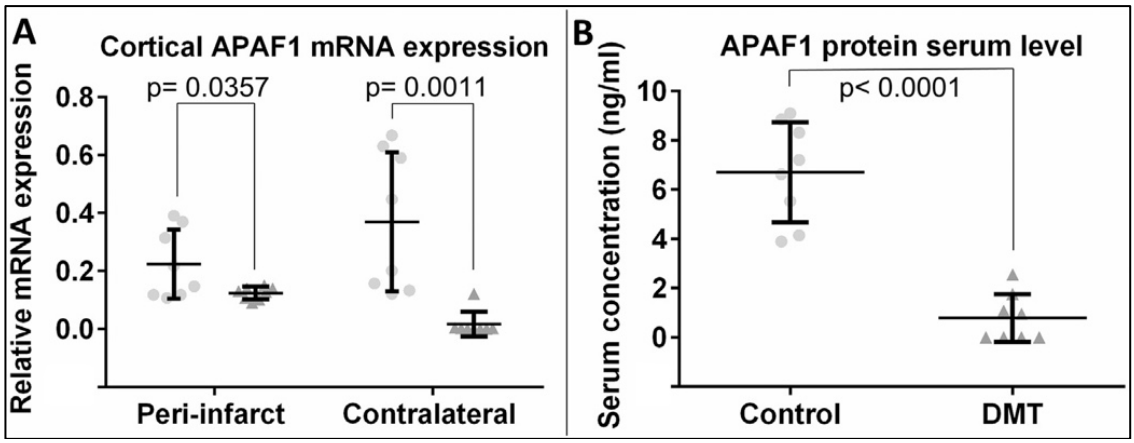

Fig. 22. DMT-induced reduction in cortical APAF1 mRNA expression and serum protein concentration following MCAO

Individual APAF1 mRNA expression values and serum protein concentrations are displayed for DMT-treated animals (grey triangles, $n = 8$) and controls (grey dots, $n = 8$). **A:** DMT administration resulted in a significant decrease in APAF1 mRNA levels in both the peri-infarct and contralateral cortices. **B:** Similarly, serum APAF1 protein concentrations were markedly lower in the DMT-treated group. Bars represent mean ± SD. Figure reproduced and legend adapted from: (141)

Preliminary analysis of neurotrophic factor levels in the cortex and serum, without sigma-1 receptor antagonist treatment or sham-operated controls

The mRNA expression of brain-derived neurotrophic factor (BDNF), a key molecule involved in neuroregeneration and synaptic plasticity, was found to be significantly elevated in both the peri-infarct region (0.009 ± 0.002 vs. 0.006 ± 0.002, $p = 0.0273$) and the contralateral cortex (0.011 ± 0.007 vs. 0.003 ± 0.002, $p = 0.0048$) of DMT-treated animals compared to vehicle-treated controls (n = 8 per group). Correspondingly, the circulating levels of BDNF protein were markedly increased in the DMT group (127.70 ± 46.16 pg/ml vs. 27.66 ± 6.41 pg/ml, $p < 0.0001$) (Fig. 23A–B).

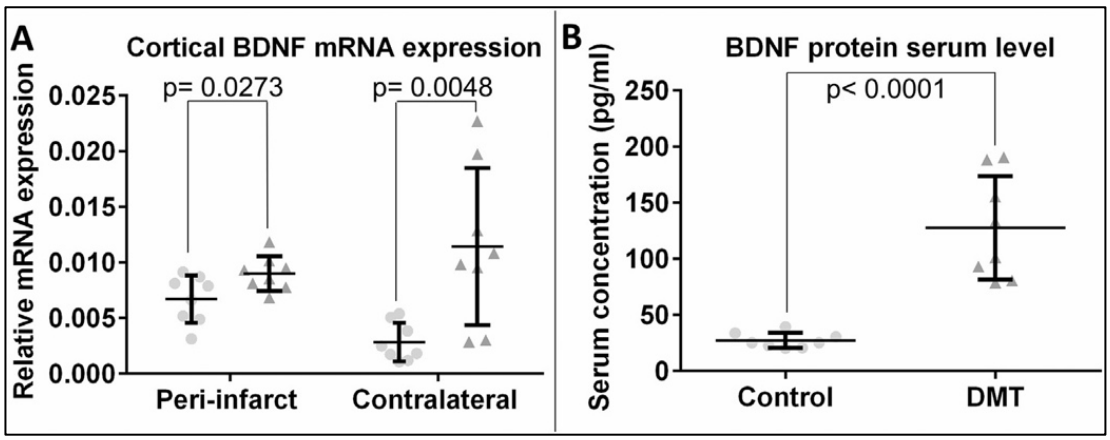

Fig. 23. DMT-induced changes in cortical BDNF expression and serum protein levels following MCAO.

Panel **A** shows a bilateral upregulation of BDNF mRNA expression in the cortex following DMT treatment. In panel **B**, serum BDNF protein levels are significantly elevated in the DMT-treated group compared to controls. Bars represent mean ± standard deviation. Figure reproduced and legend adapted from: (141)

Assessment of serum neurotrophic factor levels, including sigma-1 receptor antagonist–treated and sham-operated control groups

Serum levels of the neurotrophin BDNF were significantly higher in DMT-treated animals compared to vehicle-treated controls. This DMT-induced elevation in BDNF was abolished by BD1063, implicating the involvement of sigma-1 receptor signaling (Fig. 24).

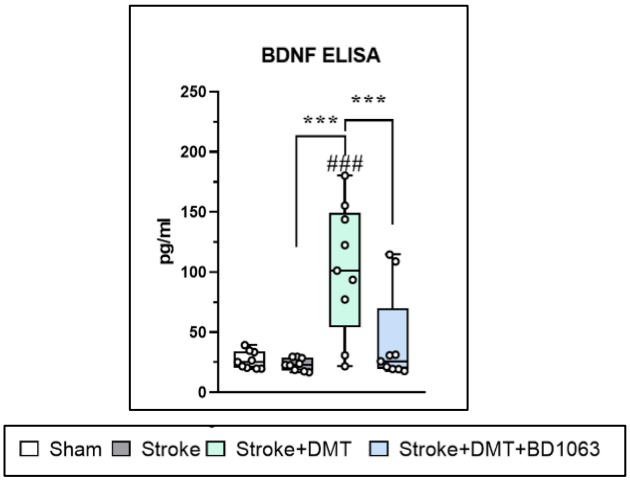

Fig. 24. Serum levels of the neurotrophic factor BDNF quantified by ELISA in rats 24 hours after stroke

All groups included n = 9 animals. Data are shown as mean ± SD. Statistical analysis was performed using one-way ANOVA followed by Bonferroni's post hoc test. ### $P < 0.001$: comparison with the sham group; *** $P < 0.001$: comparisons among stroke groups. Figure reproduced and legend adapted from: (142)

Improved motor function following DMT treatment

To evaluate functional recovery, staircase testing was conducted in two experimental groups (n = 8 per group) after successful pre-training. Animals receiving DMT treatment for 24 hours exhibited significantly improved motor performance of the left forelimb compared to untreated controls. Statistically significant differences between the groups emerged by postoperative day 4 (2.1 ± 0.9 pellets vs. 0 ± 0.0 pellets, $p = 0.0325$), and this divergence became more pronounced by the final assessment on day 30 (6.3 ± 3.5 pellets vs. 1.6 ± 3.1 pellets, $p = 0.0084$) (Fig. 25A). Notably, no differences were observed between groups in the performance of the right forelimb (Fig. 25B).

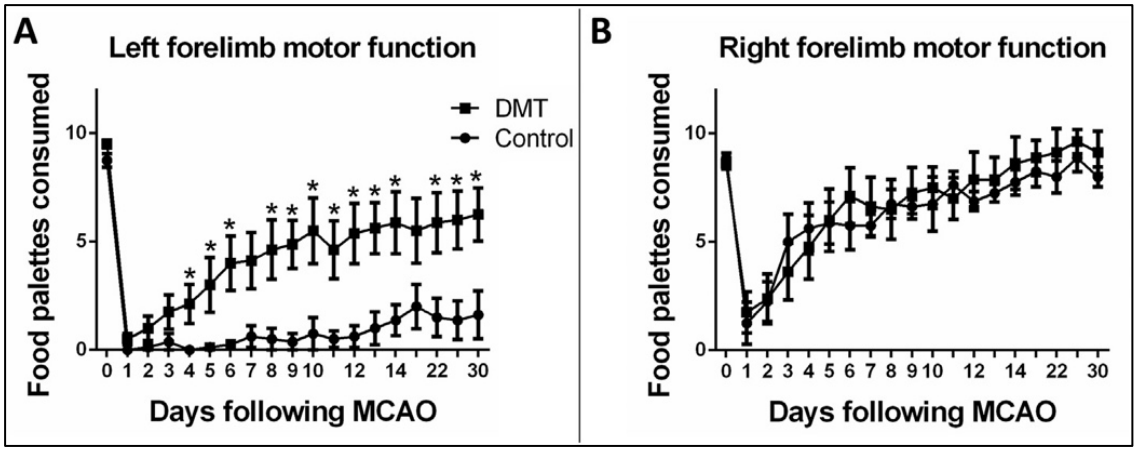

Fig. 25. The effect of DMT on motor function recovery

A: The outcomes of the serial staircase test demonstrate a marked divergence in motor recovery between the experimental groups, specifically in the affected (left) forelimb. From postoperative day 4 onward, rats receiving DMT treatment (line with squares) exhibited significantly improved performance, retrieving a greater number of food pellets with their left forelimb compared to the control group (line with dots) **B:** In contrast, no inter-group difference was observed in right forelimb function throughout the study period. Bars indicate the standard error of the mean. Figure reproduced and legend adapted from: (141)

5. Discussion

Despite decades of intensive investigation, translating neuroprotective strategies into effective clinical treatments for ischemic stroke remains a major challenge. Beyond direct neuronal damage, ischemia initiates a cascade of spatially and temporally well-characterized events, including prompt activation of microglia, endothelial cells, pericytes, and glial cells, release of proinflammatory mediators initiating and maintaining neuroinflammation with subsequent opening of the blood–brain barrier (6, 7). The resulting albumin extravasation and the wave of peripherial white blood cell infiltration further compromise BBB integrity, escalalting neuroinflammation and secondary lesion expansion (4, 8, 9).

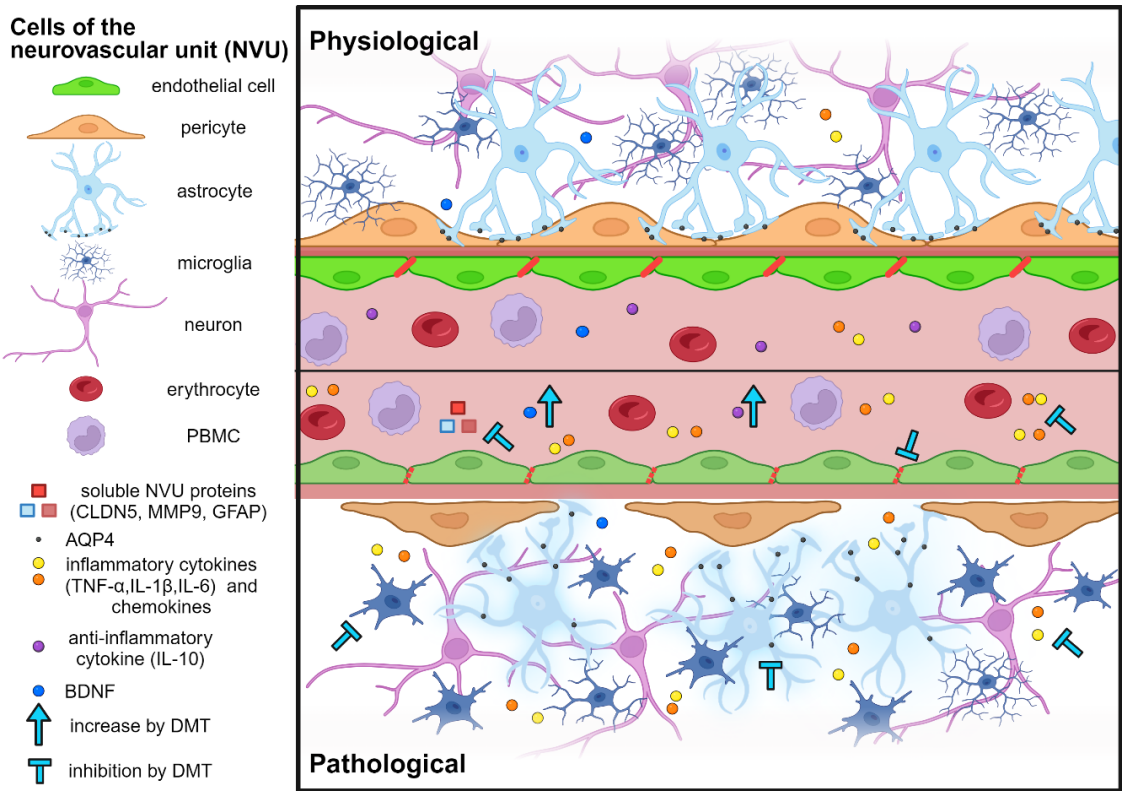

Fig. 26. BBB changes in stroke and the protective effects of DMT

Schematic representation of the neurovascular unit (NVU) in physiological condition and in stroke. Arrows and inhibition signs (cyan) show the effect of the DMT in pathological condition. In stroke tight junctions (red line between brain endothelial cells) are disrupted and CLDN5 tight junction protein is decreased, in the blood soluble neurovascular unit proteins appear, the level of the inflammatory cytokines increases and that of anti-inflammatory cytokines decreases. In the brain the morphology of microglia changes, the ratio of less ramified microglia cells increases, the AQP4 distribution changes and the level of inflammatory cytokines increases. DMT decreases the level of soluble CLDN5, MMP9 and GFAP proteins and inhibits inflammatory cytokines in the blood, while it increases the level of BDNF and the anti-inflammatory cytokine IL-10. In the brain DMT inhibits the morphological changes in microglia, the redistribution of AQP4 in astroglia and decreases proinflammatory cytokine production. Abbreviations: AQP4 aquaporin-4; BDNF, brain-derived neurotrophic factor; CLDN5, claudin-5; GFAP, glial fibrillary acidic protein; MMP9, matrix metalloproteinase-9; PBMC, peripheral blood mononuclear cell. Figure reproduced and legend adapted from: (142)

Based on the accumulated evidence regarding DMT and sigma-1 receptor signaling, our research group was the first to evaluate the in vivo cytoprotective effects of DMT in the context of cerebral ischemia–reperfusion injury.

Our findings demonstrate that continuous DMT administration, initiated at the time of reperfusion, significantly reduces ischemic brain injury in rats. Histological analysis revealed that infarct core volume was reduced in DMT-treated animals compared to controls. To validate the histological measurements, magnetic resonance imaging (MRI) was performed 24 hours post-occlusion. T2-weighted scans confirmed the neuroprotective effect of DMT, revealing smaller hyperintense areas corresponding to infarct volume in the treated group. Drawing on earlier in vitro data, we hypothesized that S1R may be a relevant mediator of DMT's neuroprotective action (132). To determine whether this effect was indeed mediated by S1R activation, a group of animals was co-treated with the S1R antagonist BD-1063 alongside DMT. These animals exhibited significantly larger infarct volumes than those receiving DMT alone, comparable to

untreated controls, confirming that the neuroprotective action of DMT is S1R–dependent. These findings are consistent with earlier in vitro studies demonstrating the cytoprotective properties of DMT under hypoxic conditions (132, 164) and in a rat model of renal ischemia–reperfusion injury (165).

To gain insight into the mechanisms underlying DMT's neuroprotective effects, we investigated four key processes involved in post-stroke pathology: **BBB integrity, apoptosis, inflammation, and neuroplasticity.**

BBB integrity is regarded as a key therapeutic target in stroke, with various protective molecules and approaches being extensively studied (166). In our experiment, DMT treatment led to a marked reduction of edema in post-stroke histological brain sections, which was accompanied by a significant attenuation of FITC-albumin leakage into both the brain parenchyma and cerebrospinal fluid. The observed reduction in edema and FITC–albumin leakage suggests that DMT's effects are related as much to stabilizing the BBB as to providing direct neuroprotection. To further validate the in vivo findings on BBB protection, we employed an in vitro co-culture BBB model subjected to oxygen–glucose deprivation and reoxygenation (OGDR). DMT treatment significantly reduced the elevated albumin flux across the barrier observed after OGDR, indicating a protective effect on the transcellular pathway and improved BBB integrity under hypoxic conditions compared to controls. While not reaching statistical significance, changes in the paracellular pathway—specifically in the transendothelial electrical resistance and fluorescein permeability—showed a noticeable trend. Additionally, DMT preserved endothelial cell viability, as demonstrated by metabolic activity assays, although it did not restore function in pericytes, which remained highly vulnerable to OGDR—consistent with earlier reports (158, 167). Given that brain endothelial cells are central components of the neurovascular unit and play a primary role in maintaining BBB integrity we analyzed the transcriptomic profile of brain endothelial cells following OGDR and found substantial changes in gene expression linked to cellular stress, extracellular matrix remodeling, and cell proliferation. In contrast, DMT treatment induced only modest transcriptional changes. A limited subset of genes related to inflammation sensing, anti-inflammatory signaling, and glucose metabolism was affected, suggesting that while DMT influences anti-inflammatory gene expression in endothelial cells, these may not

represent its primary cellular target. Notably, these effects were not reversed by BD-1063, suggesting a S1R–independent mechanism of endothelial gene regulation.

CLDN5 immunostaining both in vivo and in vitro revealed that tight junction integrity was compromised under stroke-like conditions but preserved in DMT-treated groups, with a statistically significant effect observed in histological brain sections and a non-significant trend in cell cultures. Correspondingly, DMT treatment reduced serum levels of the soluble neurovascular unit markers CLDN5 and GFAP, indicating improved blood–brain barrier stability. The clinical relevance of this observation lies in the fact that lower serum levels of BBB markers in the acute phase of stroke have been associated with better long-term outcomes (22, 43, 162).

Stroke-associated edema, a clinically important phenomenon, was reduced by DMT treatment as revealed by histological analysis. This effect may be attributable to the attenuation of stroke-induced increase in AQP4 staining intensity and redistribution—indicative of astrocyte cytotoxic swelling (15-17)—observed in DMT-treated animals. GFAP intensity, a marker of astrocytic activation assessed by immunohistochemistry, was also significantly reduced by DMT treatment in the cell culture model, although it was not significantly altered in vivo in rat brain histological sections. The observed reduction in lesion volume and edema, together with preserved BBB integrity, supports the therapeutic potential of DMT as a BBB-protective agent.

Inflammation, a major contributor to secondary neuronal injury following stroke (4-9), was also modulated by DMT. Microglial activation, a well-documented feature of early stroke pathology (6), is characterized by morphological transformation and rapid production of proinflammatory cytokines and matrix metalloproteinase-9 (MMP-9) within hours of ischemia playing a central role in the initiation and maintenance of neuroinflammation (69, 72, 73, 168, 169). DMT preserved the highly ramified, homeostatic morphology of microglia, preventing their transition to a reactive, amoeboid phenotype.

In the pathomechanism of stroke, damage-associated molecular patterns (DAMPs), cytokines, and chemokines released from the brain cross the compromised blood–brain and blood–CSF barriers, where they interact with the peripheral immune system and activate systemic immunity (91, 92). Peripheral innate immune cells are rapidly activated

through leukocyte pattern recognition receptors (91), leading to profound changes in their gene expression profiles, particularly those involved in activation and differentiation (109, 110). This is followed by an increased production of inflammatory mediators and elevated serum cytokine levels within hours after ischemia (94, 95). This cascade leads to a wave of peripheral immune cells invading the infarcted area, exacerbating neuroinflammation and causing secondary lesion expansion. A series of clinical data supports the fact that the extent of the activation of the peripheral immune system is related to brain infarct volume, stroke severity, and long-term outcomes (97-102). Suppression of the peripheral inflammatory response after stroke—alongside the inhibition of microglia in the central nervous system—was also observed following DMT treatment. In PBMCs, mRNA expression of proinflammatory cytokines (except IL-1β) and chemokines was markedly downregulated in response to DMT. The mitigation of both microglial and peripheral immune activation may be causally related to the finding that DMT significantly attenuated the stroke-induced elevation of serum MMP-9, a key mediator of BBB disruption and neuroinflammation (61, 62). Notably, lower MMP-9 levels have been associated with better long-term outcomes in clinical observations (63-68, 170). Furthermore, cortical mRNA expression and serum levels of the proinflammatory cytokines IL-1β, IL-6, and TNF-α were markedly reduced following DMT administration (although the reduction in cortical TNF-α mRNA did not reach statistical significance). These anti-inflammatory effects were reproducible in vitro. In the co-culture BBB model, cytokine assays demonstrated that DMT suppressed OGDR-induced secretion of TNF-α, IL-1β, and IL-6 in a S1R–dependent manner, with more pronounced effects observed in the abluminal compartment—likely reflecting the contribution of microglia, astrocytes, and pericytes (161). In addition, DMT significantly reduced serum levels of the chemokines CXCL-1 and CXCL-10, while simultaneously increasing both cortical mRNA and serum concentrations of the anti-inflammatory cytokine IL-10, which is of known clinical significance, as decreased serum IL-10 levels in stroke patients have been independently associated with neurological worsening (107) and poor functional recovery (108).

Apoptosis, as reflected by the expression of APAF1—a central mediator of mitochondria-mediated cell death (171)—was significantly decreased in the cortex of DMT-treated animals, and circulating APAF1 protein levels were likewise reduced,

suggesting attenuation of apoptotic signaling, which possibly contributes to the observed cytoprotective effects.

Neuroplasticity: From a clinical perspective, one of the most relevant findings of our study relates to enhanced neuroplasticity after DMT treatment, as evidenced by the improved motor function recovery observed in DMT-treated animals during the 30-day post-stroke period, assessed through forelimb functional testing. This sustained recovery suggests that DMT may not only mitigate acute neuronal injury but also support long-term neurological repair. This effect was accompanied by increased cerebral BDNF mRNA expression and elevated serum BDNF protein levels in a sigma-1 receptor-dependent manner, indicating a robust neurotrophic response. BDNF is an essential promoter of synaptogenesis and neuronal viability (172). Clinical data indicate that higher serum BDNF levels are associated with a more favorable prognosis (173) and a reduced risk of post-stroke cognitive impairment (174). These findings are consistent with previous reports linking S1R activation to enhanced BDNF expression following cerebral ischemia (175).

These results have led to the launch of a phase 1 clinical trial (NCT05559931) investigating the safety and pharmacokinetics of single and repeated intravenous doses of DMT in healthy individuals, and to the preparation of a phase 2 trial aimed at evaluating DMT's ability to enhance neuroplasticity and support long-term recovery in patients after acute stroke.

The observation that some effects of DMT are dependent on S1R activation while others are not, highlights the complexity of its mechanism of action. Co-administration of BD-1063 successfully inhibited several key effects of DMT, including infarct volume reduction, suppression of inflammatory cytokines in vivo and in vitro, elevation of serum BDNF, reduction of serum GFAP levels, attenuation of CLDN5 and AQP4 immunoreactivity, and preservation of ramified microglial morphology. In contrast, parameters such as in vitro albumin permeability, serum levels of chemokines, MMP-9 and CLDN5, PBMC gene expression, and endothelial transcriptomic profiles were unaffected by BD-1063. These findings indicate that DMT exerts its neuroprotective effects through multiple, partially overlapping mechanisms, involving both S1R–dependent and –independent pathways. Notably, previous studies have reported that not

only S1R agonists such as PRE-084 (176) but also antagonists like E-52862 (177) may confer neuroprotection in ischemic stroke models. This underscores the pharmacological complexity of the sigma-1 receptor and highlights the need for further research to elucidate the distinct and potentially overlapping actions of its ligands (178).

Key limitations should be noted. First, our in vivo experiments were conducted exclusively in young, healthy male Wistar rats; thus, translatability to the typical clinical stroke population—older patients with multiple comorbidities and concomitant medications—may be limited, and future studies should test DMT in pathological/comorbidity-enriched models, especially given the intention to progress toward phase 2 evaluation. Moreover, for standardization we used only male animals in the in vivo experiments; although our in vitro work included endothelial cells derived from both male and female donors, sex-specific effects cannot be excluded. Given reported sexual dimorphism in Sigma-1 receptor–related and serotonergic signaling, the magnitude of DMT's effects may differ in females. With the current sample size and the substantial variability in stroke lesion volumes, detecting robust sex differences was not feasible at this stage; however, after clarifying the contribution of serotonin receptors, dedicated sex-stratified in vivo studies will be an important next step. Second, although endogenous DMT is measurable in rodents and may reach neurotransmitter-like brain concentrations after ischemia, direct, validated detection in human brain tissue is currently lacking; in humans, evidence is indirect, based on detection in body fluids and on the presence of the key biosynthetic enzyme INMT in the brain. Third, the DMT dose used here likely induce a transient, non-negligible increase in blood pressure, which could theoretically augment the risk of hemorrhagic transformation—particularly after reperfusion—yet our study did not include targeted hemodynamic monitoring.

Translational feasibility: From a translational perspective, DMT appears most realistically positioned as a prehospital, MAO-inhibitor–free, slow intravenous infusion that can be started rapidly, titrated, and stopped immediately, without delaying thrombolysis or thrombectomy**.** Phase I human data suggest that prolonged sub-psychedelic infusion regimens are generally well tolerated with minimal perceptual effects**,** whereas the dose used in our animal experiments is clearly psychedelic, underscoring the need for clinically feasible dosing strategies rather than receptor blockade: although hallucinations could be attenuated with 5-HT2A antagonism, this may

also blunt 5-HT2A-dependent plasticity, and DMT's actions likely emerge from its broad, multi-receptor profile and coordinated effects within the CNS microenvironment (neurons, astrocytes, microglia, progenitors, infiltrating leukocytes). Its rapid blood–brain barrier penetration and short half-life make it an attractive "bridging" therapy aimed at slowing penumbral decay and potentially extending the treatment window, while not interfering with reperfusion therapies (it is neither anticoagulant nor antiaggregant). Importantly, drug delivery to the infarct core will be limited by no-flow, whereas the penumbra should remain accessible via collateral circulation; therefore, further preclinical work in permanent occlusion and hemorrhagic stroke models is warranted to reflect real-world diagnostic uncertainty and to better define safety and efficacy in clinically relevant scenarios.

6. Conclusion

Stroke-induced damage is a dynamic process that directly affects elements of the neurovascular unit, leading to the breakdown of the functional blood-brain barrier and resulting in the exacerbation of inflammation, edema, and secondary injury (179).

Our study demonstrates that DMT exerts a neuroprotective effect in rats following focal cerebral infarction, as evidenced by reduced infarct and edema volumes, and promotes neuroplasticity, as indicated by improved long-term functional recovery. Administration of DMT at the time of reperfusion exerts a protective effect on BBB structure and function, suppresses both central and peripheral immune responses, and downregulates apoptosis-related signaling. These effects are mediated through both sigma-1 receptor–dependent and –independent mechanisms, involving multiple cell types across the neurovascular unit.

Identifying treatments that protect not only neurons but also preserve BBB integrity—a key factor in secondary lesion expansion—is critical for improving stroke outcomes. Considering the endogenous nature of DMT and its strong receptor affinity in the human brain, DMT may hold significant potential to complement current standard stroke therapies.

7. Summary

Stroke-induced brain injury is a complex and dynamic process that disrupts the structural and functional integrity of the neurovascular unit and leads to increased blood–brain barrier (BBB) permeability. This pathomechanism plays a key role in amplifying the inflammatory response, promoting edema formation, and driving the progression of lesion size. The clinical applicability of current therapeutic options—intravenous thrombolysis and mechanical thrombectomy—is limited; therefore, identifying adjunct neuroprotective strategies is of major importance.

The endogenous compound N,N-dimethyltryptamine (DMT) rapidly crosses the BBB and binds with high affinity to multiple receptor systems, including the sigma-1 receptor (S1R). Given that S1R modulation has been shown to enhance cellular stress tolerance and support pro-survival mechanisms, the aim of our study was to determine whether DMT can reduce the extent of ischemic brain injury and, if so, through which receptor pathways.In a rat transient middle cerebral artery occlusion model, DMT administered at reperfusion significantly reduced infarct and edema size and mitigated BBB damage. In a complementary in vitro BBB model, DMT improved endothelial cell viability and attenuated ischemia-induced albumin permeability. In addition, treatment inhibited stroke-induced local microglial activation and the peripheral immune response, and reduced the production of pro-inflammatory cytokines and chemokines. During 30-day functional follow-up, DMT-treated animals demonstrated enhanced motor recovery, accompanied by increased BDNF levels measured in the cerebral cortex and in serum.

Overall, our findings suggest that the neuroprotective effect of DMT is mediated through preservation of BBB structure and function, attenuation of neuroinflammation and apoptosis-related signaling, and promotion of neuroplasticity. These mechanisms proceed via both sigma-1 receptor–dependent and –independent pathways, with integrated involvement of multiple cell types within the neurovascular unit. Owing to its endogenous nature and receptor affinity in the human brain, DMT may represent a promising therapeutic candidate to complement current standard stroke treatments.

Összefoglalás

A stroke által kiváltott agykárosodás komplex és dinamikus folyamat, amely a neurovaszkuláris egység strukturális és funkcionális integritásának megbomlásával jár, és a vér–agy gát permeabilitásának fokozódásához vezet. Ez a patomechanizmus kulcsszerepet játszik a gyulladásos válasz felerősítésében, az ödéma kialakulásában és a lézió méretének progressziójában. A jelenlegi terápiás lehetőségek – intravénás trombolízis és mechanikus trombektómia – klinikai alkalmazhatósága korlátozott, ezért a kiegészítő neuroprotektív stratégiák azonosítása kiemelt jelentőséggel bír.

Az endogén eredetű N,N-dimetiltriptamin (DMT) gyorsan átjut a vér–agy gáton, és több receptorrendszerhez, köztük a szigma-1 receptorhoz (S1R) is nagy affinitással kötődik. Tekintettel arra, hogy az S1R modulációja bizonyítottan fokozza a sejtek stressztoleranciáját és elősegíti a túlélési mechanizmusokat, vizsgálatunk célja annak meghatározása volt, hogy a DMT képes-e csökkenteni az iszkémiás agykárosodás mértékét, és ha igen, mely receptorútvonalakon keresztül.

Patkány tranziens a. cerebri media-okklúziós modellben a reperfúzió mellett adott DMT szignifikánsan mérsékelte az infarktus- és ödémaméretet, valamint csökkentette a vér–agy gát károsodását. Komplementer, vér–agy gátat modellező in vitro sejttenyészetben a DMT javította az endotélsejtek életképességét és mérsékelte az iszkémia okozta albumin-permeabilitást. Ezen túlmenően a kezelés gátolta a stroke által kiváltott lokális mikroglia-aktivációt és a perifériás immunválaszt, valamint mérsékelte a proinflammatorikus citokinek és kemokinek termelődését. 30 napos funkcionális utánkövetés során a DMT-vel kezelt állatok fokozott motoros regenerációt mutattak, amelyet az agykéregben és a szérumban mért emelkedett BDNF-szint kísért.

Eredményeink összességében arra utalnak, hogy a DMT neuroprotektív hatása a vér–agy gát struktúrájának és funkciójának megőrzésén, a neuroinflammáció és az apoptotikus jelátvitel mérséklésén, valamint a neuroplaszticitás elősegítésén keresztül valósul meg. E mechanizmusok részben szigma-1 receptor-függő, részben attól független útvonalakon keresztül mennek végbe, a neurovaszkuláris egység több sejttípusának integrált részvételével. Endogén jellegéből és az emberi agyban meglévő receptor-affinitásából fakadóan a DMT ígéretes terápiás potenciált képviselhet a jelenlegi standard stroke-kezelések kiegészítésére.

8. References

1. Campbell BCV, De Silva DA, Macleod MR, Coutts SB, Schwamm LH, Davis SM, Donnan GA. Ischaemic stroke. Nat Rev Dis Primers. 2019;5(1):70.
2. Perez-Mato M, Lopez-Arias E, Bugallo-Casal A, Correa-Paz C, Arias S, Rodriguez-Yanez M, et al. New Perspectives in Neuroprotection for Ischemic Stroke. Neuroscience. 2024;550:30-42.
3. Goenka L, Uppugunduri Satyanarayana CR, S SK, George M. Neuroprotective agents in Acute Ischemic Stroke-A Reality Check. Biomed Pharmacother. 2019;109:2539-47.
4. Jayaraj RL, Azimullah S, Beiram R, Jalal FY, Rosenberg GA. Neuroinflammation: friend and foe for ischemic stroke. J Neuroinflammation. 2019;16(1):142.
5. Taylor RA, Sansing LH. Microglial responses after ischemic stroke and intracerebral hemorrhage. Clin Dev Immunol. 2013;2013:746068.
6. Kettenmann H, Hanisch UK, Noda M, Verkhratsky A. Physiology of microglia. Physiol Rev. 2011;91(2):461-553.
7. Shan Y, Tan S, Lin Y, Liao S, Zhang B, Chen X, et al. The glucagon-like peptide-1 receptor agonist reduces inflammation and blood-brain barrier breakdown in an astrocyte-dependent manner in experimental stroke. J Neuroinflammation. 2019;16(1):242.
8. Schoknecht K, Prager O, Vazana U, Kamintsky L, Harhausen D, Zille M, et al. Monitoring stroke progression: in vivo imaging of cortical perfusion, blood-brain barrier permeability and cellular damage in the rat photothrombosis model. J Cereb Blood Flow Metab. 2014;34(11):1791-801.
9. Tomkins O, Shelef I, Kaizerman I, Eliushin A, Afawi Z, Misk A, et al. Blood-brain barrier disruption in post-traumatic epilepsy. J Neurol Neurosurg Psychiatry. 2008;79(7):774-7.
10. Xue S, Zhou X, Yang ZH, Si XK, Sun X. Stroke-induced damage on the blood-brain barrier. Front Neurol. 2023;14:1248970.
11. Abbott NJ, Ronnback L, Hansson E. Astrocyte-endothelial interactions at the blood-brain barrier. Nat Rev Neurosci. 2006;7(1):41-53.

12. Mathiisen TM, Lehre KP, Danbolt NC, Ottersen OP. The perivascular astroglial sheath provides a complete covering of the brain microvessels: an electron microscopic 3D reconstruction. Glia. 2010;58(9):1094-103.
13. Ballabh P, Braun A, Nedergaard M. The blood-brain barrier: an overview: structure, regulation, and clinical implications. Neurobiol Dis. 2004;16(1):1-13.
14. Kimelberg HK. Astrocytic swelling in cerebral ischemia as a possible cause of injury and target for therapy. Glia. 2005;50(4):389-97.
15. Zador Z, Stiver S, Wang V, Manley GT. Role of aquaporin-4 in cerebral edema and stroke. Handb Exp Pharmacol. 2009(190):159-70.
16. Hirt L, Fukuda AM, Ambadipudi K, Rashid F, Binder D, Verkman A, et al. Improved long-term outcome after transient cerebral ischemia in aquaporin-4 knockout mice. J Cereb Blood Flow Metab. 2017;37(1):277-90.
17. Stokum JA, Kurland DB, Gerzanich V, Simard JM. Mechanisms of astrocyte-mediated cerebral edema. Neurochem Res. 2015;40(2):317-28.
18. Manley GT, Fujimura M, Ma T, Noshita N, Filiz F, Bollen AW, et al. Aquaporin-4 deletion in mice reduces brain edema after acute water intoxication and ischemic stroke. Nat Med. 2000;6(2):159-63.
19. Yao X, Derugin N, Manley GT, Verkman AS. Reduced brain edema and infarct volume in aquaporin-4 deficient mice after transient focal cerebral ischemia. Neurosci Lett. 2015;584:368-72.
20. Thrane AS, Rappold PM, Fujita T, Torres A, Bekar LK, Takano T, et al. Critical role of aquaporin-4 (AQP4) in astrocytic Ca2+ signaling events elicited by cerebral edema. Proc Natl Acad Sci U S A. 2011;108(2):846-51.
21. Mi-Hwa KS-H, O.; Young-Do, K.; Min-Jung, B.; You-Kyung, K.; Hyun, SK.; Won-Chan, K.; Ok, JK. . Clinical Usefulness of Serum Glial Fibrillary Acidic Protein in Patients with Acute Ischemic Stroke. J Neurocrit Care. 2009;2(2):50-5.
22. Wunderlich MT, Wallesch CW, Goertler M. Release of glial fibrillary acidic protein is related to the neurovascular status in acute ischemic stroke. Eur J Neurol. 2006;13(10):1118-23.
23. Amalia L. Glial Fibrillary Acidic Protein (GFAP): Neuroinflammation Biomarker in Acute Ischemic Stroke. J Inflamm Res. 2021;14:7501-6.

24. Liu G, Geng J. Glial fibrillary acidic protein as a prognostic marker of acute ischemic stroke. Hum Exp Toxicol. 2018;37(10):1048-53.

25. Foerch C, Curdt I, Yan B, Dvorak F, Hermans M, Berkefeld J, et al. Serum glial fibrillary acidic protein as a biomarker for intracerebral haemorrhage in patients with acute stroke. J Neurol Neurosurg Psychiatry. 2006;77(2):181-4.

26. Luger S, Witsch J, Dietz A, Hamann GF, Minnerup J, Schneider H, et al. Glial Fibrillary Acidic Protein Serum Levels Distinguish between Intracerebral Hemorrhage and Cerebral Ischemia in the Early Phase of Stroke. Clin Chem. 2017;63(1):377-85.

27. Rozanski M, Waldschmidt C, Kunz A, Grittner U, Ebinger M, Wendt M, et al. Glial Fibrillary Acidic Protein for Prehospital Diagnosis of Intracerebral Hemorrhage. Cerebrovasc Dis. 2017;43(1-2):76-81.

28. Persidsky Y, Ramirez SH, Haorah J, Kanmogne GD. Blood-brain barrier: structural components and function under physiologic and pathologic conditions. J Neuroimmune Pharmacol. 2006;1(3):223-36.

29. Peppiatt CM, Howarth C, Mobbs P, Attwell D. Bidirectional control of CNS capillary diameter by pericytes. Nature. 2006;443(7112):700-4.

30. Armulik A, Mae M, Betsholtz C. Pericytes and the blood-brain barrier: recent advances and implications for the delivery of CNS therapy. Ther Deliv. 2011;2(4):419-22.

31. Fernandez-Klett F, Priller J. Diverse functions of pericytes in cerebral blood flow regulation and ischemia. J Cereb Blood Flow Metab. 2015;35(6):883-7.

32. Kamouchi M, Ago T, Kuroda J, Kitazono T. The possible roles of brain pericytes in brain ischemia and stroke. Cell Mol Neurobiol. 2012;32(2):159-65.

33. Liu S, Agalliu D, Yu C, Fisher M. The role of pericytes in blood-brain barrier function and stroke. Curr Pharm Des. 2012;18(25):3653-62.

34. Abbott NJ, Patabendige AA, Dolman DE, Yusof SR, Begley DJ. Structure and function of the blood-brain barrier. Neurobiol Dis. 2010;37(1):13-25.

35. Doolittle ND, Abrey LE, Bleyer WA, Brem S, Davis TP, Dore-Duffy P, et al. New frontiers in translational research in neuro-oncology and the blood-brain barrier: report of the tenth annual Blood-Brain Barrier Disruption Consortium Meeting. Clin Cancer Res. 2005;11(2 Pt 1):421-8.

36. Shi Y, Zhang L, Pu H, Mao L, Hu X, Jiang X, et al. Rapid endothelial cytoskeletal reorganization enables early blood-brain barrier disruption and long-term ischaemic reperfusion brain injury. Nat Commun. 2016;7:10523.

37. Vanlandewijck M, He L, Mae MA, Andrae J, Ando K, Del Gaudio F, et al. A molecular atlas of cell types and zonation in the brain vasculature. Nature. 2018;554(7693):475-80.

38. Koto T, Takubo K, Ishida S, Shinoda H, Inoue M, Tsubota K, et al. Hypoxia disrupts the barrier function of neural blood vessels through changes in the expression of claudin-5 in endothelial cells. Am J Pathol. 2007;170(4):1389-97.

39. Knowland D, Arac A, Sekiguchi KJ, Hsu M, Lutz SE, Perrino J, et al. Stepwise recruitment of transcellular and paracellular pathways underlies blood-brain barrier breakdown in stroke. Neuron. 2014;82(3):603-17.

40. Haley MJ, Lawrence CB. The blood-brain barrier after stroke: Structural studies and the role of transcytotic vesicles. J Cereb Blood Flow Metab. 2017;37(2):456-70.

41. Liu J, Jin X, Liu KJ, Liu W. Matrix metalloproteinase-2-mediated occludin degradation and caveolin-1-mediated claudin-5 redistribution contribute to blood-brain barrier damage in early ischemic stroke stage. J Neurosci. 2012;32(9):3044-57.

42. Vazquez-Liebanas E, Mocci G, Li W, Lavina B, Reddy A, O'Connor C, et al. Mosaic deletion of claudin-5 reveals rapid non-cell-autonomous consequences of blood-brain barrier leakage. Cell Rep. 2024;43(3):113911.

43. Kazmierski R, Michalak S, Wencel-Warot A, Nowinski WL. Serum tight-junction proteins predict hemorrhagic transformation in ischemic stroke patients. Neurology. 2012;79(16):1677-85.

44. Li Y, Zhu ZY, Huang TT, Zhou YX, Wang X, Yang LQ, et al. The peripheral immune response after stroke-A double edge sword for blood-brain barrier integrity. CNS Neurosci Ther. 2018;24(12):1115-28.

45. Lindsberg PJ, Carpén O, Paetau A, Karjalainen-Lindsberg ML, Kaste M. Endothelial ICAM-1 expression associated with inflammatory cell response in human ischemic stroke. Circulation. 1996;94(5):939-45.

46. Gronberg NV, Johansen FF, Kristiansen U, Hasseldam H. Leukocyte infiltration in experimental stroke. J Neuroinflammation. 2013;10:115.
47. Jickling GC, Liu D, Ander BP, Stamova B, Zhan X, Sharp FR. Targeting neutrophils in ischemic stroke: translational insights from experimental studies. J Cereb Blood Flow Metab. 2015;35(6):888-901.
48. Ceulemans AG, Zgavc T, Kooijman R, Hachimi-Idrissi S, Sarre S, Michotte Y. The dual role of the neuroinflammatory response after ischemic stroke: modulatory effects of hypothermia. J Neuroinflammation. 2010;7:74.
49. Nilupul Perera M, Ma HK, Arakawa S, Howells DW, Markus R, Rowe CC, Donnan GA. Inflammation following stroke. J Clin Neurosci. 2006;13(1):1-8.
50. Perez-de-Puig I, Miro-Mur F, Ferrer-Ferrer M, Gelpi E, Pedragosa J, Justicia C, et al. Neutrophil recruitment to the brain in mouse and human ischemic stroke. Acta Neuropathol. 2015;129(2):239-57.
51. Schilling M, Strecker JK, Schabitz WR, Ringelstein EB, Kiefer R. Effects of monocyte chemoattractant protein 1 on blood-borne cell recruitment after transient focal cerebral ischemia in mice. Neuroscience. 2009;161(3):806-12.
52. ElAli A, Jean LeBlanc N. The Role of Monocytes in Ischemic Stroke Pathobiology: New Avenues to Explore. Front Aging Neurosci. 2016;8:29.
53. Han D, Liu H, Gao Y. The role of peripheral monocytes and macrophages in ischemic stroke. Neurol Sci. 2020;41(12):3589-607.
54. Yilmaz G, Arumugam TV, Stokes KY, Granger DN. Role of T lymphocytes and interferon-gamma in ischemic stroke. Circulation. 2006;113(17):2105-12.
55. Hurn PD, Subramanian S, Parker SM, Afentoulis ME, Kaler LJ, Vandenbark AA, Offner H. T- and B-cell-deficient mice with experimental stroke have reduced lesion size and inflammation. J Cereb Blood Flow Metab. 2007;27(11):1798-805.
56. El Amki M, Glück C, Binder N, Middleham W, Wyss MT, Weiss T, et al. Neutrophils Obstructing Brain Capillaries Are a Major Cause of No-Reflow in Ischemic Stroke. Cell Reports. 2020;33(2):108260.
57. Kim JY, Park J, Chang JY, Kim SH, Lee JE. Inflammation after Ischemic Stroke: The Role of Leukocytes and Glial Cells. Exp Neurobiol. 2016;25(5):241-51.

58. Turner RJ, Sharp FR. Implications of MMP9 for Blood Brain Barrier Disruption and Hemorrhagic Transformation Following Ischemic Stroke. Front Cell Neurosci. 2016;10:56.

59. Sorokin L. The impact of the extracellular matrix on inflammation. Nat Rev Immunol. 2010;10(10):712-23.

60. Baeten KM, Akassoglou K. Extracellular matrix and matrix receptors in blood-brain barrier formation and stroke. Dev Neurobiol. 2011;71(11):1018-39.

61. Rosenberg GA, Estrada EY, Dencoff JE. Matrix metalloproteinases and TIMPs are associated with blood-brain barrier opening after reperfusion in rat brain. Stroke. 1998;29(10):2189-95.

62. del Zoppo GJ. The neurovascular unit in the setting of stroke. J Intern Med. 2010;267(2):156-71.

63. Montaner J, Rovira A, Molina CA, Arenillas JF, Ribo M, Chacon P, et al. Plasmatic level of neuroinflammatory markers predict the extent of diffusion-weighted image lesions in hyperacute stroke. J Cereb Blood Flow Metab. 2003;23(12):1403-7.

64. Rosell A, Alvarez-Sabin J, Arenillas JF, Rovira A, Delgado P, Fernandez-Cadenas I, et al. A matrix metalloproteinase protein array reveals a strong relation between MMP-9 and MMP-13 with diffusion-weighted image lesion increase in human stroke. Stroke. 2005;36(7):1415-20.

65. Montaner J, Alvarez-Sabin J, Molina CA, Angles A, Abilleira S, Arenillas J, Monasterio J. Matrix metalloproteinase expression is related to hemorrhagic transformation after cardioembolic stroke. Stroke. 2001;32(12):2762-7.

66. Morancho A, Rosell A, Garcia-Bonilla L, Montaner J. Metalloproteinase and stroke infarct size: role for anti-inflammatory treatment? Ann N Y Acad Sci. 2010;1207:123-33.

67. Zhong C, Yang J, Xu T, Xu T, Peng Y, Wang A, et al. Serum matrix metalloproteinase-9 levels and prognosis of acute ischemic stroke. Neurology. 2017;89(8):805-12.

68. Gori AM, Giusti B, Piccardi B, Nencini P, Palumbo V, Nesi M, et al. Inflammatory and metalloproteinases profiles predict three-month poor outcomes

in ischemic stroke treated with thrombolysis. J Cereb Blood Flow Metab. 2017;37(9):3253-61.

69. Kaindl AM, Degos V, Peineau S, Gouadon E, Chhor V, Loron G, et al. Activation of microglial N-methyl-D-aspartate receptors triggers inflammation and neuronal cell death in the developing and mature brain. Ann Neurol. 2012;72(4):536-49.

70. Hanisch U-K, Kettenmann H. Microglia: active sensor and versatile effector cells in the normal and pathologic brain. Nature Neuroscience. 2007;10(11):1387-94.

71. Jolivel V, Bicker F, Binamé F, Ploen R, Keller S, Gollan R, et al. Perivascular microglia promote blood vessel disintegration in the ischemic penumbra. Acta Neuropathologica. 2015;129(2):279-95.

72. Iadecola C, Anrather J. The immunology of stroke: from mechanisms to translation. Nat Med. 2011;17(7):796-808.

73. Lambertsen KL, Biber K, Finsen B. Inflammatory Cytokines in Experimental and Human Stroke. Journal of Cerebral Blood Flow & Metabolism. 2012;32(9):1677-98.

74. Brown GC, Neher JJ. Eaten alive! Cell death by primary phagocytosis: 'phagoptosis'. Trends Biochem Sci. 2012;37(8):325-32.

75. Alawieh A, Langley EF, Tomlinson S. Targeted complement inhibition salvages stressed neurons and inhibits neuroinflammation after stroke in mice. Sci Transl Med. 2018;10(441).

76. Denes A, Vidyasagar R, Feng J, Narvainen J, McColl BW, Kauppinen RA, Allan SM. Proliferating resident microglia after focal cerebral ischaemia in mice. J Cereb Blood Flow Metab. 2007;27(12):1941-53.

77. Greenhalgh AD, Zarruk JG, Healy LM, Baskar Jesudasan SJ, Jhelum P, Salmon CK, et al. Peripherally derived macrophages modulate microglial function to reduce inflammation after CNS injury. PLOS Biology. 2018;16(10):e2005264.

78. Ju H, Park KW, Kim I-d, Cave JW, Cho S. Phagocytosis converts infiltrated monocytes to microglia-like phenotype in experimental brain ischemia. Journal of Neuroinflammation. 2022;19(1):190.

79. Sun M, Deng B, Zhao X, Gao C, Yang L, Zhao H, et al. Isoflurane preconditioning provides neuroprotection against stroke by regulating the expression of the TLR4 signalling pathway to alleviate microglial activation. Sci Rep. 2015;5:11445.
80. Marino Lee S, Hudobenko J, McCullough LD, Chauhan A. Microglia depletion increase brain injury after acute ischemic stroke in aged mice. Experimental Neurology. 2021;336:113530.
81. Otxoa-de-Amezaga A, Miró-Mur F, Pedragosa J, Gallizioli M, Justicia C, Gaja-Capdevila N, et al. Microglial cell loss after ischemic stroke favors brain neutrophil accumulation. Acta Neuropathologica. 2019;137(2):321-41.
82. Jin WN, Shi SX, Li Z, Li M, Wood K, Gonzales RJ, Liu Q. Depletion of microglia exacerbates postischemic inflammation and brain injury. J Cereb Blood Flow Metab. 2017;37(6):2224-36.
83. Gliem M, Mausberg AK, Lee JI, Simiantonakis I, van Rooijen N, Hartung HP, Jander S. Macrophages prevent hemorrhagic infarct transformation in murine stroke models. Ann Neurol. 2012;71(6):743-52.
84. Wattananit S, Tornero D, Graubardt N, Memanishvili T, Monni E, Tatarishvili J, et al. Monocyte-Derived Macrophages Contribute to Spontaneous Long-Term Functional Recovery after Stroke in Mice. J Neurosci. 2016;36(15):4182-95.
85. Nimmerjahn A, Kirchhoff F, Helmchen F. Resting microglial cells are highly dynamic surveillants of brain parenchyma in vivo. Science. 2005;308(5726):1314-8.
86. Vinet J, Weering HR, Heinrich A, Kälin RE, Wegner A, Brouwer N, et al. Neuroprotective function for ramified microglia in hippocampal excitotoxicity. J Neuroinflammation. 2012;9:27.
87. Boche D, Perry VH, Nicoll JA. Review: activation patterns of microglia and their identification in the human brain. Neuropathol Appl Neurobiol. 2013;39(1):3-18.
88. Davalos D, Grutzendler J, Yang G, Kim JV, Zuo Y, Jung S, et al. ATP mediates rapid microglial response to local brain injury in vivo. Nat Neurosci. 2005;8(6):752-8.

89. Parakalan R, Jiang B, Nimmi B, Janani M, Jayapal M, Lu J, et al. Transcriptome analysis of amoeboid and ramified microglia isolated from the corpus callosum of rat brain. BMC Neurosci. 2012;13:64.

90. Bower NI, Hogan BM. Brain drains: new insights into brain clearance pathways from lymphatic biology. J Mol Med (Berl). 2018;96(5):383-90.

91. Iadecola C, Buckwalter MS, Anrather J. Immune responses to stroke: mechanisms, modulation, and therapeutic potential. J Clin Invest. 2020;130(6):2777-88.

92. Esposito E, Ahn BJ, Shi J, Nakamura Y, Park JH, Mandeville ET, et al. Brain-to-cervical lymph node signaling after stroke. Nat Commun. 2019;10(1):5306.

93. Abbas AL, AH.; Pillai, S. Cellular and Molecular Immunology. 7th ed. ed. Philadelphia, Pennsylvania, USA: Elsevier; 2012.

94. Chapman KZ, Dale VQ, Denes A, Bennett G, Rothwell NJ, Allan SM, McColl BW. A rapid and transient peripheral inflammatory response precedes brain inflammation after experimental stroke. J Cereb Blood Flow Metab. 2009;29(11):1764-8.

95. Offner H, Subramanian S, Parker SM, Afentoulis ME, Vandenbark AA, Hurn PD. Experimental stroke induces massive, rapid activation of the peripheral immune system. J Cereb Blood Flow Metab. 2006;26(5):654-65.

96. Denes A, Wilkinson F, Bigger B, Chu M, Rothwell NJ, Allan SM. Central and haematopoietic interleukin-1 both contribute to ischaemic brain injury in mice. Dis Model Mech. 2013;6(4):1043-8.

97. Furlan JV, M.; Silver, F. . White blood cell count as a marker of stroke severity and clinical outcomes after acute ischemic stroke. Neurology. 2012;78(1 Supplement):P03.011–P03. .

98. Barow E, Quandt F, Cheng B, Gelderblom M, Jensen M, Konigsberg A, et al. Association of White Blood Cell Count With Clinical Outcome Independent of Treatment With Alteplase in Acute Ischemic Stroke. Front Neurol. 2022;13:877367.

99. Huang YW, Yin XS, Li ZP. Association of the systemic immune-inflammation index (SII) and clinical outcomes in patients with stroke: A systematic review and meta-analysis. Front Immunol. 2022;13:1090305.
100. Lee ML, EJ.; Kim, RO.; Pyun, JM.; Joo, BE.; Kwon, KY.; Roh, H.; Ahn, MY.; Lee, K. Systemic immune-inflammation index as a predictor of early stroke progression/recurrence in acute atherosclerotic ischemic stroke. . Clin Neurol Neurosurg. 2024;238:108182.
101. Vila N, Castillo J, Davalos A, Chamorro A. Proinflammatory cytokines and early neurological worsening in ischemic stroke. Stroke. 2000;31(10):2325-9.
102. Smith CJ, Emsley HC, Gavin CM, Georgiou RF, Vail A, Barberan EM, et al. Peak plasma interleukin-6 and other peripheral markers of inflammation in the first week of ischaemic stroke correlate with brain infarct volume, stroke severity and long-term outcome. BMC Neurol. 2004;4:2.
103. Piepke M, Clausen BH, Ludewig P, Vienhues JH, Bedke T, Javidi E, et al. Interleukin-10 improves stroke outcome by controlling the detrimental Interleukin-17A response. J Neuroinflammation. 2021;18(1):265.
104. Spera PA, Ellison JA, Feuerstein GZ, Barone FC. IL-10 reduces rat brain injury following focal stroke. Neurosci Lett. 1998;251(3):189-92.
105. Bodhankar S, Chen Y, Vandenbark AA, Murphy SJ, Offner H. IL-10-producing B-cells limit CNS inflammation and infarct volume in experimental stroke. Metab Brain Dis. 2013;28(3):375-86.
106. He ML, Lv ZY, Shi X, Yang T, Zhang Y, Li TY, Chen J. Interleukin-10 release from astrocytes suppresses neuronal apoptosis via the TLR2/NFkappaB pathway in a neonatal rat model of hypoxic-ischemic brain damage. J Neurochem. 2017;142(6):920-33.
107. Vila N, Castillo J, Davalos A, Esteve A, Planas AM, Chamorro A. Levels of anti-inflammatory cytokines and neurological worsening in acute ischemic stroke. Stroke. 2003;34(3):671-5.
108. Sun W, Wang S, Nan S. The Prognostic Determinant of Interleukin-10 in Patients with Acute Ischemic Stroke: An Analysis from the Perspective of Disease Management. Dis Markers. 2021;2021:6423244.

109. Tang Y, Xu H, Du X, Lit L, Walker W, Lu A, et al. Gene expression in blood changes rapidly in neutrophils and monocytes after ischemic stroke in humans: a microarray study. J Cereb Blood Flow Metab. 2006;26(8):1089-102.
110. Moore DF, Li H, Jeffries N, Wright V, Cooper RA, Jr., Elkahloun A, et al. Using peripheral blood mononuclear cells to determine a gene expression profile of acute ischemic stroke: a pilot investigation. Circulation. 2005;111(2):212-21.
111. Yan J LJ, Greer JM, McCombe PA. Increased expression of the hypoxia-related genes in peripheral blood leukocytes of human subjects with acute ischemic stroke. Clin Exp Neuroimmunology. 2014;5(2):216–26. .
112. Liang D, Bhatta S, Gerzanich V, Simard JM. Cytotoxic edema: mechanisms of pathological cell swelling. Neurosurg Focus. 2007;22(5):E2.
113. Moritani T, Smoker WR, Sato Y, Numaguchi Y, Westesson PL. Diffusion-weighted imaging of acute excitotoxic brain injury. AJNR Am J Neuroradiol. 2005;26(2):216-28.
114. Simard JM, Kent TA, Chen M, Tarasov KV, Gerzanich V. Brain oedema in focal ischaemia: molecular pathophysiology and theoretical implications. Lancet Neurol. 2007;6(3):258-68.
115. Michinaga S, Koyama Y. Pathogenesis of brain edema and investigation into anti-edema drugs. Int J Mol Sci. 2015;16(5):9949-75.
116. Ho ML, Rojas R, Eisenberg RL. Cerebral edema. AJR Am J Roentgenol. 2012;199(3):W258-73.
117. Obenaus A, Badaut J. Role of the non-invasive imaging techniques in monitoring and understanding the evolution of brain edema. J Neurosci Res. 2022;100(5):1191-200.
118. Kleindienst A, Dunbar JG, Glisson R, Marmarou A. The role of vasopressin V1A receptors in cytotoxic brain edema formation following brain injury. Acta Neurochir (Wien). 2013;155(1):151-64.
119. McKenna DJ TG, Abbott F. . Monoamine oxidase inhibitors in South American hallucinogenic plants: tryptamine and beta-carboline constituents of ayahuasca. . J Ethnopharmacol. 1984;1984 Apr;10(2):195-223.

120. Dean JG, Liu T, Huff S, Sheler B, Barker SA, Strassman RJ, et al. Biosynthesis and Extracellular Concentrations of N,N-dimethyltryptamine (DMT) in Mammalian Brain. Sci Rep. 2019;9(1):9333.

121. Barker SA. N, N-dimethyltryptamine (DMT) in rodent brain: Concentrations, distribution, and recent pharmacological data. Prog Neuropsychopharmacol Biol Psychiatry. 2025;137:111259.

122. Vitale AA, Pomilio AB, Canellas CO, Vitale MG, Putz EM, Ciprian-Ollivier J. In vivo long-term kinetics of radiolabeled n,n-dimethyltryptamine and tryptamine. J Nucl Med. 2011;52(6):970-7.

123. Good M, Joel Z, Benway T, Routledge C, Timmermann C, Erritzoe D, et al. Pharmacokinetics of N,N-dimethyltryptamine in Humans. Eur J Drug Metab Pharmacokinet. 2023;48(3):311-27.

124. Vogt SB, Ley L, Erne L, Straumann I, Becker AM, Klaiber A, et al. Acute effects of intravenous DMT in a randomized placebo-controlled study in healthy participants. Transl Psychiatry. 2023;13(1):172.

125. D'Souza DC, Syed SA, Flynn LT, Safi-Aghdam H, Cozzi NV, Ranganathan M. Exploratory study of the dose-related safety, tolerability, and efficacy of dimethyltryptamine (DMT) in healthy volunteers and major depressive disorder. Neuropsychopharmacology. 2022;47(10):1854-62.

126. Carbonaro TM, Gatch MB. Neuropharmacology of N,N-dimethyltryptamine. Brain Res Bull. 2016;126(Pt 1):74-88.

127. Fontanilla D, Johannessen M, Hajipour AR, Cozzi NV, Jackson MB, Ruoho AE. The hallucinogen N,N-dimethyltryptamine (DMT) is an endogenous sigma-1 receptor regulator. Science. 2009;323(5916):934-7.

128. Hayashi T, Su TP. Sigma-1 receptor chaperones at the ER-mitochondrion interface regulate Ca(2+) signaling and cell survival. Cell. 2007;131(3):596-610.

129. Cozzi NV, Gopalakrishnan A, Anderson LL, Feih JT, Shulgin AT, Daley PF, Ruoho AE. Dimethyltryptamine and other hallucinogenic tryptamines exhibit substrate behavior at the serotonin uptake transporter and the vesicle monoamine transporter. J Neural Transm (Vienna). 2009;116(12):1591-9.

130. Ruscher K, Wieloch T. The involvement of the sigma-1 receptor in neurodegeneration and neurorestoration. J Pharmacol Sci. 2015;127(1):30-5.

131. Urfer R, Moebius HJ, Skoloudik D, Santamarina E, Sato W, Mita S, et al. Phase II trial of the Sigma-1 receptor agonist cutamesine (SA4503) for recovery enhancement after acute ischemic stroke. Stroke. 2014;45(11):3304-10.

132. Szabo A, Kovacs A, Riba J, Djurovic S, Rajnavolgyi E, Frecska E. The Endogenous Hallucinogen and Trace Amine N,N-Dimethyltryptamine (DMT) Displays Potent Protective Effects against Hypoxia via Sigma-1 Receptor Activation in Human Primary iPSC-Derived Cortical Neurons and Microglia-Like Immune Cells. Front Neurosci. 2016;10:423.

133. Morales-Garcia JA, Calleja-Conde J, Lopez-Moreno JA, Alonso-Gil S, Sanz-SanCristobal M, Riba J, Perez-Castillo A. N,N-dimethyltryptamine compound found in the hallucinogenic tea ayahuasca, regulates adult neurogenesis in vitro and in vivo. Transl Psychiatry. 2020;10(1):331.

134. Ly C, Greb AC, Cameron LP, Wong JM, Barragan EV, Wilson PC, et al. Psychedelics Promote Structural and Functional Neural Plasticity. Cell Rep. 2018;23(11):3170-82.

135. Vargas MV, Dunlap LE, Dong C, Carter SJ, Tombari RJ, Jami SA, et al. Psychedelics promote neuroplasticity through the activation of intracellular 5-HT2A receptors. Science. 2023;379(6633):700-6.

136. Dennis M, Mead G, Forbes J, Graham C, Hackett M, Hankey GJ, et al. Effects of fluoxetine on functional outcomes after acute stroke (FOCUS): a pragmatic, double-blind, randomised, controlled trial. The Lancet. 2019;393(10168):265-74.

137. Hankey GJ, Hackett ML, Almeida OP, Flicker L, Mead GE, Dennis MS, et al. Safety and efficacy of fluoxetine on functional outcome after acute stroke (AFFINITY): a randomised, double-blind, placebo-controlled trial. The Lancet Neurology. 2020;19(8):651-60.

138. Lundström E, Isaksson E, Greilert Norin N, Näsman P, Wester P, Mårtensson B, et al. Effects of Fluoxetine on Outcomes at 12 Months After Acute Stroke. Stroke. 2021;52(10):3082-7.

139. Percie du Sert N, Alfieri A, Allan SM, Carswell HV, Deuchar GA, Farr TD, et al. The IMPROVE Guidelines (Ischaemia Models: Procedural Refinements Of in Vivo Experiments). J Cereb Blood Flow Metab. 2017;37(11):3488-517.

140. Nardai S, Dobolyi A, Pal G, Skopal J, Pinter N, Lakatos K, et al. Selegiline promotes NOTCH-JAGGED signaling in astrocytes of the peri-infarct region and improves the functional integrity of the neurovascular unit in a rat model of focal ischemia. Restor Neurol Neurosci. 2015;33(1):1-14.
141. Nardai S, Laszlo M, Szabo A, Alpar A, Hanics J, Zahola P, et al. N,N-dimethyltryptamine reduces infarct size and improves functional recovery following transient focal brain ischemia in rats. Exp Neurol. 2020;327:113245.
142. László MJ, Vigh JP, Kocsis AE, Porkoláb G, Hoyk Z, Polgár T, et al. N,N-dimethyltryptamine mitigates experimental stroke by stabilizing the blood-brain barrier and reducing neuroinflammation. Science Advances. 2025;11(33):eadx5958.
143. Krutsay. M. Nisslfärbung mit Kresylechtviolett [Nissl staining with cresyl violet]. Z Med Labortech. 1970(11):75-6
144. Sommer C. Histology and Infarct Volume Determination in Rodent Models of Stroke. Rodent Models of Stroke. Neuromethods2016. p. 263-77.
145. Swanson RA, Morton MT, Tsao-Wu G, Savalos RA, Davidson C, Sharp FR. A semiautomated method for measuring brain infarct volume. J Cereb Blood Flow Metab. 1990;10(2):290-3.
146. Schwamm LH, Koroshetz WJ, Sorensen AG, Wang B, Copen WA, Budzik R, et al. Time course of lesion development in patients with acute stroke: serial diffusion- and hemodynamic-weighted magnetic resonance imaging. Stroke. 1998;29(11):2268-76.
147. Trueman RC, Diaz C, Farr TD, Harrison DJ, Fuller A, Tokarczuk PF, et al. Systematic and detailed analysis of behavioural tests in the rat middle cerebral artery occlusion model of stroke: Tests for long-term assessment. J Cereb Blood Flow Metab. 2017;37(4):1349-61.
148. Krueger M, Bechmann I, Immig K, Reichenbach A, Härtig W, Michalski D. Blood-brain barrier breakdown involves four distinct stages of vascular damage in various models of experimental focal cerebral ischemia. J Cereb Blood Flow Metab. 2015;35(2):292-303.
149. Lendvai D, Morawski M, Négyessy L, Gáti G, Jäger C, Baksa G, et al. Neurochemical mapping of the human hippocampus reveals perisynaptic matrix

around functional synapses in Alzheimer's disease. Acta Neuropathologica. 2013;125(2):215-29.

150. Fernández-Arjona MDM, Grondona JM, Granados-Durán P, Fernández-Llebrez P, López-Ávalos MD. Microglia Morphological Categorization in a Rat Model of Neuroinflammation by Hierarchical Cluster and Principal Components Analysis. Front Cell Neurosci. 2017;11:235.

151. Karperien A, Ahammer H, Jelinek HF. Quantitating the subtleties of microglial morphology with fractal analysis. Front Cell Neurosci. 2013;7:3.

152. Witten IH, Frank E, Hall MA, Pal CJ. Data Mining, Fourth Edition: Practical Machine Learning Tools and Techniques: Morgan Kaufmann Publishers Inc.; 2016.

153. Dempster AP, Laird NM, Rubin DB. Maximum Likelihood from Incomplete Data Via the EM Algorithm. Journal of the Royal Statistical Society: Series B (Methodological). 2018;39(1):1-22.

154. Winer J, Jung CKS, Shackel I, Williams PM. Development and Validation of Real-Time Quantitative Reverse Transcriptase–Polymerase Chain Reaction for Monitoring Gene Expression in Cardiac Myocytesin Vitro. Analytical Biochemistry. 1999;270(1):41-9.

155. Nakagawa S, Deli MA, Kawaguchi H, Shimizudani T, Shimono T, Kittel A, et al. A new blood-brain barrier model using primary rat brain endothelial cells, pericytes and astrocytes. Neurochem Int. 2009;54(3-4):253-63.

156. Perrière N, Demeuse P, Garcia E, Regina A, Debray M, Andreux JP, et al. Puromycin-based purification of rat brain capillary endothelial cell cultures. Effect on the expression of blood-brain barrier-specific properties. J Neurochem. 2005;93(2):279-89.

157. Dukay B, Walter FR, Vigh JP, Barabási B, Hajdu P, Balassa T, et al. Neuroinflammatory processes are augmented in mice overexpressing human heat-shock protein B1 following ethanol-induced brain injury.

158. Sato K, Nakagawa S, Morofuji Y, Matsunaga Y, Fujimoto T, Watanabe D, et al. Effects of fasudil on blood-brain barrier integrity. Fluids Barriers CNS. 2022;19(1):43.

159. Porkoláb G, Mészáros M, Szecskó A, Vigh JP, Walter FR, Figueiredo R, et al. Synergistic induction of blood–brain barrier properties. Proceedings of the National Academy of Sciences. 2024;121(21):e2316006121.
160. Frecska E, Szabo A, Winkelman MJ, Luna LE, McKenna DJ. A possibly sigma-1 receptor mediated role of dimethyltryptamine in tissue protection, regeneration, and immunity. J Neural Transm (Vienna). 2013;120(9):1295-303.
161. Banks WA, Kovac A, Morofuji Y. Neurovascular unit crosstalk: Pericytes and astrocytes modify cytokine secretion patterns of brain endothelial cells. J Cereb Blood Flow Metab. 2018;38(6):1104-18.
162. Kakkar P, Almusined M, Kakkar T, Munyombwe T, Makawa L, Kain K, et al. Circulating Blood-Brain Barrier Proteins for Differentiating Ischaemic Stroke Patients from Stroke Mimics. Biomolecules. 2024;14(11).
163. Zhang X, Wu F, Jiao Y, Tang T, Yang L, Lu C, et al. An Increase of Sigma-1 Receptor in the Penumbra Neuron after Acute Ischemic Stroke. Journal of Stroke and Cerebrovascular Diseases. 2017;26(9):1981-7.
164. Szabo I, Varga VE, Dvoracsko S, Farkas AE, Kormoczi T, Berkecz R, et al. N,N-Dimethyltryptamine attenuates spreading depolarization and restrains neurodegeneration by sigma-1 receptor activation in the ischemic rat brain. Neuropharmacology. 2021;192:108612.
165. Nemes B, Peto K, Nemeth N, Mester A, Magyar Z, Ghanem S, et al. N,N-dimethyltryptamine Prevents Renal Ischemia-Reperfusion Injury in a Rat Model. Transplant Proc. 2019;51(4):1268-75.
166. Sifat AE, Vaidya B, Abbruscato TJ. Blood-Brain Barrier Protection as a Therapeutic Strategy for Acute Ischemic Stroke. AAPS J. 2017;19(4):957-72.
167. Hall CN, Reynell C, Gesslein B, Hamilton NB, Mishra A, Sutherland BA, et al. Capillary pericytes regulate cerebral blood flow in health and disease. Nature. 2014;508(7494):55-60.
168. Eldahshan W, Fagan SC, Ergul A. Inflammation within the neurovascular unit: Focus on microglia for stroke injury and recovery. Pharmacol Res. 2019;147:104349.
169. Kumar V. Toll-like receptors in the pathogenesis of neuroinflammation. J Neuroimmunol. 2019;332:16-30.

170. Montaner J, Alvarez-Sabin J, Molina C, Angles A, Abilleira S, Arenillas J, et al. Matrix metalloproteinase expression after human cardioembolic stroke: temporal profile and relation to neurological impairment. Stroke. 2001;32(8):1759-66.
171. Riedl SJ, Li W, Chao Y, Schwarzenbacher R, Shi Y. Structure of the apoptotic protease-activating factor 1 bound to ADP. Nature. 2005;434(7035):926-33.
172. Acheson A, Conover JC, Fandl JP, DeChiara TM, Russell M, Thadani A, et al. A BDNF autocrine loop in adult sensory neurons prevents cell death. Nature. 1995;374(6521):450-3.
173. Zhu Y, Sun L, Huang T, Jia Y, Yang P, Zhang Q, et al. High Serum Brain-Derived Neurotrophic Factor Is Associated With Decreased Risks of Poor Prognosis After Ischemic Stroke. Stroke. 2023;54(7):1789-97.
174. Chang X, You J, Yang P, He Y, Liu Y, Shi M, et al. High-Serum Brain-Derived Neurotrophic Factor Levels Are Associated With Decreased Risk of Poststroke Cognitive Impairment. Stroke. 2024;55(3):643-50.
175. Xu Q, Ji XF, Chi TY, Liu P, Jin G, Gu SL, Zou LB. Sigma 1 receptor activation regulates brain-derived neurotrophic factor through NR2A-CaMKIV-TORC1 pathway to rescue the impairment of learning and memory induced by brain ischaemia/reperfusion. Psychopharmacology (Berl). 2015;232(10):1779-91.
176. Liu DY, Chi TY, Ji XF, Liu P, Qi XX, Zhu L, et al. Sigma-1 receptor activation alleviates blood-brain barrier dysfunction in vascular dementia mice. Exp Neurol. 2018;308:90-9.
177. Sánchez-Blázquez P, Pozo-Rodrigálvarez A, Merlos M, Garzón J. The Sigma-1 Receptor Antagonist, S1RA, Reduces Stroke Damage, Ameliorates Post-Stroke Neurological Deficits and Suppresses the Overexpression of MMP-9. Mol Neurobiol. 2018;55(6):4940-51.
178. Ngo A, Fattakhov N, Toborek M. Sigma-1 receptor signaling: A potential therapeutic approach for ischemic stroke. J Cereb Blood Flow Metab. 2024;44(12):1430-40.

179. Candelario-Jalil E, Dijkhuizen RM, Magnus T. Neuroinflammation, Stroke, Blood-Brain Barrier Dysfunction, and Imaging Modalities. Stroke. 2022;53(5):1473-86.

9. Bibliography of the candidate's publications

Thesis-related publications

Nardai S, Laszlo M, Szabo A, Alpar A, Hanics J, Zahola P, et al. N,N-dimethyltryptamine reduces infarct size and improves functional recovery following transient focal brain ischemia in rats. **Exp Neurol.** 2020;327:113245.

László MJ, Vigh JP, Kocsis AE, Porkoláb G, Hoyk Z, Polgár T, et al. N,N-dimethyltryptamine mitigates experimental stroke by stabilizing the blood-brain barrier and reducing neuroinflammation. **Sci Adv.** 2025;11(33):eadx5958.

Other publications

László JM, Hortobágyi T. Hemorrhagic transformation of ischemic stroke. **Vasc Dis Ther.** 2017;2(4):1-25. doi:10.15761/VDT.1000130.

Zamodics M, Babity M, Schay G, Bucsko-Varga A, Kovacs E, Horvath M, et al. Investigation of body composition and cardiac sports adaptation in elite water polo players. **Sports (Basel).** 2025;13(6).

Reichl JJ, Hamid KA, Burkard T, Vischer AS, Guzman C, Dudek D, et al. PPG-based smartphone application vs usual care for atrial fibrillation screening: a European multicenter randomized trial. **Heart Rhythm.** 2025 Dec;22(12):e1155-e1162. doi:10.1016/j.hrthm.2025.07.060. Epub 2025 Sep 16. PMID:40769446.

10. Acknowledgments

I would like to express my deepest gratitude to my supervisors, **Dr. Sándor Nardai** and **Prof. Zoltán Nagy**, for their continuous guidance, encouragement, and invaluable support throughout my research. I am also sincerely thankful to **Prof. Béla Merkely** for his support, and to **Prof. Alán Alpár** for his guidance.

I am grateful to the entire Szeged team, with special thanks to **Prof. Mária Deli** and Dr. **Judit Vígh**, whose expertise and collaboration greatly contributed to the completion of this dissertation.